THE RHEOLOGY, PROPERTIES AND MORPHOLOGY OF THERMOTROPIC LIQUID CRYSTALLINE POLYMERS

This Thesis is submitted in accordance with
the requirements of the University of Liverpool
for the degree of Doctor in Philosophy by
Adrian Philip Pickles.

September 1991

ABSTRACT

The primary objective was to characterise the rheological
properties of a thermotropic liquid crystalline polymer
under conditions relevant to injection moulding.
Secondary objectives were to investigate the mechanical
properties, and to examine the structure and morphology
of injection moulded articles.

The rheological properties were examined using a
laboratory rheometer and an instrumented injection
moulding machine. Both shear and extensional flow was
investigated, for glass filled and unfilled versions of
the polymer. Using an existing rheological model, the
shear and extensional flow was found to be describable by
a power law relationship over the range of shear rates
covered. The viscosities were found to be independent of
temperature, between 330°C and 350°C. At 340°C the shear
flow was similar to that of low viscosity thermoplastics,
while the extensional flow was found to be far more
strain rate sensitive. Results suggested that the polymer
flowed in domains, comprised of a number of aligned
molecules, which become extended in the flow direction at
higher strain rates.

The structure and properties were investigated by the
examination of injection moulded plaques. The mouldings,
which consisted of four distinct morphogical layers, were
found to be highly anisotropic, with superior properties
in the flow direction. These properties were dependent on
section thickness, decreasing with increasing thickness.
The presence of glass fibres also resulted in a reduction
in mechanical properties in the flow direction, due to a
poor fibre matrix bond, and a disruption to the highly
aligned polymer domains. X-ray diffraction experiments
indicated changes in orientation, with highly oriented
skin layers and transverse orientation in the core.

ACKNOWLEDGEMENTS

AUTHOR'S PUBLICATIONS

1. A.P. Pickles, Dr. A.G. Gibson, Paper 19, The Polymer Processing Society, Autumn Meeting, Kerkrade, The Netherlands, October 1989.

2. A.P. Pickles, Dr. A.G. Gibson, Paper 19, The Institute of Metals, Metals and Materials '90, The University of Liverpool, April 1990.

TABLE OF CONTENTS

List of Figures

Symbols and Abbreviations

LCP - Liquid crystalline polymer
SRP - Self reinforcing polymer
PET - Poly(ethylene terephthalate)
POB - Acetoxybenzoic acid
HBA - Hydroxybenzoic acid
PPT - Poly(phenylene-terephthalamide)
IA - Isophthalic acid
HQ - Hydroquinone
HNA - Hydroxynaphthoic acid
PP - Polypropylene

S - Order parameter
n - Director vector
Θ - Angle between molecular axis and director
f_H - Hermans orientation function
N_1 - Primary normal stress difference

η_s - Shear viscosity
η_e - Extensional viscosity
η_0 - Zero rate (Newtonian) viscosity
τ_w - Wall shear stress
σ - Extensional stress
Γ - Shear rate
ϵ - Strain rate
G & m - Shear viscosity power law constants
H & n - Extesional viscosity power law constants
α - Die semi angle
R_1 - Capillary radius
R_0 - Upstream radius
L - Capillary length
Q - Volume flow rate
P - Pressure
P_{cap} - Capillary pressure
P_{ent} - Entry pressure
P_{As} - Shear component of the entry pressure
P_{Ae} & P_{Be} - Extensional components of the entry pressure
V_f - Volume fraction of fibres
V_m - Volume fraction of matrix
r_0 - Radius of flowing unit
r_1 - Radius of fibre
L/D - Aspect ratio of flowing unit
Ω & f - Constants in the Carreau-Ysasuda equation

CHAPTER 1

Introduction

1.1   Objectives

This thesis is based on an investigation of the processing and properties of a thermotropic liquid crystal polymer.

The primary objective was to characterise the rheological properties of the polymer over a range of shear rates. This involved the examination of both the shear and extensional viscosities, under conditions relevant to injection moulding, using a previously derived rheological model. The effect of short glass fibre reinforcement on the viscosity of the polymer was also investigated.

Secondary objectives were to characterise the mechanical properties, and examine the structure and morphology of injection moulded articles produced from the same liquid crystalline polymer. The effect of glass reinforcement was again studied.

1.2   Background

Liquid crystalline behaviour was first described in 1888, during studies of thermotropic cholesteric molecules[1]. The phenomenon of liquid crystallinity was examined on a qualitative level until 1922, when the concept of three distinct mesophases was proposed[1]. These were nematic, cholesteric and smectic, each providing a structural model, on the molecular scale, for the different textures observed.

Polymeric liquid crystallinity was first observed in lyotropic biopolymers, for example, tobacco mosaic virus and collagen, which were extensively studied in the 1940's[2].

Work carried out on lyotropic polymers, in particular the synthetic polypeptides which were investigated by Courtaulds Ltd.[3], led to the first theories pertaining to liquid crystallinity. One of these was Flory's 1956 lattice theory for phase equilibria in solutions of rod-like particles[4]. This theory was validated in 1965 when Kwolek discovered that certain wholly aromatic polyamides gave anisotropic solutions in alkylamide and alkylurea solvents[2,5]. This discovery was one of the most significant milestones in the history of liquid crystalline polymers because it ultimately led to the commercial production of aramid fibres, marketed under

2

the trade name Kevlar[R] by DuPont in 1971[2,6].

Due to the rigid 'rod-like' nature of many liquid crystalline polymers (LCPs), an analogy is often drawn between these rods and fibrous reinforcements, such as glass fibre. For this reason LCPs are sometimes referred to as self reinforcing polymers, or SRPs.

In 1970 a paper by Frank[7] on the strength and stiffness of polymers provided another impetus to the research. The paper discussed the difference found between the experimental and theoretical moduli of polymers. Frank concluded that for polymers to reach their theoretical moduli the polymer chains must be in an extended conformation. A number of ways in which high stiffness and strength values may be obtained were suggested. These included cross-linking, increasing the number of bonding electrons with the use of aromatic rings or double bonds, and process routes such as cold extrusion or drawing, melt extrusion and fibre spinning from either a melt or solution. All of these have subsequently been shown to produce the desired effect of improving the mechanical properties.

Following the commercial production of the lyotropic polymers, activity was directed at the possibility of melt processable (thermotropic) liquid crystal polymers. The first thermotropic polymers were based on all-

aromatic polyesters, reported in patents assigned to ICI in 1965[5]. However, these polymers had such high melting points that they could not be melt spun or moulded, and their liquid crystalline properties were not described specifically in the patents. Other patents were published in 1972, but the first real breakthrough came in 1974 when the conventional melt spinning of a copolyester of 60 mole% p-acetoxybenzoic acid and poly(ethylene terephthalate) (POB/PET 60/40) at 275°C was reported[3]. This was subsequently patented by Eastman Kodak under the name X7G^R[2].

The first published work on the injection moulding of LCPs was seen in 1976, again on compositions of POB/PET[3]. Since this, several companies have developed thermotropic liquid crystalline polymers, including ICI, who manufacture the SRP1 range studied in this project. This has also been closely linked with research activity in many aspects of liquid crystalline behaviour.

One such area has been rheological behaviour. In a review by Wissbrun[8] it was observed that an understanding of the rheological behaviour associated with liquid crystallinity is essential for processing the polymer into the appropriate structure. The flow characteristics of thermotropic polymers are both qualitatively and quantitatively different from conventional isotropic polymer melts[9]. For example, over a certain temperature

4

range they exhibit relatively low melt viscosity combined with long relaxation times[10]. Such phenomena reveal the importance of obtaining a greater understanding of the rheological properties.

Knowledge of the flow properties also becomes important when discussing processing routes, for example injection moulding. The different flow regimes which occur during mould filling, coupled with the heat transfer and molecular relaxation effects produce varying degrees of orientation, even in conventional thermoplastic polymers[11]. In LCPs the complex flow patterns manifest themselves as a layer structure, visible to the naked eye[12,13]. A review by Cogswell[6] looked at the processability of LCPs in relation to their service performance, the results indicating some similarities between them and long fibre reinforced thermoplastics.

Another area of recent interest has been the application of LCPs as an additive to conventional thermoplastic polymers. This was investigated by Isayev and Modic[14], and Nobile et al.[15] using blends of polycarbonate and PET/HBA. It was found that, although there was no solubility between the two phases, the introduction of the liquid crystalline polymer produced a drop in melt viscosity and an enhancement of mechanical properties.

LCPs have also been shown to be suitable candidates for

sandwich injection moulding. In work performed by Baird and Wilkes[16], a low viscosity thermotropic polymer, produced from HBA/PET, was used to form an oriented skin with the core of the moulding being filled with PET. In this way the core of a moulding, which would ordinarily be filled with transversally oriented polymer, is replaced by a cheaper polymer. This results in a more economic use of the LCP, and a potential increase in the mechanical properties, for example, bending modulus.

Current areas of possible use for LCPs include fibre optics, electronics, chemical processing equipment, aerospace and consumer products[17,18]. However, to achieve the full potential of the LCPs, a greater understanding of the flow behaviour, and the resultant moulded structure and morphology is needed.

A summary of the historical developments of liquid crystalline polymers up to the mid 1980s was written by Tai-Shung Chung[19], whilst the more specific areas of structure and properties were reviewed by Wendorff and Zimmermann[20].

CHAPTER 2

Literature Review

2.1   Liquid Crystals

The term liquid crystal signifies a state of aggregation
that is intermediate between the crystalline solid and
the amorphous liquid[21]. Generally, a liquid crystal is
associated with an anisotropic liquid state, in which the
molecules possess a degree of long range order.

2.1.1   Phase Transitions

Liquid crystals are characterised by systematic phase
transitions that occur as the temperature is increased.
Thermotropic polymers go from a solid phase, through the
liquid crystal transitions and then into an isotropic
phase. It should be noted that in polymeric LCPs the
isotropic phase is sometimes not observed due to the
polymer degrading when high temperatures are involved.

Liquid crystal structures are characterised by the degree
of molecular orientation in the three dimensional
structure. These structures are referred to as mesophases
and are subdivided into three categories, nematic,

cholesteric and smectic.

In a nematic mesophase the molecules possess a high degree of long range orientational order, but no long range translational order[21]. This structure is shown schematically in figure 2.1a. The average direction of the molecules is defined by a vector n and the deviation from this direction is given by an order parameter S, defined as $S = \frac{1}{2}(3\cos^2\theta - 1)$, where θ is the angle between the molecular axis and the director n.

The cholesteric structure closely resembles that of the nematic, except that a helical twist is imposed on the layers normal to the director n. This is depicted schematically in figure 2.1b. Only optically active molecules form the cholesteric mesophase, inactive ones or racemic mixtures result in helices with infinite pitch, i.e. true nematic[21].

The smectic mesophase has been subdivided into seven categories, described by Demus and Richter[1]. These are labelled S_A, S_B, S_C, S_D, S_E, S_F, and S_G, the denotation been chosen on the basis of the chronological order in which they were first observed. In general the polymers have a stratified structure with the variations in molecular arrangements within the layers giving rise to the different structures. The structures of smectic A and C are shown in figure 2.1c and d.

8
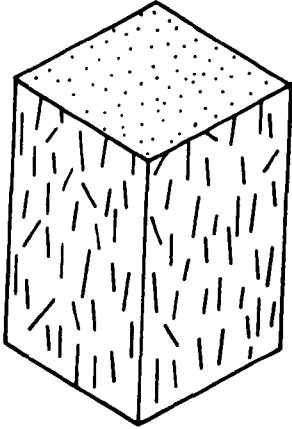
a.   b.
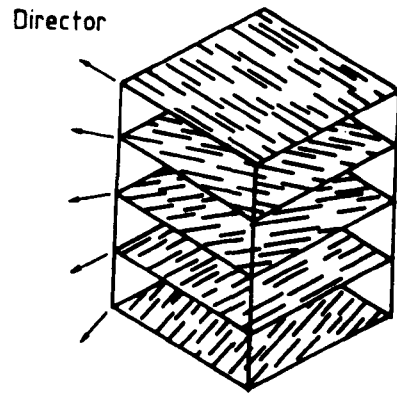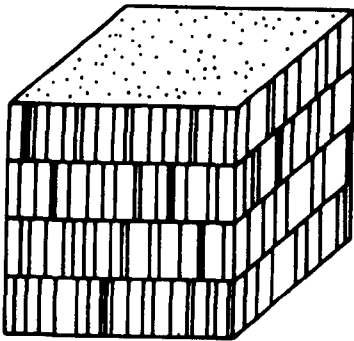
c.   d.
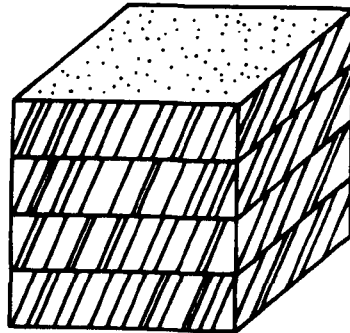
Figure 2.1. Schematic representation of the liquid
crystalline mesophases[1].
a. Nematic structure.
b. Cholesteric structure.
c. Smectic A structure.
d. Smectic C structure.

2.1.2 Texture Observation

The textures of thermotropic liquid crystals have been discussed in detail by Demus and Richter[1]. The structure of the liquid crystal, when viewed in polarized light, is characterised by a defect pattern produced by lattice defects such as points, lines or walls. Line defects, or disclinations, are prevalent in liquid crystals and often determine the features of the texture. The use of a hot stage microscope for the observation of these textures allows the various phase transitions to be identified as the temperature is raised or lowered.

Meurisse and coworkers[22] used a microscopy technique to identify mesophases in several aromatic-aliphatic polyesters. However, it was noted that texture observation was insufficient for the classification of the mesophase. To remedy this, miscibility and X-ray studies were suggested to provide additional information. In a later paper, Lenz[23] discussed the additional techniques of DSC, small angle light scattering, NMR[24,25], melt rheology, electron microscopy and electron diffraction.

2.1.3 Lyotropic Liquid Crystalline Polymers

Lyotropic liquid crystal polymers form an ordered state

when the polymer is dissolved in an appropriate solvent. The formation of the mesophase is restricted to a tight regime which is dependent on both the concentration and temperature of the solution. Flow induced phase transitions have been predicted to occur at a critical extensional velocity gradient, however, direct evidence has been difficult to obtain[26].

2.1.3.1 Formation of the Liquid Crystal

Much of the early work on liquid crystallinity was performed on lyotropic systems, most notably the tobacco mosaic virus and collagen[2]. After the publication of Flory's theory in 1956[4] a large amount of research was directed at its validation. Work on poly(benzyl glutamates) in suitable solvents produced several important findings[27], described below.

A critical polymer volume fraction was found, above which the solution separated into an isotropic and anisotropic phase. This critical volume fraction was found to be temperature dependent, and by carefully controlling the conditions the solution could be kept in the isotropic state. By altering either polymer concentration or temperature, the solution could be forced passed the critical point and the structure of the anisotropic phase examined under the microscope as it developed. A second

critical point was found at higher volume fractions, above which the solution was completely anisotropic.

The majority of synthetic polymers so far shown to form lyotropic systems are the aromatic polyamides[28]. Some of the most common solvents include concentrated sulphuric acid and $CHCl_3$.

2.1.3.2 Practical applications

Recent interest in lyotropic liquid crystals has been stimulated by the possible practical applications. Most important in this has been the drive to produce temperature resistant, ultra-high strength fibres[27]. Predisposition to such properties occurs mostly in aromatic structures such as polyarylamides and polypeptides, the former of which is the basis of Kevlar[R][3].

Most of the research in this area has been done by the investigation of the variables in the dry-jet wet spinning of polymer solutions. This process is shown schematically in figure 2.2. A number of important factors have been deduced. Firstly the solution must stay in the liquid crystalline phase, and so temperature and concentration are vitally important. Secondly, an air gap between the die and the coagulation bath provides for

Polymer Solution

Air
Gap

Elongational
Flow Region

Coagulation
Bath

Take Up
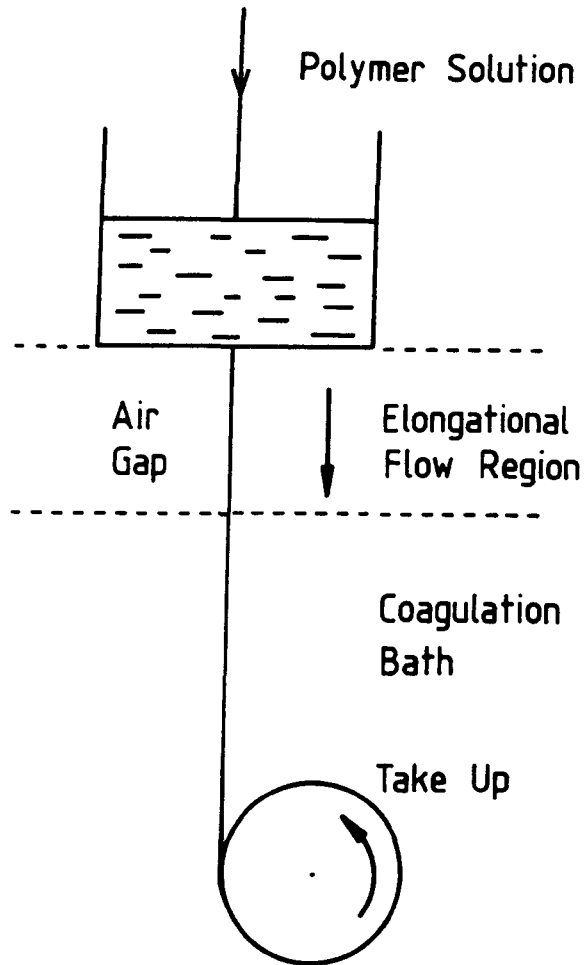
Figure 2.2.   Representation of the dry-jet wet spinning
process for lyotropic solutions[3].

13

elongational flow which increases chain orientation and
hence mechanical properties. The coagulation bath is
needed to remove the solvent, and depending on the
particular solvent used, this may require a number of
steps. Finally heat treatment of the fibre can improve
its mechanical properties by more than a factor of
three[3].

2.1.4   Thermotropic Liquid Crystal Polymers

Thermotropic liquid crystal polymers form an ordered
phase which is dependent on temperature alone. The
mesophase, which persists in the molten state, is
retained as the temperature is lowered, to produce a
solid which possesses a high degree of molecular
orientation.

2.1.4.1   Molecular Structure

Polymeric structures which contain large rigid assemblies
of aromatic rings are found to be intractable and usually
degrade before melting. Hence, in order to lower the
melting point the almost perfect regularity of para
linked aromatic chains must be disrupted. This may be
achieved in two ways[10,29,30]. Firstly, by the addition
of large side groups, the chains can be prevented from

packing close together[31], known as frustrated chain packing. Secondly, the linearity of the chain can be disrupted by the use of aliphatic (flexible), or meta aromatic (rigid) links, thus weakening the overall chain cohesion in the melt. A comprehensive review of the production of thermotropic polyesters was given by Jin et al.[32].

Mesogenic groups possess a large degree of asymmetry, and are a feature common to all liquid crystalline substances[33]. They form comparatively rigid structures, which, in main chain LCPs cause the chain backbone to be highly extended. Due to steric interactions between neighbouring chains in the molten phase, these extended chains from a melt in which the chains become aligned.

Introduction of a mesogenic group into a polymer backbone gives main chain liquid crystalline polymers, while attaching the groups to a polymer backbone leads to side chain liquid crystalline polymers[2,34,35]. A simplified representation of these two structures is shown in figure 2.3. In recent years several variations on these two conformations have been described[36,37], for example, paired mesogens, combined main and side chain systems, laterally fixed mesogens and cross shaped mesogens. By altering the mesogenic units and/or the spacers, the number of possible LCPs becomes very large. Numerous publications[25,36,37,38,39,40,41,42,43] have been

a.

b.
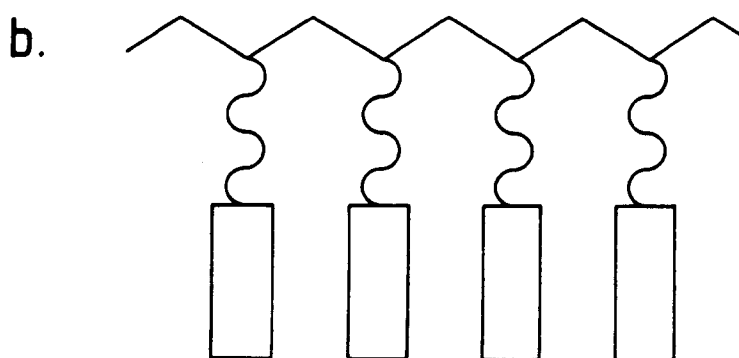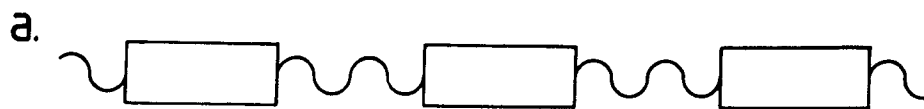
☐ —— Mesogenic Group

∿∿ —— Flexible Spacer

Figure 2.3. Schematic illustration of possible molecular
structures for thermotropic liquid crystalline polymers.
a. Main chain.
b. Side chain.

written concerning the effect of altering these
variables.

2.1.4.2 Synthesis

According to patents published in the U.S., main chain
aromatic liquid crystal polyesters are generally
polymerised through a condensation reaction[19]. To aid
the reaction process the monomers are usually acetylated
and the temperature set around 50°C above the highest
melting point of the monomers. By-products, such as
acetic acid, are removed as the reaction proceeds, with
the final polymerisation steps being carried out under
vacuum[19,44].

Side chain liquid crystalline polymers can in theory be
produced by three methods, addition or condensation
polymerisation and modification of existing linear
polymers. In practice most side chain LCPs are produced
by the addition route. The polymerizable group is usually
a methacrylate or an acrylate, forming a flexible vinyl
backbone. As yet no polymers synthesized by condensation
polymerisation have shown side chain liquid crystalline
character, while the modification method, relying on
reactive groups in the monomers, has been limited to
polysiloxanes[45].

2.1.4.3. Practical application

The early work was stimulated by the production of fibres from lyotropic solutions, and hence the research was directed at melt spinning. Most of the investigations were performed on copolyesters, predominantly a combination of p-acetoxybenzoic acid and poly(ethylene terephthalate). The first reported work came from Kuhfuss and Jackson in 1974, and was followed by many subsequent publications, as stated in the review by Lewis and Fellers[3].

Recent investigations of spinning fibres from a nematic melt[46,47,48] have concentrated on the examination of process variables in an attempt to produce fibres with enhanced properties. However, the values of stiffness and strength obtainable in fibres produced from the melt are considerably less than those of fibres spun from lyotropic solutions.

In 1976 Jackson and Kuhfuss, and also McFarlane described the injection moulding of copolyesters. This was an important step as it opened up whole new areas for the possible use of liquid crystalline polymers.

It has been shown that for thermotropic polymers the processing temperatures and rates play a major role in determining the structure, morphology, and mechanical strength of products[3].

2.2   Rheology

2.2.1   Introduction

It is now widely recognised that the molecules of a
liquid crystalline polymer are oriented by the flow of
the polymer[3,49]. For this reason an understanding of
the rheological properties becomes an important factor.
By gaining more knowledge on the flow process it will be
easier to take full advantage of the unique properties of
the liquid crystalline polymers.

2.2.2   The Three Stage Flow Curve

In 1980 Onogi and Asada introduced the concept of the
three stage flow curve along with proposed structures for
each stage[50]. Subsequent to this a large proportion of
research has looked at the possibility of fitting
experimental data to this flow curve. Figure 2.4 shows a
schematic flow curve along with the proposed structures.
The three regions are as follows:

Stage I is envisaged as a conglomeration of piled
polydomains[50]. In this form the liquid crystal consists
of individual domains within which the molecular
orientation varies. During the shear thinning process the

19
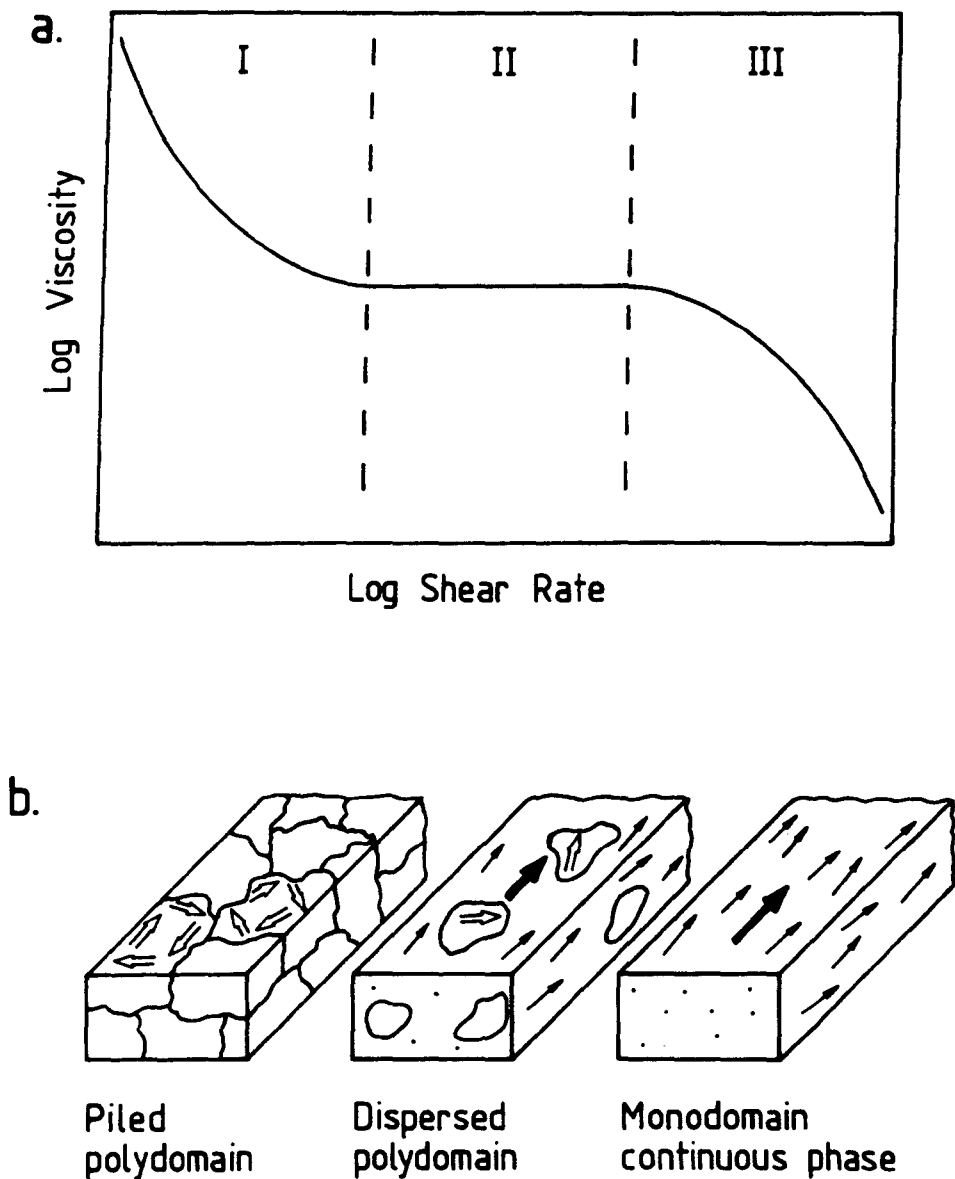
Figure 2.4. Schematic flow curve and molecular
structures, as postulated by Onogi and Asada[50].
a. Three stage flow curve showing a shear thinning
   region, followed by a constant viscosity plateaux and a
   final shear thinning region.
b. The proposed structural changes for each region of the
   flow curve.

orientation within each domain becomes unified, and some domains may coalesce. The shear thinning region is often explained as being associated with a yield stress, which is accounted for by three possible mechanisms[8]. Firstly, a stress is required to deform the director field, secondly, it is caused by the plastic flow of piled domains and thirdly, the yield stress is a result of phase separation of the polymer.

Although these three mechanisms have been looked into, none appears to give a completely satisfactory explanation of the observed effects.

The proposed structure of stage II is one of dispersed polydomains[50], with individual oriented domains in a continuous phase. This region has been extensively studied for lyotropic polymers and a number of relationships have been deduced between viscosity, concentration and molecular weight[8]. Extensive work of this nature has not been produced for thermotropic polymers.

In stage III the polydomain structure is believed to be completely broken down into a continuous monodomain phase[50].

2.2.2.1 Experimental Evidence

In a review by Wissbrun[8] the flow curves of several
polymer systems were plotted and compared with the
predictions of the three stage model. This is reproduced
in figure 2.5, along with some additional data obtained
from subsequent publications.

Of the seven polymers initially described by Wissbrun,
only three of the systems, 1, 3, and 5, showed all three
regions. System 6 does show stage II and III, and may
well have shown stage I if lower shear rates had been
examined. However, the remaining systems, including both
the thermotropic polymers, show only one region of shear
thinning, either stage I or III. Evidence given by
Wissbrun indicates that these are in fact stage I. The
two additional plots are for thermotropic polymers.
System 8[44] shows only shear thinning, stage I, while
system 9[51,52] shows stage I and II.

The important conclusion to be drawn from these plots is
that the observed behaviour of many thermotropic liquid
crystalline polymers does not appear to support the
general concept of a three stage flow curve. The only
piece of evidence is the appearance of stage II at high
shear rates for the HBA/PET system at 275°C. The high
shear rate data was obtained using a capillary rheometer,
which may be subject to a number of sources of errors,

22
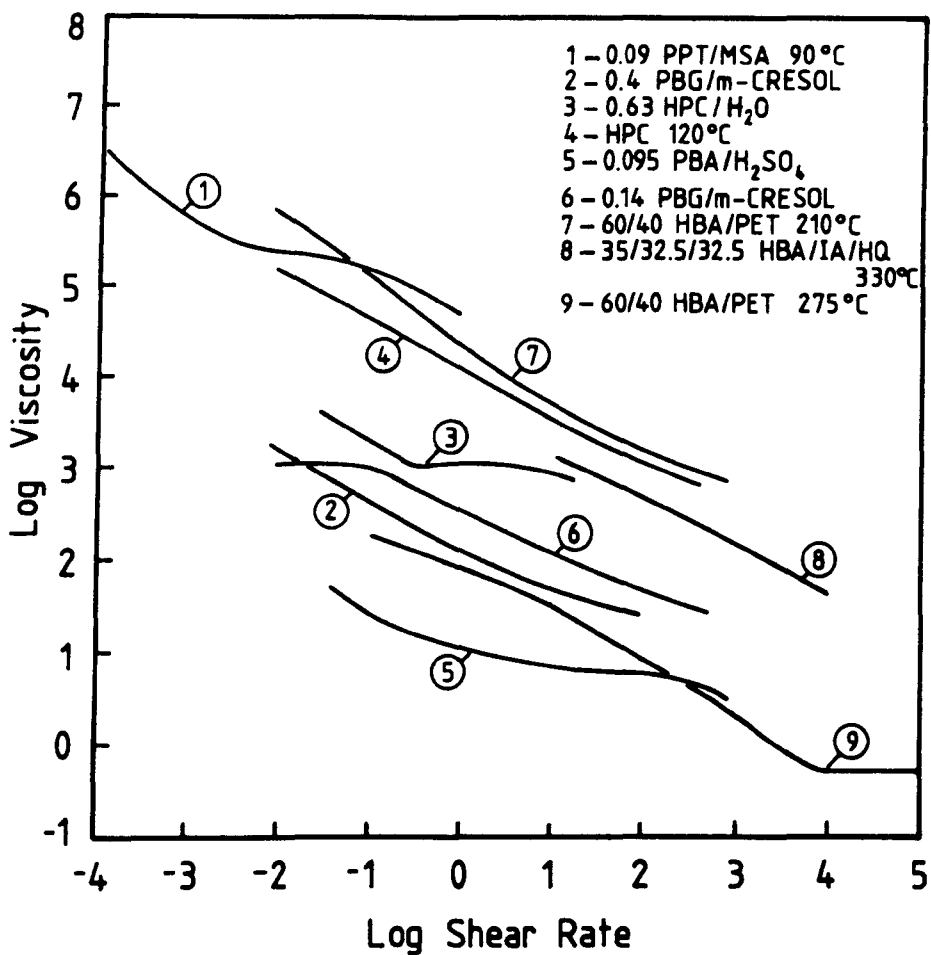
Figure 2.5. Experimentally obtained flow
curves(8,44,51,52), for lyotropic and thermotropic liquid
crystalline polymers.

for example, shear heating, inertia and pressure effects.
Gotsis and Baird investigated these possible errors, but
found them to be fairly small[52]. Hence the high shear
rate plateau was believed to be a real effect.

Commenting on the three stage proposal, Gotsis and Baird
indicate serious reservations. At the lowest shear rates
the viscosity appears to be levelling off, and not
increasing as Onogi and Asada suggest. Also, it was felt
unlikely that the plateau in viscosity would be followed
by another region of shear thinning.

Experiments performed by Yang and Krigbaum[53] on
thermotropic polymers produced from HBA and HNA indicated
a plateau in the viscosity. However, it was believed that
this was not a real effect, and was assumed to be due to
a transition from shear thickening to shear thinning
viscosity. Also, the region no longer appeared when the
temperature was increased sufficiently to avoid
recrystallization.

To summarise, the initial proposals of Onogi and
Asada[50] provide a useful starting point, but many
studies on the rheology of thermotropic liquid
crystalline polymers fail to adequately support their
theory[8,52,53]. The suggested structures are plausible
but do not appear to be associated with any direct change
in the observed viscosity. Much more work is needed in

this area, looking not only at the shear viscosity, over a wide range of shear rates, but also the extensional viscosity.

2.2.3 Transient Shear Flow

The transient shear flow behaviour of thermotropic polymers was investigated by Baird[51]. In later work, carried out in conjunction with Viola[54], both thermotropic and lyotropic polymers were examined. These investigations resulted in a number of important conclusions.

The rheological measurements were performed using a Rheometrics mechanical spectrometer with cone-and-plate and parallel plate geometries. The thermotropic polymer, a 60% HBA/PET copolymer at 275°C, exhibited an instantaneous stress overshoot at shear rates from 5 to 40 sec^{-1}. For the higher shear rates a secondary overshoot also occurred. In an earlier paper Wissbrun[55] had also noted two maxima in the shear stress for the same polymer at 280°C. Investigations of the lyotropic polymer, 12wt% PPT/H_2SO_4 solution at 60°C, revealed only a primary stress overshoot, indicating that the secondary peak seen with the HBA/PET was unlikely to be associated with the liquid crystalline nature of the polymer.

On cessation of the shear, the shear stress rapidly fell to zero, which was interpreted as an indication that the polymer did not exhibit a yield stress. This result is in contrast to the proposal that stage I of the three stage flow curve is associated with a yield stress, as indicated by Wissbrun[8].

The results of interrupted shear tests showed the disappearance of the primary stress overshoot, while the secondary peak remained present. This effect persisted for annealing times of up to three minutes. Similar tests on the lyotropic system indicated a considerably reduced stress overshoot after a relaxation time of three minutes.

It was assumed that the primary peak was a manifestation of orientation of the molecules, and by implication this was not destroyed by annealing at the melt temperature. To investigate this further Viola and Baird used wide angle X-Ray scattering to determine orientation. They found that the samples produced by shearing revealed very little molecular orientation, while ribbons subjected to an elongational strain showed a high degree of orientation in the flow direction. Additionally it was found that molecular orientation was lost by annealing samples for less than a minute at 275°C. Hence, it was concluded that the first stress overshoot was not related to long range molecular orientation.

Viola and Baird concluded that the most probable explanation was the existence of a polydomain structure, as proposed by Onogi and Asada[50]. The initial structure, consisting of large domains, is broken down into smaller domains by the action of shear and is responsible for the stress overshoot. These small domains may then become extended or coalesce to form highly oriented larger domains. However, the relaxation of the stress to zero upon cessation of the shear flow indicates a lack of any long range cohesive structure.

2.2.4 Time Dependence

Using a liquid crystalline polymer, produced from chlorohydroquinone, 4,4-dihydroxydiphenyl, terephthalic acid, and resorcinol, Gochanour and Weinberg investigated the effect of time on its rheological properties[56,57].

The rheological measurements were performed in a forced oscillation mode using a Weissenberg rheogoniometer in parallel plate geometry, providing data on the complex viscosity. It was found that holding the polymer at its melt temperature greatly affected its viscosity. At a frequency of 1 s^{-1}, and a temperature of 325°C, an annealing time of 30 minutes caused a factor of ten increase in the complex viscosity, and a hundred fold increase after 180 minutes.

Gochanour and Weinberg concluded that the change in viscosity was caused by a change in crystallinity. This conclusion was substantiated by DSC traces for samples of the polymer which had been annealed for various times. Samples annealed around the melt temperature were found to exhibit two peaks at the melting transition, one at 310°C, the other at 340°C. The higher temperature peak was believed to be a result of either a different crystal structure, or crystals which were larger or more perfect.

2.2.5 Thermal and Shear History

The effect of the thermal and shear history on the rheological properties of LCPs was noted by Wissbrun[55] and also by Cogswell[58].

In the experiments performed by Wissbrun[55], samples of a 60/40 HBA/PET polymer were loaded into capillary and rotational rheometers at elevated temperatures. After one minute at this temperature the sample was allowed to cool to the test temperature of 210°C. Wissbrun found that heating the polymer prior to the actual test resulted in a lowering of the viscosity. The higher the initial temperature, the lower the final viscosity.

The hypothesis was that this decrease in viscosity was due to the melting of crystallites at high temperature.

To elucidate this, X-ray diffraction studies were
employed to investigate possible changes in sample
crystallinity. Samples extruded at 230°C revealed sharp
X-ray reflections, while those extruded at 280°C showed
no such reflections. The reflections obtained correspond
closely to those seen in pure HBA. Thus it appears that
pre-heating the polymer destroys crystalline regions of
HBA.

In the work of Cogswell[58] the melt flow rate of a
polymer composed of chlorohydroquinone, terephthalic acid
and ethylene-4,4-dioxybenzoic acid, in the ratio
50/25/25, was investigated. At a temperature of 223°C a
melt flow index of 6.4 was observed. This dropped to 0.3
after the melt had been held at 223°C for 18 hours, and
increased to 260 when apparatus was charged at 240°C and
then cooled to 223°C.

In addition to thermal history dependence, Cogswell also
showed the importance of mechanical history. In an
experiment where the polymer was pre-sheared at 110 sec^{-1}
prior to extrusion, the viscosity was observed to fall to
one quarter of its original value. This mechanical work
caused a temperature rise of 2°C, but the drop in
viscosity was equivalent to an increase in temperature of
20°C.

Both these studies on the effect of thermal history, and

also mechanical history, clearly show that it is an important factor in the rheological properties. The structure of the polymer investigated by Wissbrun appears to contain regions of HBA crystals, which have a higher melting point, and higher viscosity, than the remaining polymer. When the polymer is heated to a high enough temperature, these crystallites are destroyed and the polymer then has a lower viscosity when the temperature is lowered, since the crystallites do not reform.

2.2.6   Temperature Dependence

Using an Instron capillary rheometer, Kiss investigated the effect of temperature on the rheology of a liquid crystalline polymer[44], consisting of three monomers, HBA, IA and HQ. A number of polymers with various compositions were produced using equal fractions of IA and HQ with HBA making up the remaining fraction. Examination of these compositions revealed a minimum in the melting point at a HBA content of 35%.

Three different types of temperature dependence were seen depending on the composition of the polymer. Firstly, at compositions around 35% HBA the viscosity increased with increasing temperature, from 330°C to 370°C, over the full range of shear rates. This was described as a positive temperature dependence. Secondly, for

compositions containing a low percentage of HBA the
viscosity curves produced at different temperatures
intersect. Below the intersection point the viscosity
decreases with increasing temperature, while above this
point it increases. Lastly, for polymers with high HBA
content the previous situation is reversed. At low shear
rates the viscosity increases with temperature, and
decreases with temperature at high shear rates.

The increase in viscosity with temperature for the 35%
HBA polymer is ascribed to the formation of a biphasic
structure. For this to be possible the polymer must
consist of runs of HBA units separated by sequences of
IA/HQ pairs, which then segregate into distinct phases,
an isotropic and an anisotropic phase. As temperature is
increased the volume fraction of the isotropic phase will
increase at the expense of the anisotropic phase. Since
the isotropic phase will have a higher viscosity, the
viscosity of the system increases accordingly.

At the low HBA compositions the polymer is on the
borderline between an isotropic and a thermotropic
polymer. Thus, at low shear rates the polymer behaves in
a conventional manner, viscosity decreasing with
temperature, while at higher shear rates the positive
temperature dependence indicates a liquid crystalline
structure. Therefore, the application of a high shear
rate has the effect of tipping part of the monophasic

isotropic melt into an anisotropic state.

The high HBA polymer also appears to be on the borderline. However, at these compositions the effect of increasing shear rate is to push the biphasic anisotropic melt towards an isotropic monophase system. The polymer then acts like a conventional polymer with viscosity decreasing with temperature.

Although the conclusions drawn by Kiss, relying on a biphasic melt in the liquid crystalline state, are not substantiated by any particular experimental evidence, they are reasonable explanations for the observed behaviour and are in line with the theories presented by Flory[4].

Data on the behaviour of the viscosity of other liquid crystalline polymers as a function of temperature have been reported by Yang and Krigbaum[53]. In these investigations the viscosity was found to decrease with increasing temperature over the shear rate range covered. However, it is possible that in these experiments the polymer remained in the nematic phase, and did not reach temperatures at which an isotropic phase may have formed, and produced an increase in the viscosity.

2.2.7 Normal Stresses

When a polymer melt is subjected to a simple shear flow, a direct stress component normal to the flow boundaries is generated[59]. As mentioned by Brydson[60], normal stresses become important at points in the flow system where there is a change in cross-section. Consequently, they may influence the entry flow of a polymer melt into a capillary, and are usually associated with such features as die swell.

One of the unusual phenomena observed with thermotropic polymers is that of zero, or even negative die swell[51,53,61]. One of the possible explanations for this effect is the occurrence of negative primary normal stress differences (N_1), which have been observed for a number of LCPs[8,52,55].

Looking at an 80% HBA/PET polymer, Gotsis and Baird[52] observed negative values of N_1 at low shear rates which were dependent on both test geometry and temperature. At higher shear rates N_1 became positive and virtually independent of geometry and temperature. Similar studies on a 60% HBA/PET polymer showed only positive values of N_1.

The examination of the die swell of both these polymers provided no direct link with the changes in N_1. For the

60% HBA/PET polymer, values of die swell less than unity were observed when N_1 was positive, and for the 80% HBA/PET polymer the die swell was always greater than one, even at shear rates where N_1 was negative.

Hence, although unusual behaviour is observed for both die swell and the primary normal difference, no consistent correlation between them has been observed.

2.3   Mechanical Properties

2.3.1   Engineering Thermoplastics

Comparing the properties of liquid crystalline polymers with common engineering thermoplastics[62], it can be seen that many LCPs show higher values of tensile strength and flexural modulus, when tested in the melt flow direction. The tensile strength of LCPs is comparable with that of long glass fibre reinforced nylon, being approximately 200MPa. Flexural moduli of approximately 15GPa and 9GPa for glass filled and unfilled versions respectively have been reported[62,63].

The effect of using regrind on the mechanical properties of LCPs has been investigated[18,64]. In a laboratory study, 80% to 100% of the strength and modulus was retained after five mouldings using 100% regrind. However, it was recommended, by the manufacturers, that the regrind be limited to 25% to maintain colour and optimum properties.

In addition to mechanical properties, LCPs also show good high temperature capability. This is reflected in high values of the heat deflexion and continuous use temperature. These are frequently in the range of 170 to 250°C[18,63,65], depending on the polymer.

35

2.3.2 Injection Moulding Variables

2.3.2.1 Injection Rate

Ophir and Ide[66] found that in the moulding of an LCP,
produced from hydroxybenzoic acid, terephthalic acid and
naphthalene diacetate, a slow injection rate gave
improved properties, in the flow direction, compared to a
fast rate. However, one property, the notched impact
strength, showed the opposite effect, having higher
values at the fast injection rate.

Using a copolyester of HBA/HNA, Boldizar[67] measured the
elongation to rupture, the tensile strength and tensile
modulus of bars moulded at four different injection
rates. In general, samples produced at the lower rates,
$1.5cm^3/s$, had improved tensile properties when compared
with samples produced at a rate of $8cm^3/s$, confirming the
results of Ophir and Ide[66]. The elongation to rupture,
however, was less sensitive to injection rate and no
definite conclusions were drawn.

Using three different injection speeds Thapar and
Bevis[68] again found better tensile properties, in the
flow direction, at the slower speeds.

The increase in tensile properties is usually attributed

to two possible factors. Firstly, at the lower injection rate the highly oriented skin layers were thicker, producing a greater proportion of oriented material. Secondly, at high injection rates, turbulence may have occurred, which would counteract the development of orientation.

Thapar and Bevis[68] also investigated the variation of Young's modulus through the thickness of a moulding. This was achieved by producing 1.5mm thick sections cut at known depths from a 20mm thick moulding. It was found that in the flow direction the Young's modulus of the skin layers was considerably higher than that of the core, 12.6GPa and 1.9GPa respectively for an injection rate of 21.43mm/s. Also, as the injection rate was increased, the modulus of the skin layers dropped, while the modulus of the core increased.

This result, in conjunction with the findings that the macroscopic mechanical properties, in the flow direction, also decrease with increase in injection rate, suggests that the macroscopic tensile properties may be dependent on the properties of the skin layers, with the core region playing a minor role. This is consistent with the view that the mechanical properties are related to the amount of material aligned in the flow direction, since the skin layers show orientation in the flow direction while the core shows transverse orientation.

This result is in contrast to those of Williams and Garg[69] who found that it was possible to remove up to 10% of the thickness of the sample without a drop in the tensile modulus, implying that the tensile modulus is not dominated by the outer skin layers.

A slow injection speed is recommended by manufacturers to obtain optimum strength and stiffness in the flow direction[63]. However, it was also noted that, as the injection speed is reduced, so the surface finish of the moulding deteriorates. Hence, a compromise between mechanical properties and surface finish must be reached.

2.3.2.2 Mould Design

The manner in which the polymer flows into and through the mould will play a prominent role in the orientation developed in the moulded article. For this reason the design of the mould, and particularly the gate area, is an important factor.

Boldizar[67] looked at the effect of three different gate geometries, shown in figure 2.6, on the mechanical properties of a HBA/HNA copolymer. Although Boldizar found it difficult to draw any definite conclusions regarding the effect of gate geometry, two factors were noted. Due to the low die swell of LCPs it is important

38
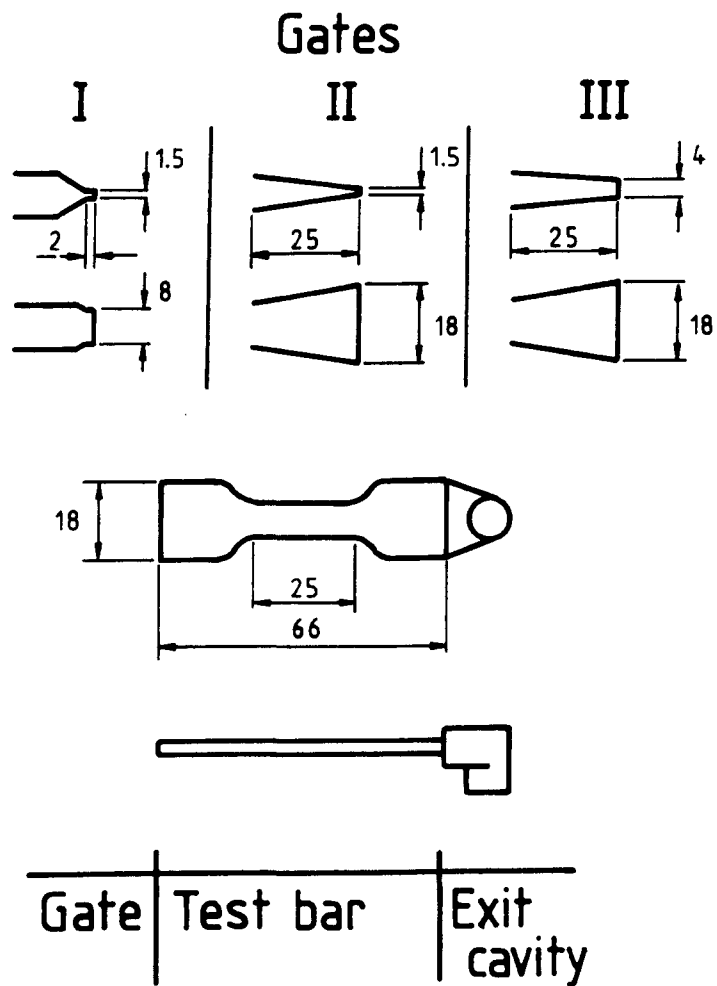
Figure 2.6. Gate geometries employed by Boldizar in the evaluation of the mechanical properties of a HBA/HNA copolymer[67].

that the gate be designed in such a way that upon entering the mould the melt touches at least some part of the mould wall, in order to prevent jetting[63,64,66]. In circumstances where jetting does occur, Folkes[70] has indicated that the mould cavity may be filled in the reverse direction to that anticipated. This will result in multiple weld lines being produced throughout the moulding, which will have a deleterious effect on physical properties. Also a gate which promotes elongational flow will be more effective in producing a high degree of orientation. The strong converging flow in the thickness direction of gate II will facilitate the production of such a flow and hence orientation in the flow direction.

Of the three gate geometries investigated, a conventional thermoplastic gate, gate I in figure 2.6, was found to result in samples with the lowest tensile properties. This gate geometry did not take account of possible jetting, nor the production of a steady converging flow. The best tensile properties were produced by using a much simpler gate design. The width of the gate exit was increased to that of the tensile specimen to prevent jetting, and a consistent converging flow was developed by a gradual narrowing of the gate in the thickness direction.

In addition to altering gate geometries, the effect of an

exit cavity was also examined. This resulted in an
increase in the tensile properties of the bars for all
the gate designs studied. The exit cavity allowed greater
movement of the melt during the injection and holding
stages of the moulding cycle, which promoted a higher
degree and a more homogeneous state of orientation, thus
increasing the tensile properties.

It has also been noted that the location of the gate is
important when designing moulds for LCPs[64]. Multiple
gates are not recommended, due to the formation of weld
lines, which result in weak sections of the moulding.
When weld lines are unavoidable, seam welds, are
significantly better than butt welds[63]. A seam, or knit
weld occurs where one advancing flow front is split by
some obstacle in the path of the flow and then the
separate flow fronts recombine, while a butt weld occurs
where two separate flow fronts meet head on[70].

2.3.2.3 Melt Temperature

The tensile properties of a HBA/HNA polymer examined by
Thapar and Bevis[68] were found to be strongly dependent
on the temperature of the melt during processing. With
the aid of DSC results, this phenomenon was attributed to
the melting transition. At temperatures below the melting
point the melt did not flow suitably to give high

preferred orientation in the mouldings. Increasing the melt temperature improved melt fluidity and eventually produces a melt with a fully developed nematic structure. At this temperature the mechanical properties, in the highly oriented flow direction, reach their optimum values. For the tensile strength Thapar and Bevis indicate a three fold improvement between the two extremes of temperature.

2.3.3 Section Thickness

The effect of section thickness on the mechanical properties has been the subject of investigations by Boldizar[67] and Thapar and Bevis[68]. Results show that as the thickness of a moulding increases its mechanical properties, in the flow direction, decrease. A reduction, by more than a factor of two, in the tensile strength and modulus on going from a 1mm to a 4mm thick section have been reported.

Findings of this nature are usually explained by an overall reduction in the amount of material aligned in the flow direction.

2.3.4 Dynamic Mechanical and Thermal Analysis

The technique of dynamic mechanical and thermal analysis (DMTA) has been widely used to examine the properties of various thermotropic liquid crystalline polymers.

DMTA was employed throughout the 1960s and 1970s to investigate conventional polymeric materials. Much of this work was reviewed by Murayama[71]. It was shown that the shape and location of the transitions were strongly affected by both crystallization and orientation. Results for a HBA/HNA polymer, studied by Wissbrun and Yoon[72] contradict these observations.

Testing relatively poorly oriented moulded samples and highly oriented fibres at the same frequency produced transition at the same temperature. The independence of the transition temperature of macroscopic orientation was interpreted as evidence that the motions, and the environment in which they occur, are not affected by the orientation. This is consistent with the view that the transitions are a result of the individual motion of moieties. Due to the high degree of local order on the microscopic scale the movement of small groups along the chain is essentially unchanged whether or not macroscopic orientation is present.

Troughton, Davies and Ward[73,74] observed three

transitions for compositions of a HBA/HNA polymer. The low temperature transition, occurring around -60°C was ascribed to movement of HBA, while the motion of HNA residues was responsible for a transition at 50°C. A peak in the tan δ plot at about 100°C was shown to be akin to a glass transition type process.

An aggregate model was used to describe the temperature dependence of the tensile and shear moduli. Using a uniform stress (lower bound) model it was concluded that the chain modulus was intrinsically temperature dependent and that imperfect orientation results in the fall in the shear modulus which substantially reduces the macroscopic tensile modulus. Essentially these effects indicate a weakening of the inter chain interactions as the temperature is raised.

The model also provides a novel technique for the evaluation of the chain modulus, E_c, and orientation of the chains with respect to the major flow direction, Θ. These are related to the tensile and shear moduli by the following expression:

$$\frac{1}{E} - \frac{1}{E_c} = \frac{1}{G}(\sin^2\Theta)$$

By plotting a graph of 1/E against 1/G, Troughton et al. calculated the value of Θ, which gave an average chain missalignment of approximately 5°.

2.3.5 Fibre Reinforcement

The effect of the addition of fibrous reinforcement on the mechanical properties of LCPs has not been widely studied. This is in spite of the commercial production of glass fibre reinforced grades of material.

Voss and Friedrich[75] examined the influence of short fibre reinforcement on the fracture behaviour of a bulk liquid crystal polymer. Over a range of mechanical properties, the addition of fibres was found to produce no improvement in properties, in the flow direction, when compared with the LCP matrix material. Using scanning electron microscopy to look at fracture surfaces, the fibre-matrix bond was found to be relatively poor, thus accounting for the lack of improvement in mechanical properties.

In a later paper looking specifically at the impact behaviour Wu, Friedrich and Grosso[76] again found that the addition of fibres reduced the properties in the flow direction. However, the properties in the transverse direction were found to increase, thus decreasing the overall anisotropy of the moulded polymer.

2.3.6 Self Reinforcement

As mentioned previously, liquid crystalline polymers are often referred to as self reinforcing polymers, or SRPs. This description was given credence by Ide and Chung[77] with their work on extruded thermotropic polymer sheets.

Testing the extruded sheets at varying angles to the extrusion direction, it was found that the tensile strength could be fitted to the Tsai-Hill theory for conventional fibre reinforced materials. In addition to this the initial modulus followed the Lees equation. These results suggest that the highly oriented liquid crystal domains may be considered as reinforcing fibres, with the mechanical properties being describable by existing composite theory.

2.4   Structure and Morphology

2.4.1   Development of Orientation

To obtain the best properties from the polymer the
molecules must be highly oriented. Hence the development
of this orientation is of great importance, and has been
the subject of several papers.

2.4.1.1   Shear and Extensional Flow

Viola and coworkers[78] used wide angle X-ray scattering
and electron microscopy to examine the orientation of
sheared and extended samples. Two polymers were
investigated, a 60% and an 80% HBA/PET copolymer.

The sheared samples revealed only slight molecular
orientation which was dependent on the shear rate, higher
rates producing more orientation. This was contrasted by
considerable orientation being produced in extensional
deformation. For example, the degree of molecular
orientation which was produced at an extensional strain
rate of 2.5 s^{-1} was comparable to that produced at a
shear rate of 50 s^{-1}.

Annealing the samples for one minute at 240°C for the 60%

HBA/PET polymer and 300°C for the 80% HBA/PET polymer did
not appear to destroy the molecular orientation developed
during flow. However, in a later paper[54] it was shown
that annealing the 60% HBA/PET polymer at 275°C resulted
in the orientation being greatly reduced after a minute,
and completely destroyed after five minutes. This implies
that at a temperature between 240°C and 275°C, molecular
relaxation is able to take place in this particular
polymer.

SEM examination of etched surfaces revealed a sheet-like
structure in the sheared samples, which was dependent on
the shear stress, and a fibre-like structure in the
extended samples. The fibre-like structure appeared to
relax after annealing, but retained the fibrous texture.
A fibrous texture was also observed by Jenkins and
Jenkins[79] for extruded and drawn fibres produced from a
copolyester.

The observed differences in orientation and morphology
were explained in terms of the domain structure. In shear
flow the domains tumble and rotate at low shear rates and
only tend to align at the higher rates when the domain
structure is broken down to produce a continuous phase.
The extensional flow stretches the individual domains,
all of which then become aligned in the flow direction,
producing a high degree of orientation.

2.4.1.2 Injection Moulding

In a rectangular mould, three major regions of flow have been identified by White[80], shown in figure 2.7. These were described by Garg and Kenig[9] as a spreading radial flow in region one, a converging flow due to the flattening of the melt front in region two, and fountain flow of the melt front in region three, with shear flow occurring at some distance from the mould wall.

The initial spreading radial flow, being a diverging type of flow results in the deceleration of the melt. This produces an elongational flow, with orientation in the transverse direction. The flattening of the melt front which follows in region two results in orientation in the flow direction. The maximum level of orientation obtained in this flow occurs at a point where the melt front assumes a flat, straight line profile.

In fountain flow, the fluid elements from the core of the moulding are elongated while moving along stream lines to the flow front, figure 2.8. These elements reach their maximum state of elongation at the surface of the front, and are deposited on the cold walls of the mould cavity. Since the elements become frozen in this region, a skin develops which is highly oriented in the flow direction.

In the case of non-isothermal flow, where hot polymer is

49
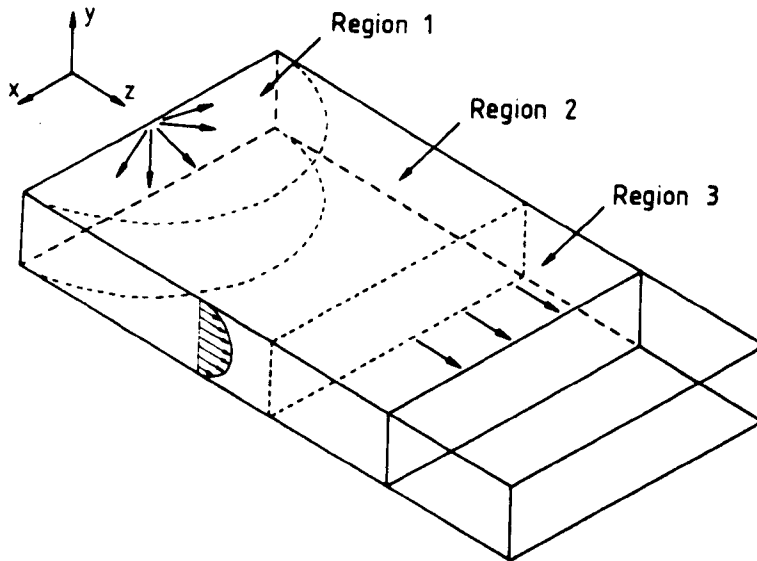
Figure 2.7. Illustration of the three main regions of
flow in the injection moulding process[9,80].
Region 1: Spreading radial flow. Region 2: Converging
flow due to flattening of melt front. Region 3: Fountain
flow at melt front, and shear flow at some distance from
mould wall.
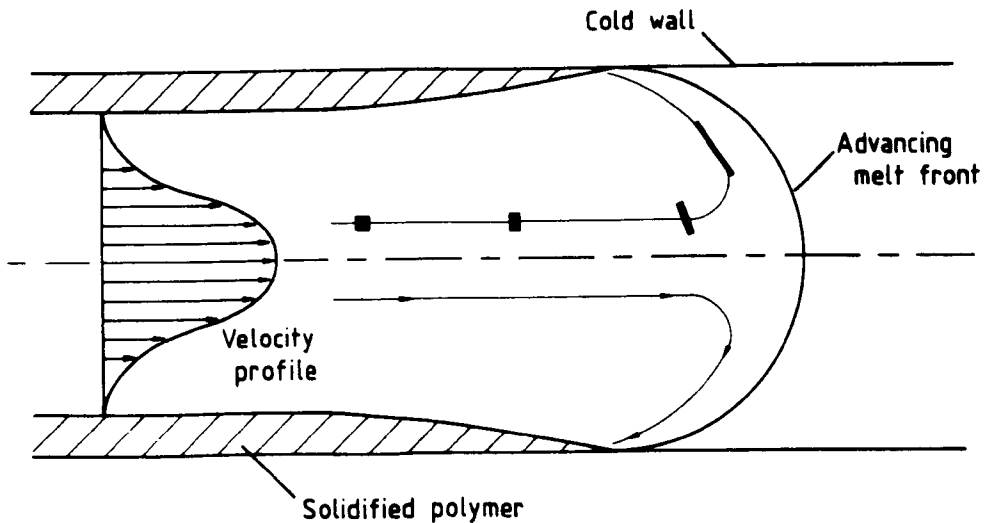
Figure 2.8. Schematic illustration of fountain flow,
showing the deformation of an initially square fluid
element, and the upstream velocity profile.

flowing into a cold mould, it has been shown[80,81] that the velocity profile upstream from the melt front, assumes a shape similar to that shown in figure 2.9a. This profile has an inflexion point due to the lower temperature and higher viscosity of the polymer near the mould wall. This results in the shear rate reaching a maximum at the point of this inflexion, as illustrated in figure 2.9b.

Optical microscopy of mouldings, using reflected light, has indicated the existence of seven layers. However, due to the symmetry of a moulding about the core, the moulding is usually said to consist of four distinct layers, a dark skin followed by a light coloured layer, a dark layer, and a light core[13]. Blundel et al.[82] have noted that the darker layers are more oriented than the lighter ones. The presence of the higher shear rate just below the skin could account for the second dark layer. Viola[78] has shown, as indicated above, that higher shear rates produce greater orientation.

2.4.2 Hierarchical Model

A hierarchical structure, describing different levels of organisation, was proposed by Weng and coworkers[12] after the examination of a HBA/HNA copolymer, which was in the form of injection moulded plaques. A schematic

a. Velocity profile   b. Shear rate profile
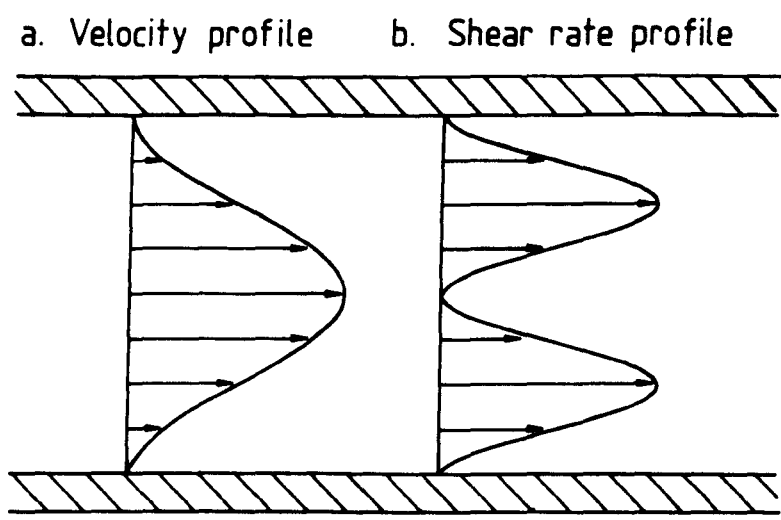
Figure 2.9. The velocity and associated shear rate profile in a flowing polymer melt in the injection moulding process.

illustration of the model is shown in figure 2.10.

On the macroscopic level the structure is divided into three layers, two skins and a core. These are clearly visible to the naked eye by virtue of their different colours. Tensile fracture surfaces indicate skin layers oriented in the flow direction, with a transversally oriented core. The macroscopic layer structure has been reported elsewhere[13,66,83], indicating more than just the three layers, as mentioned in section 2.4.1.2.

At higher magnification, using scanning electron microscopy of fracture surfaces, it becomes apparent that the skin layer is itself divided into a number of layers.

The top layer, approximately 20μm in thickness, was fibrillar in nature and highly oriented. Scanning electron microscopy indicated individual fibrils less than 2μm in diameter. The orientation was investigated by wide angle X-ray scattering (WAXS), and revealed high molecular orientation in the flow direction.

Between this top layer and the core, the structure is divided into sublayers, each approximately 40μm thick. WAXS patterns again indicate molecular orientation in the flow direction, but with weaker reflections than in the surface layer. These sublayers appeared to be further divided into microlayers with a strip like structure,

53
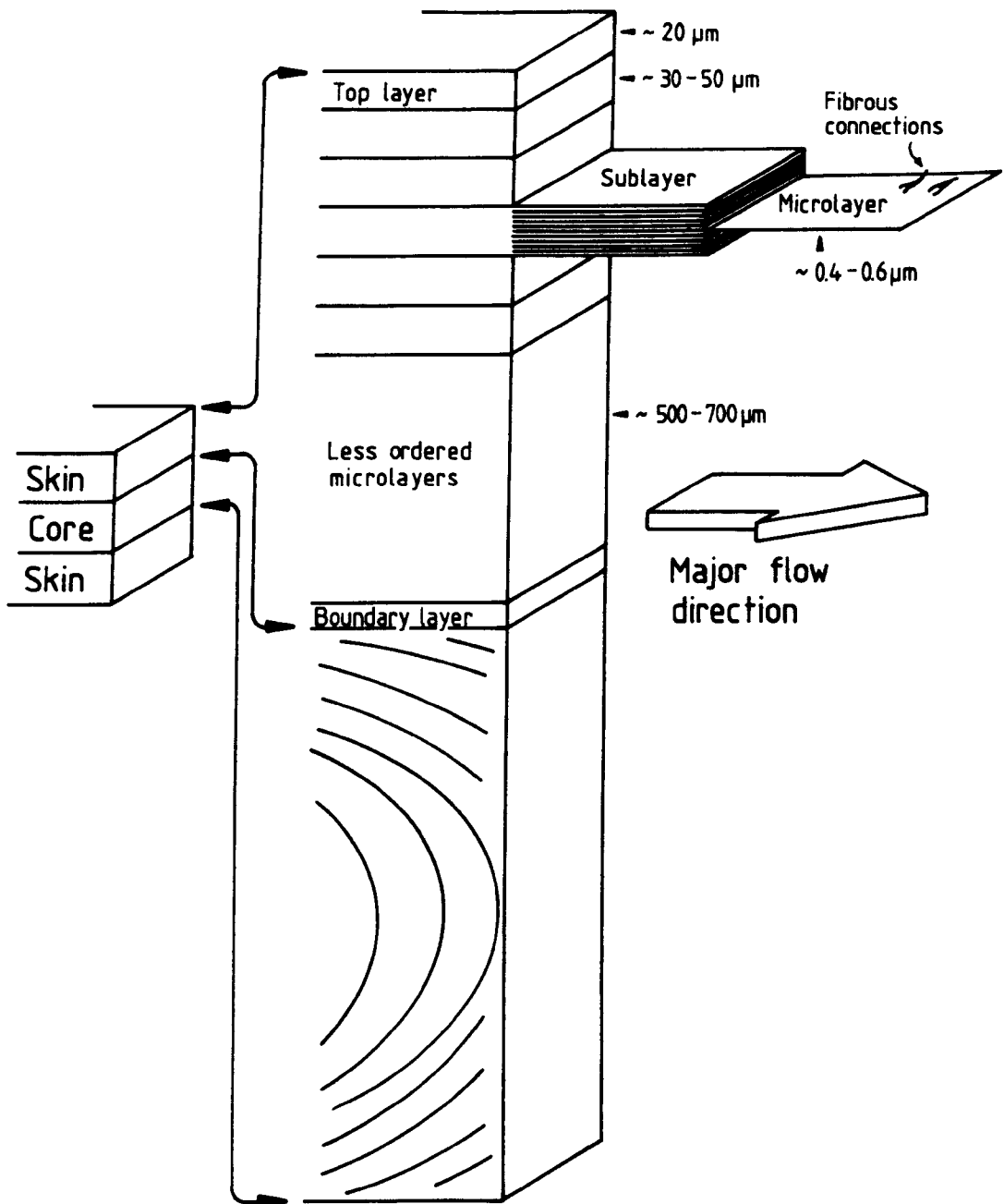
Figure 2.10. Hierarchical model for an injection moulded plaque, as proposed by Weng et al.[12], indicating different levels of organisation.

about 0.5μm thick and ranging from 10 to 30μm in width. Closer examination of the strips revealed a fibrous texture, with the fibres being a few microns wide.

On moving away from the top layer to the core, the microlayers become thicker, 3μm to 5μm rather than 0.5μm, and more fibrous in nature. The average molecular orientation remains in the flow direction, but with reduced order.

Investigations of specially prepared fracture surfaces indicated two types of connections between the microlayers. The first method of cleaving samples at liquid nitrogen temperature revealed strips, less than 10μm wide and 30μm long, similar to the strips observed in the sublayers. The second method involved pulling the layers apart and indicated very thin fibrous interconnections, approximately 0.3μm in diameter.

The core region, occupying approximately one third of the moulding, revealed no structural hierarchical organisation. Tightly packed, parabolic flow lines were clearly visible to the naked eye, apparently arising from the flow pattern of the moulding process. X-ray diffraction examination at several points along the flow lines revealed that molecular orientation was always parallel to these lines. Hence a transverse molecular orientation is observed in the centre of the moulding.

This occurrence is not surprising, as transverse orientation in the core has also been reported for certain short fibre reinforced thermoplastics[84,85].

The hierarchical model was also used to explain the structure of extruded fibres and mouldings by Sawyer and Jaffe[83]. Various methods were employed to examine the structure, including optical and electron microscopy, X-ray diffraction and etching. A representation of the fibre structure is shown in figure 2.11. In this configuration the fibre consists of smaller fibres, the smallest being of the order of $0.05\mu m$.

Sawyer and Jaffe concluded that the microstructure of a broad range of LCP specimens, including fibres, thick extrudates and injection moulded parts, may be described by a hierarchical model which is composed of similar fibrillar subunits.

2.4.3 Layer Morphology

The morphology and composition of the layers, in particular the skin and core, were investigated for a HBA/PET copolyester by Joseph and coworkers[86].

Wide angle X-ray scattering again indicated a highly oriented skin and unoriented core. Electron microscopy of

Skin

Oriented
fibre

5 um   Macro
fibril

0.5 um   Fibril

0.05 um   Micro
fibril
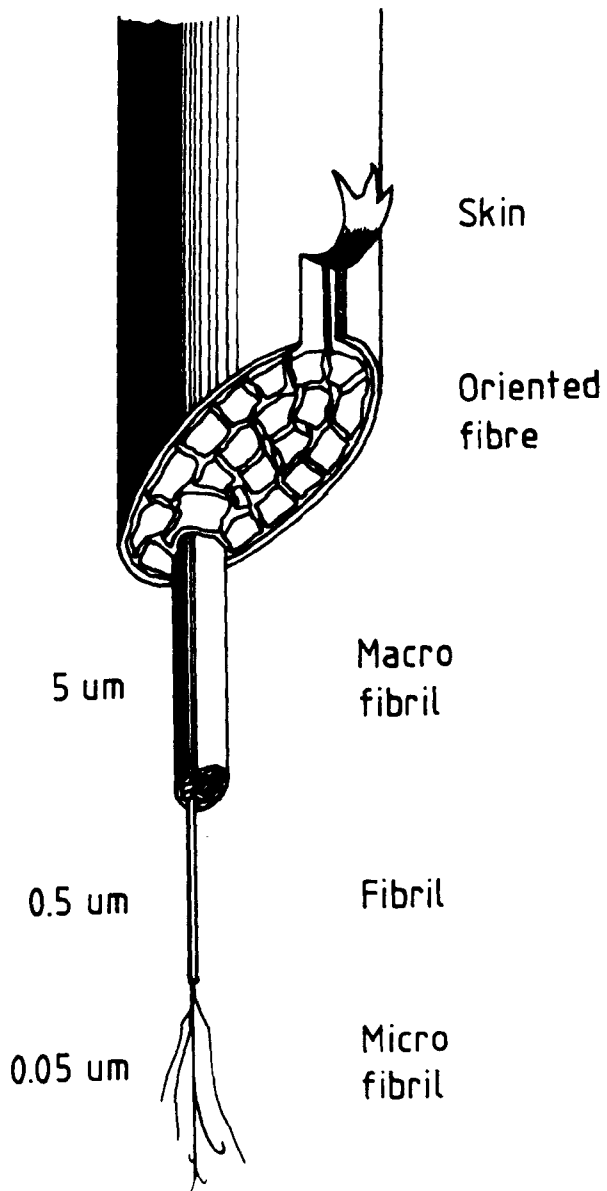
Figure 2.11. Hierarchical structure of extruded fibre,
from Sawyer and Jaffe[83].

sections etched in n-propylamine revealed an elongated structure in the skin, and a core with no discernible structure, although more of the polymer had been etched away. The technique of ESCA (electron spectroscopy for chemical analysis) indicated that the skin region was richer in HBA, while the core contained a higher proportion of PET. This was explained by assuming that the HBA rich regions in the melt were of lower viscosity and migrated to the surface during moulding, while PET rich regions preferentially remained in the core.

Segregation of this nature was also postulated by Kiss[44] for a polymer with HBA as a major constituent, as mentioned in section 2.2.6.

2.4.4 Moulding Parameters

The layer structure, typical of injection mouldings, was investigated in detail by Suokas[13] using a naphthalene based liquid crystalline copolyester. In particular, the effect of various moulding parameters were examined. These included the holding pressure, nozzle and mould temperature.

In general all the mouldings showed a cross section with four layers. Using reflected light microscopy these showed up as a dark skin layer followed by a light layer,

another dark region and finally a light core. Each of
these layers was affected by the variation of the
processing conditions.

Broadly speaking a decrease in mould temperature expanded
the third layer at the expense of the fourth, with the
outer two layers remaining almost constant. The
application of a holding pressure reduced the size of the
second and third layers while increasing that of the
central core region. The lowering of the nozzle
temperature produced insignificant changes in the skin
and the core, but slightly reduced the thickness of the
second layer and increased the thickness of the third
layer.

Suokas paid particular attention to the formation of the
third layer, indicating a relationship between its
thickness and the mesophase glass transition. It was
believed that a supercooling effect enhanced polymer
elasticity due to an increase in internal friction. With
a slow solidification rate and increased viscosity, the
melt has a tendency to align at a fixed angle to the flow
direction, producing a layer with increased orientation.

2.4.5   Etching

The selective etching of various HBA/PET polymers by

Hedmark et al.[87] supports the work of Joseph and coworkers[86].

It was found that n-alkylamines selectively etched the PET rich regions in the polymer. Etched surfaces examined in the electron microscope revealed a Swiss-cheese morphology, indicating a discontinuous PET rich phase in the form of 1-2µm spherical particles. The process of etching was performed on as-received pellets, and 50µm thick films, made by compression. Hence, although no comments could be made on the structure of mouldings, the HBA content of a 50Å thick top layer of the films, for a 60/40 HBA/PET polymer, was found to be 94 mole %.

Chen and coworkers[88] etched oriented films of a copolyester, produced form dicarboxydiphenoxydecane and bromohydroquinone, with an argon plasma technique to reveal a fibrillar structure. The samples were prepared by shearing the polymer between glass slides. This produced zig zag fibrils which ranged from 4µm to 10µm depending on the shear rate. Higher shear rates producing thinner fibrils. Annealing the samples above the melt temperature resulted in a loss of orientation. However, it did not destroy the fibrils. The mechanism by which the fibrils were formed remained unclear.

Thapar and Bevis[68,89] also used an etch technique to examine the morphology of an all para copolyester,

consisting of HBA and HNA. Using concentrated sulphuric
acid as the etchant, a continuous change in topography
was seen on going from the skin to the core, which was
separated into five regions. The skin was composed of
aggregates of thin fibrils. These were approximately
150nm in diameter, and well aligned in the injection
direction. The second region consisted of nodule like
aggregates, followed by a region of nodular fibrillar
material. The fourth layer was again fibrillar, with
diameters greater than those seen on the skin. The core
of the moulding revealed a parabolic profile, but was
neither nodular nor fibrillar in structure.

2.4.6   Banded Texture

Liquid crystalline polymers often show a banded texture
after they have been sheared and cooled to room
temperature. This was first seen in lyotropic
systems[90], but has subsequently been observed in
several thermotropic systems[91], with the bands lying
perpendicular to the shear direction.

Optical microscopy of thin films of thermotropic polymers
revealed an almost sinusoidal variation in the direction
of the molecular long axis[92]. These findings were
supported by the results of electron microscopy[93], and
indicated that the molecules followed a serpentine path

about the shear axis. Later studies, using both optical
and transmission electron microscopy[94], showed that the
periodic variation of the director orientation was
distinctly different, depending on the method of
examination. It was postulated that these differences
were caused by a synchronous rotation of the planar
aromatic groups about the molecular chain axis.

Work by Kwiatkowski and Hinrichsen[95] on samples
prepared by shearing between glass plates revealed the
usual banded textures. However, annealing the samples for
a few minutes produced changes in the structure,
dependent on the thickness of the sample. While the
thinner regions showed no changes and the thicker parts
produced a new vein structure, intermediate regions
formed a 'tractor' or 'herring bone' pattern.

2.4.7 Transmission Electron Microscopy

The technique of transmission electron microscopy (TEM)
has been used to examine molecular orientation. Donald
and Windle[96] have shown that the chains within a domain
lie almost parallel, but from one domain to another there
is typically a 10° mismatch. This change in orientation
results in the formation of walls. There is a strong
tendency for the walls to lie parallel to the original
shear direction, with bend and twist distortions

accounting for changes in orientation.

Although these observations indicate interesting
phenomena, some reservations were indicated. Probably the
most important one is that of surface effects. The
technique of TEM requires very thin sections, typically
less than 100nm, which means that both free and fixed
surfaces may play a crucial role in the molecular
orientation. Thus, results produced in this manner may
not be wholly representative of bulk LCPs.

2.4.8 Crystallinity

The crystallinity of two thermotropic polymers was
investigated by Blundell[97] using thermal and X-ray
analysis. For each polymer, two types of specimen were
prepared. A slow cooled sample, which allowed three
dimensional crystals to form, and a sample which was
quenched from the melt to minimise crystallization.

Thermal analysis indicated that there was very little
difference in the enthalpy of fusion between the quenched
and slow cooled samples. However, the X-ray analysis
indicated that three dimensional ordered structures were
present in the slow cooled sample, while the quenched
sample appeared to be totally amorphous. The degree of
conventional crystallinity in the slow cooled samples was

estimated to be approximately 20% for both polymers.

This apparent anomaly was explained by the presence of microcrystals, less than 30Å across. For conventional polymers such small crystals would be unstable due to the large surface energy involved. However, for the liquid crystalline polymers the surface energy is small, a direct consequence of the molecular morphology in the ordered melt state. This permits the formation of small, stable crystallites.

It was noted that, although the formation of small crystallites in the melt was probable, once they had formed the resultant restriction in movement of the polymer chains would prevent the subsequent growth and perfection of crystals.

These results are supported by the work of Butzbach et al.[98], again using thermal and X-ray analysis. The crystals produced in a HBA/HNA copolymer were found to be imperfect with low values of the enthalpy and entropy of transition, and negligible volume change on crystallization. This latter effect of volume change is partially responsible for the low values of mould shrinkage seen with most LCPs.

The crystallization process was believed to occur in two steps, shown in figure 2.12. The first step, completed in
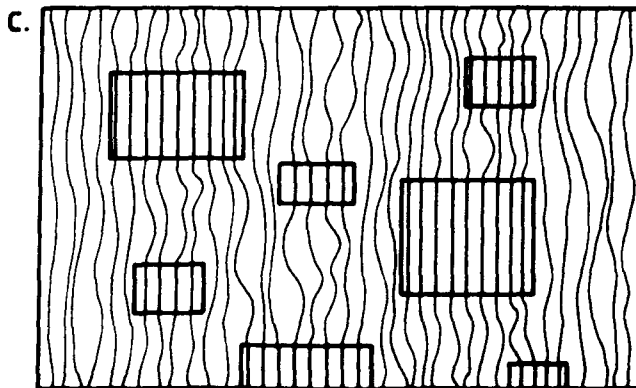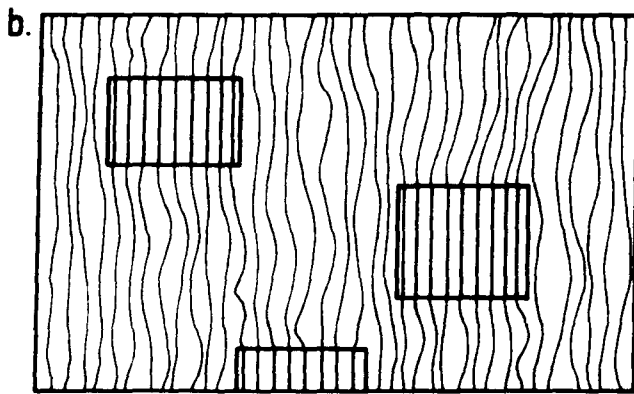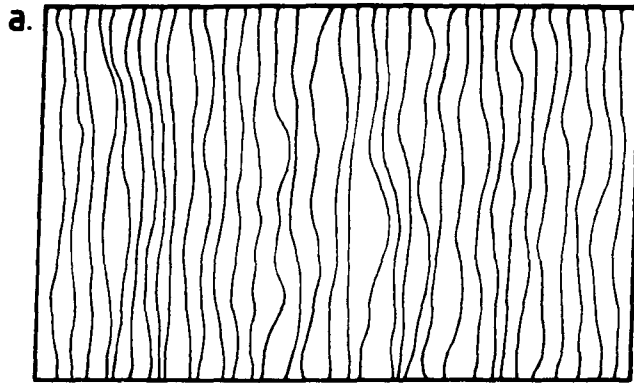
Figure 2.12. Structural model for the formation of crystal, from Butzbach et al.[98].
a. Nematic phase.
b. After rapid transition step.
c. During slow transition step.

seconds, resulted in a two dimensional lattice perpendicular to the direction of the chain axis, with slight registry in the third dimension. Meridional X-ray reflections produced from these units were characteristic of an aperiodic linear array as illustrated in figure 2.13. The remaining part of the sample could then only be transformed into an ordered, crystal structure by a slow diffusional process.

The nature of crystallites in a HBA/HNA copolymer was also investigated by Spontak and Windle[99]. In this study, samples of polymer in the form of ultrathin films, prepared by shearing the polymer on a rocksalt substrate, were examined using transmission electron microscopy. Samples which had been annealed were found to contain randomly distributed crystallites, typically 20 x 60nm, oriented normal to the shear direction. These were identified with aperiodic meridional maxima, indicating that they were non-periodic layer crystallites. Thus confirming the earlier work of Butzbach et al.[98].

The size and shape of the crystallites were found to be dependent on the temperature at which the sample was sheared, the time and temperature of annealing, and the molecular weight of the polymer. A low molecular weight sample, sheared and annealed below the melt temperature produced an estimated degree of crystallinity of 13%.
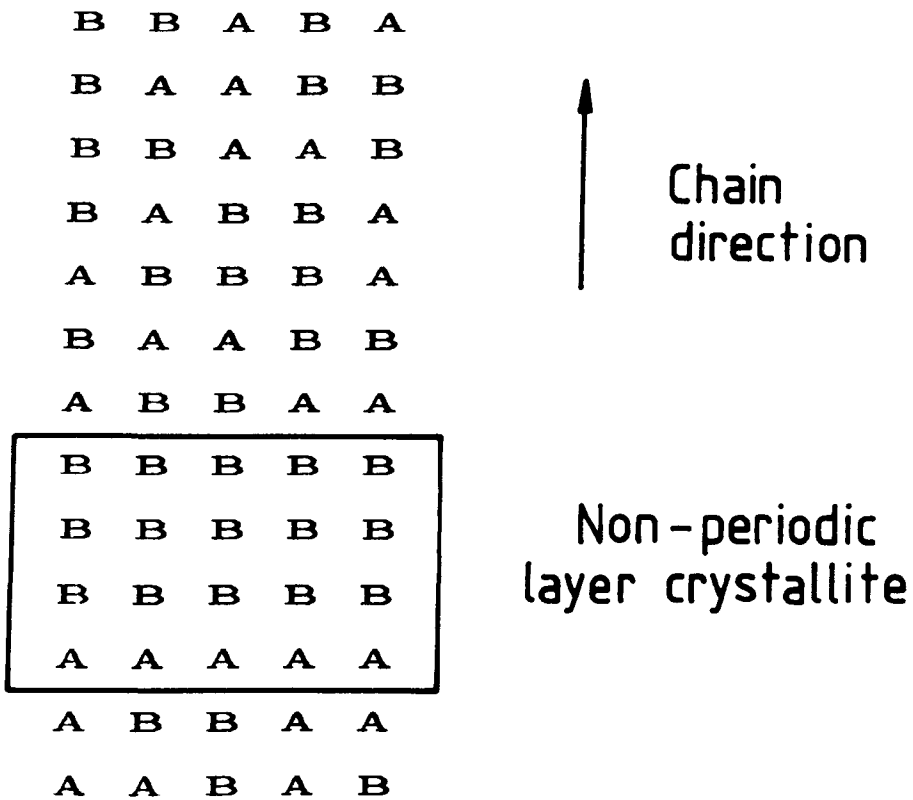
Figure 2.13. Schematic view of a non-periodic layer crystallite[99]. Resulting from longitudinal register of identical sequences of monomer units. A and B represent the different monomers.

2.5   Rheological Models

2.5.1   Capillary Rheometers

Capillary rheometers have been extensively used to evaluate the rheological properties of polymer melts. The method provides rheological data which are relevant to polymer processing, it is able to utilise small quantities of material, and it gives very reproducible results. These are, as mentioned by Cogswell[100], advantageous features of any rheological test method.

Two basic designs of capillary rheometers exist, imposed rate and imposed pressure rheometers, shown schematically in figure 2.14. For the imposed rate rheometers, a plunger is forced into a barrel filled with molten polymer, at a constant rate, and the resulting pressure measured. The pressure may be measured with either a pressure transducer situated just above the die in the wall of the barrel, or by measuring the load on the plunger. If the pressure is deduced from the load on the piston, friction may be a possible source of error. Friction can be eliminated by using gas pressure to extrude the polymer, used in the imposed pressure rheometers. However, measuring the pressure at the point of application may introduce head effects. That is, the measured pressure will contain a term for the pressure
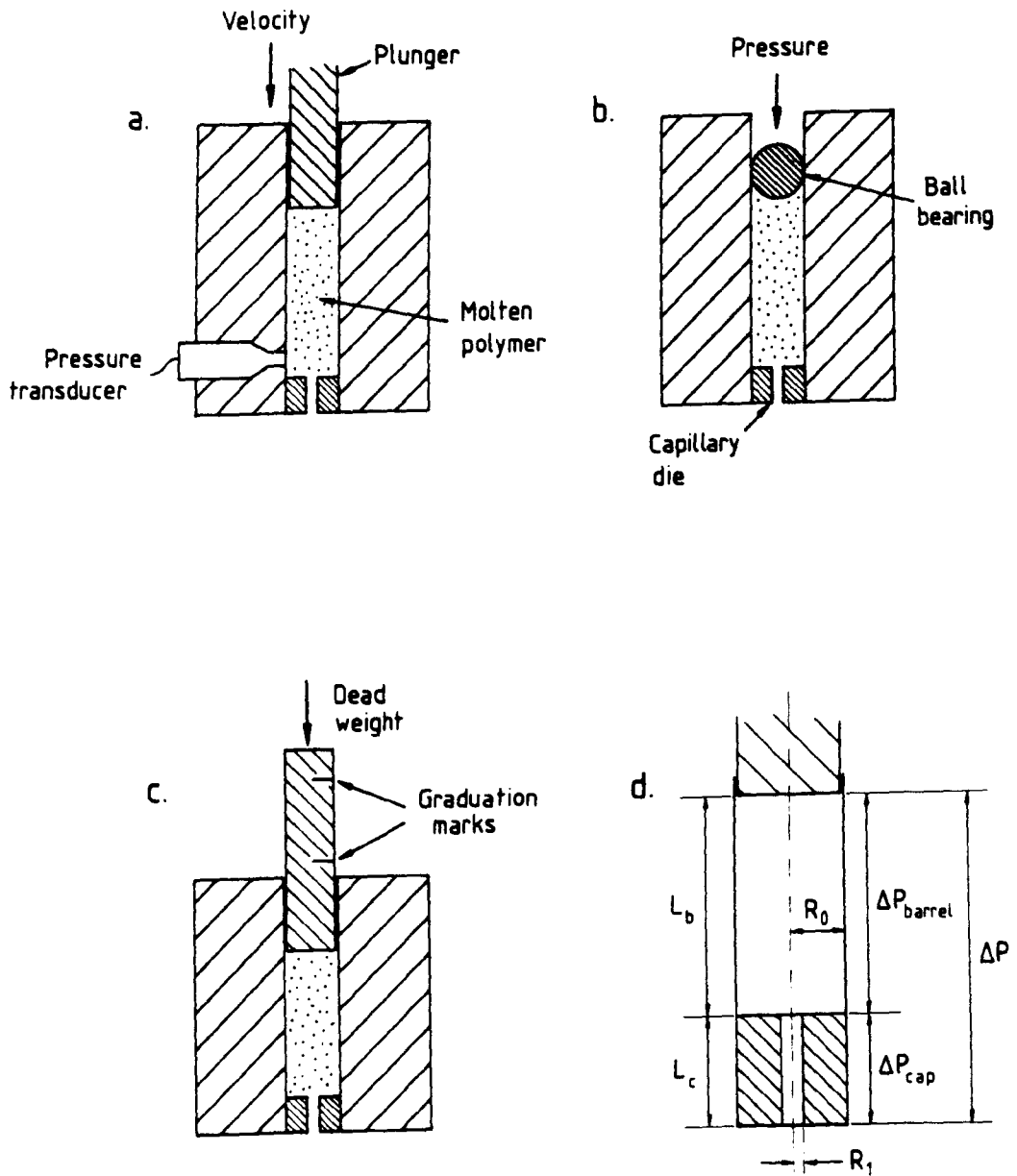
Figure 2.14. Schematic representation of capillary
rheometers.
a. Imposed rate.
b. Imposed pressure.
c. Melt flow indexer.
d. Nomenclature for head effect.

drop in the barrel, as well as in the capillary, shown in figure 2.14d. For a power law fluid, it can be shown that[60]:

$$\frac{\Delta P_{barrel}}{\Delta P_{cap}} = \frac{L_b}{L_c} \left[\frac{R_1}{R_0}\right]^{3m+1} \qquad 2.1$$

where m is the power law index. It is important to keep $\Delta P_{barrel}/ \Delta P_{cap}$ as small as possible, which may be achieved by using long thin capillaries, in conjunction with a large diameter barrel. However, using long thin capillaries may introduce errors due to pressure dependence and shear heating, which will be discussed later. Also, applying a constant pressure to the top of the melt causes the flow rate to increase as the barrel empties, due to a reduction in the head effect. This can be significant in apparatus such as the melt flow indexer, illustrated in figure 2.14c, where the polymer is extruded by the application of a dead weight. Standard tests stipulate that measurements must be made when the piston height is between two specified limits, thus ensuring the same head effect and viscous resistance for each test. In tests where a known pressure or load is applied to the top of the polymer melt, an average volumetric flow rate is usually obtained by weighing the amount of material extruded in a measured time interval.

2.5.2 Capillary Flow

For a Newtonian fluid flowing in a cylindrical capillary,
the pressure drop, ΔP, is related to the flow rate, Q,
by the well known Hagen-Poiseuille equation:

$$\text{Pressure drop} = \Delta P = \frac{8Q\eta L}{\pi R^4} \qquad 2.2$$

It can be shown that the wall shear stress in the
capillary is given by:

$$\text{Wall shear stress} = \tau_w = \frac{R \cdot \Delta P}{2L} \qquad 2.3$$

and that the shear rate at the wall is:

$$\text{Shear rate} = \Gamma_w = \frac{4Q}{\pi R^3} \qquad 2.4$$

In the case of non-Newtonian, and especially power law
fluids, the approximation is sometimes made that the wall
shear rate is given by equation 2.4. In this case the
quantity $4Q/\pi R^3$ is referred to as the apparent Newtonian
shear rate, Γ_A.

Describing the shear flow by a power law relationship, of
the type:

$$\text{Wall shear stress} = \tau_w = G\Gamma^m \qquad 2.5$$

the pressure drop for such a fluid flowing in a capillary

71

can be shown to be:

$$P_{cap} = \frac{2GL}{R_1^{(1+3m)}} \left[\frac{1+3m}{\pi m}\right]^m Q^m$$

$$= \frac{2GL}{R_1} \left[\frac{1+3m}{4m}\right]^m \left[\frac{4Q}{\pi R_1^3}\right]^m \qquad 2.6$$

or

$$\tau_w = G \left[\frac{1+3m}{4m}\right]^m \Gamma_A^m \qquad 2.7$$

A log-log plot of wall shear stress against shear rate
will provide the shear viscosity constants G and m. The
term (1+3m)/4m is referred to as the Rabinowitsch
correction[60], and is required when the approximation
$\Gamma_w = \Gamma_A$ is made.

2.5.3 Entry and Exit Pressures

It has been pointed out that the capillary is not
infinitely long[101], and as a result, the pressure
losses at the entrance and the exit can contribute
significantly to the total pressure drop. These effects
are especially significant with polymeric liquids.

Figure 2.15a shows a schematic plot of pressure against
distance for a polymer flowing through a capillary.
Although the exact shape of the curve around z = 0, and
z = L is open to question, the general features of the

plot have been confirmed experimentally by Han[102].
Thus, the total pressure drop, measured in the reservoir
of a capillary rheometer, can, to a good approximation,
be regarded as a combination of three factors, an entry,
a capillary and an exit pressure.

Han investigated the pressure distribution found with two
fluids which had approximately equal shear viscosities.
The first was molten polyethylene, at 180°C, the other
was a Newtonian liquid, Indopol H-1900, at room
temperature. It was found that the polyethylene gave rise
to significant entry and exit pressure values, while
these effects were found to be quite small with the
Newtonian liquid. Han concluded that the large entry
pressure was associated with the elastic properties of
the polymer melt. The origin of these large entry
pressures has been the subject of much discussion. We
shall assume here that they involve high extensional
viscosities, which are associated with the orientation of
chain segments, or other entities which have a high
resistance to extensional flow[103].

2.5.4 Correction Factors

One of the most commonly applied correction factors is
the Bagley correction[104]. As can be seen from figure
2.15a, substituting the upstream pressure into equation

73
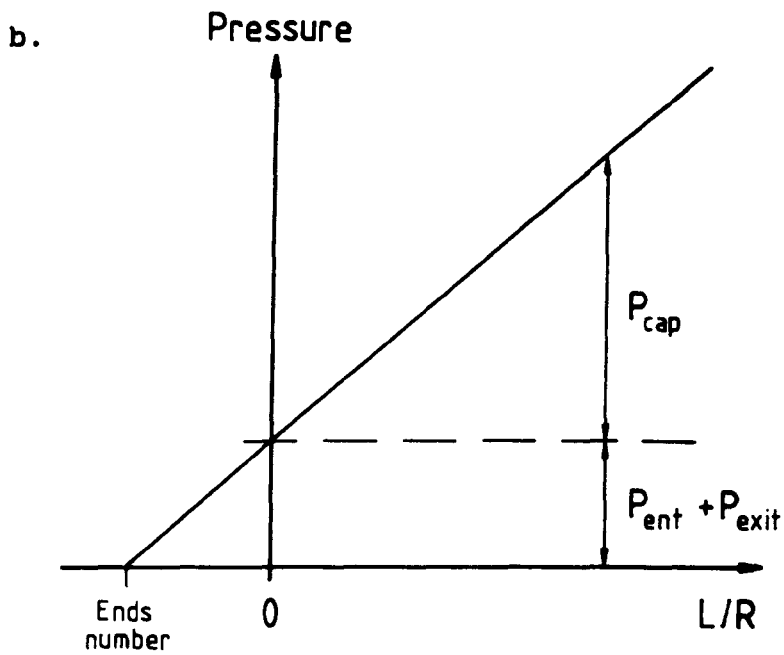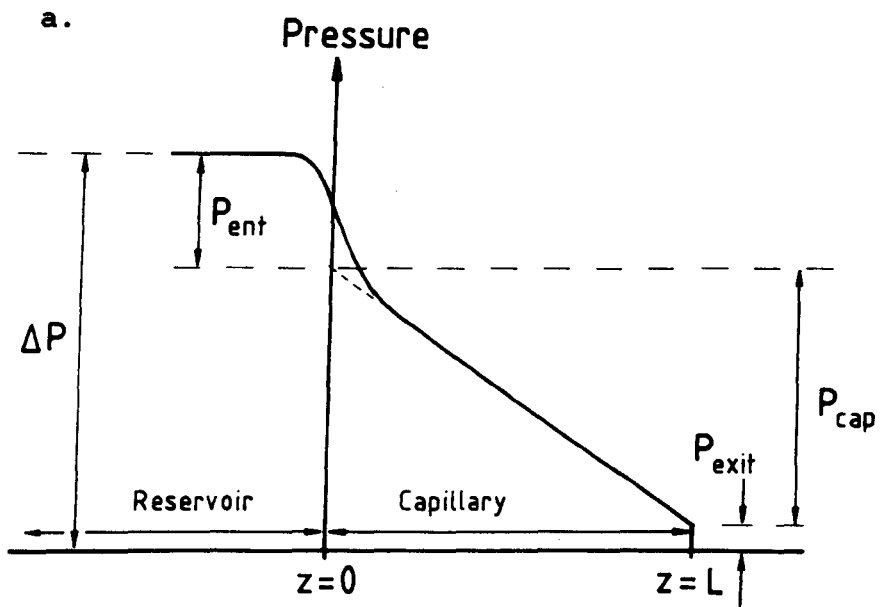
Figure 2.15. Capillary flow,
a. Pressure distribution in the reservoir and capillary
   of a capillary rheometer.
b. Bagley plot.

2.3, will overestimate the value of the capillary wall
shear stress. For this reason, the capillary pressure,
needed to calculate the actual wall shear stress, must be
deduced. Bagley, working with different grades of
polyethylene, found that plots of total pressure against
the capillary L/R ratio were linear. Extrapolation of
these plots to L/R = 0, enabled the sum of the entry and
exit pressures to be separated from the capillary
pressure, as shown in figure 2.15b.

Although the Bagley correction does not allow the entry
and exit pressures to be calculated separately, the exit
pressure term is usually small in comparison to the entry
pressure. At a shear rate of $330s^{-1}$, and an L/R ratio of
16, Han found that the entry pressure for polyethylene
constituted approximately 22% of the total pressure,
while the exit pressure amounted to less than 4%[102].
Hence, for the purpose of this work we assume that P_{ent}
is very much greater than P_{exit}, and equate the Bagley
correction with the entry pressure drop.

Another correction factor usually applied to capillary
rheometry is the Rabinowitsch correction[60], mentioned
in section 2.5.2. This takes into account the non-
parabolic nature of the velocity profile, and permits the
calculation of the true wall shear rate, rather than the
apparent shear rate, as given by equation 2.4. Describing
the polymer melt as a power law fluid, equation 2.5, the

Rabinowitsch correction may be written as:

$$\text{True shear rate} = \Gamma = \left[\frac{3m+1}{4m}\right]\frac{4Q}{\pi R^3} \qquad\qquad 2.8$$

The magnitude of (3m+1)/4m varies as m goes from 1 to 0, with a maximum error of 15% in the calculated viscosity, occurring when m = 0.23, if the correction factor is not taken into account[100].

Other sources of error, which are more difficult to correct for, are those due to pressure and temperature effects. Polymer melts are slightly compressible, and Cogswell[100] has noted that a pressure of 10^8 Nm^{-2} will typically cause a 10% increase in density. On progression down the reservoir and down the capillary, the reduction in pressure causes the melt to expand. Brydson[60] suggests that this may result in the flow rate on emergence from the die being 10% greater than that calculated from readings of piston displacement. Also, pressure increases the viscosity of polymer melts, the viscosity at a pressure of 10^8 Nm^{-2} may be 2 to 5 times greater than that at atmospheric pressure.

The decrease in pressure during extrusion leads to a reduction in the average melt temperature, which, according to Cogswell[100] may be of the order of 15°C for a pressure gradient of 10^8 Nm^{-2}. The viscous dissipation in the capillary also gives rise to an

increase in temperature. The volume average temperature
rise is directly proportional to the pressure drop, and
may be as much as 40°C for a 10^8 Nm^{-2} pressure drop. This
is particularly significant in regions of high shear near
the die wall, and causes a reduction in the viscosity. In
addition to this, there is also a sudden increase in
temperature when the melt is compressed[100].

It is fortuitous that these effects are, to a large
extent, mutually cancelling. However, these sources of
errors may be kept to a minimum by not using dies with
excessively long capillaries. A maximum L/R ratio of 32
is usually employed.

2.5.5 Elongational Flow

Although the shear viscosity, as outlined above, is
relatively straightforward to evaluate using capillary
rheometry, the determination of the parameters associated
with extensional flow are more difficult to ascertain. A
number of methods[60] have been proposed, but these have
so far met with only limited success. Many of these
methods involve the extension of a sample of polymer
under a defined deformation mode, usually constant stress
or strain rate. The main problems with these methods are
the difficulty of clamping a sample of essentially molten
polymer at either end, and the tendency of the rod to

neck as it is drawn. A method of continuous drawing or spinning would appear more suitable, but the considerable variation in elongation rate with position along the spinline makes the interpretation of results difficult[60].

Another possible method of examining elongational flow, that is potentially useful, is to observe that a substantial part of the flow regime in a die entry is convergent, and to resolve the convergent flow in a capillary rheometer into a shear and an extensional component. This method has the advantage that it utilises existing rheological equipment. It has the ability to study high elongational rates, with the production of reproducible results over a wide temperature range. However, the principal objection to this method has been the lack of rigorous analysis[60]. A number of models have been proposed to describe die entry flow, some of which will be described below, but none have as yet been universally accepted.

2.5.6 Cogswell Model

One of the early models was proposed by Cogswell in 1972[105]. In this model, Cogswell described the shear flow by a power law relationship, and the elongational flow by an apparent Newtonian relationship, i.e. n = 1.

By resolving the forces on the elements shown in figure
2.16a, the following expressions for the shear and
extensional contributions to the entry pressure in a
conical convergent die were obtained:

$$P_s = \frac{2G}{3m \cdot \tan\alpha} \left[\frac{1+3m}{4m}\right]^m \Gamma_A^m \left[1 - \left[\frac{R_1}{R_o}\right]^{3m}\right] \qquad 2.9$$

$$P_e = \frac{\eta_{eA} \cdot \tan\alpha}{3} \Gamma_A \left[1 - \left[\frac{R_1}{R_o}\right]^3\right] \qquad 2.10$$

where η_{eA} is the apparent extensional viscosity.

The above model has been found to describe the entry
pressure, $(P_s + P_e)$, in constrained flow quite well at
low die angles, up to about 45°. Above this angle,
problems arise because 'flat slab' analysis gives values
of $\tan\alpha$, and hence P_{ent}, which go to infinity at $\alpha = 90°$,
shown in figure 2.16b.

Cogswell attempted to adapt the model to describe the
unconstrained flow that occurs at a flat entry die, i.e.
$\alpha = 90°$. It was assumed that the melt would form its own
convergence angle, and flow through a region, bounded by
an angle α_o, such that the pressure drop was a minimum.
This yielded the following expressions for the entry
pressure and the convergence angle:

79
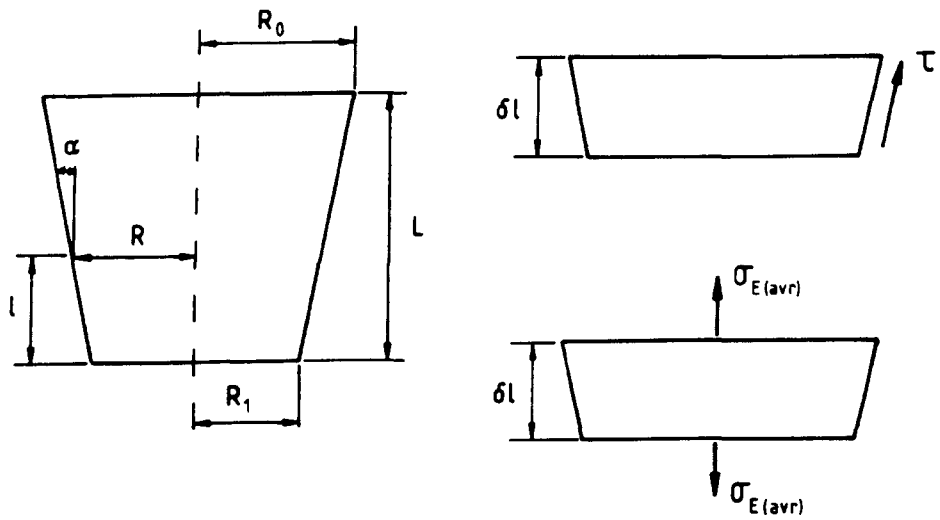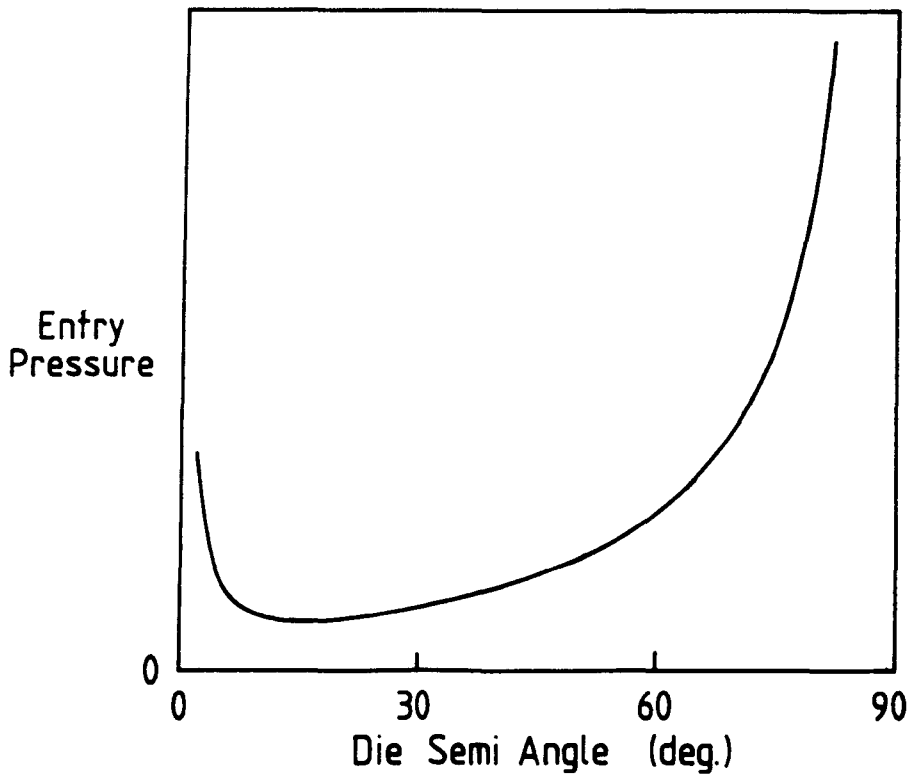
Figure 2.16. Cogswell model.
a. Fluid elements and force balance[105].
b. Plot of entry pressure vs. die semi angle, calculated
   using equations 2.9 and 2.10.

$$P_{ent} = \frac{4\sqrt{2}}{3(m+1)} \Gamma (\eta_s \eta_e)^{\frac{1}{2}} \qquad\qquad 2.11$$

$$\tan \alpha_o = \left[\frac{2\eta_s}{\eta_e}\right]^{\frac{1}{2}} \qquad\qquad 2.12$$

Although the unconstrained version of Cogswell's model can be used to obtain approximate values of extensional viscosity, if results are obtained covering a range of die angles the viscosities obtained using equation 2.9 and 2.10 at low die angles and equation 2.11 at $\alpha = 90°$ are not consistent. This anomaly may arises from the assumption that the velocity at the boundary of the converging zone is zero. In the real flow, the point of zero axial velocity will be within the recirculating zone, and taking a zero boundary velocity neglects the energy dissipation which occurs in the recirculating, or dead zones of a die with a large semi angle. As a consequence of this, use of Cogswell's model is normally limited to low die angles, usually less than 45°.

2.5.7 Binding Model

In a paper on contraction and converging flows, Binding[106] employed energy principles to relate the entry pressure drop to flow rate. Binding considered the flow through a circular channel shown in figure 2.17, and used power law relationships to describe both the shear

81
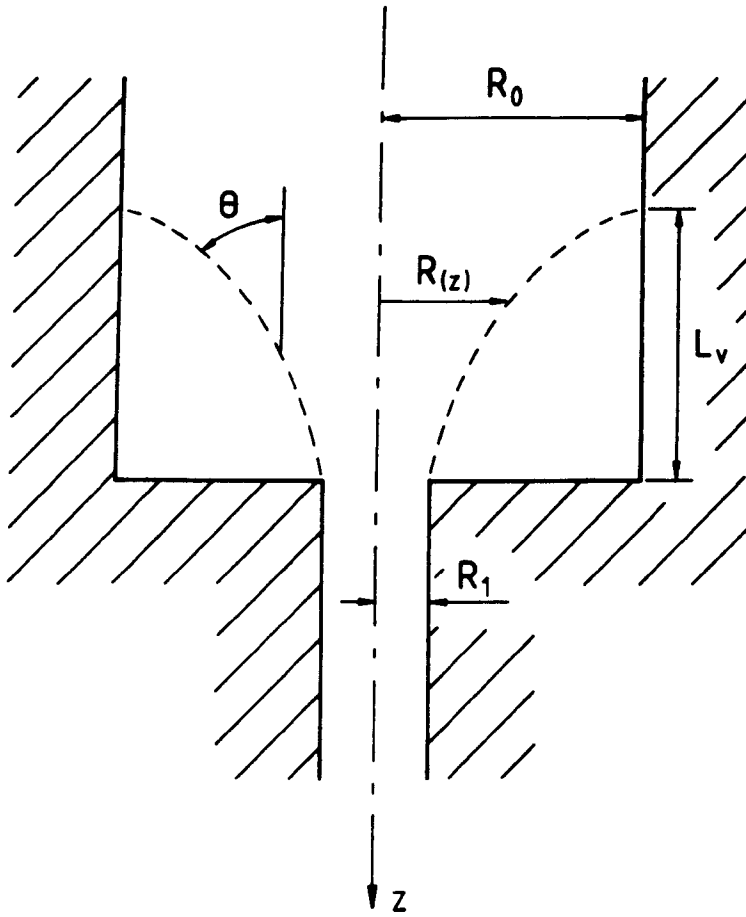
Figure 2.17. Die entry flow as proposed by Binding[106], indicating the vortex length, Lv, and the convergence angle, θ.

and extensional viscosities. By evaluating and minimising the energy dissipation in the converging region, the following expression for the entry pressure was obtained:

$$P_{ent} = \frac{2G(1+n)^2}{3n^2(1+m)^2} \cdot \left[\frac{Hn(3m+1)m^n I}{G} \right]^{1/(1+n)}$$

$$\cdot \Gamma^{n(m+1)/(1+n)} \left[1 - \left[\frac{R_1}{R_0} \right]^{3n(m+1)/(1+n)} \right] \qquad 2.13$$

where I is a numerically evaluated integral, given by:

$$I = \int_0^1 \left[\left| abs \left| 2 - \left[\frac{3m+1}{m} \right] \Phi^{1+1/m} \right| \right]^{n+1} \Phi \, d\Phi \qquad 2.14$$

In a later paper[107], Binding used the theory to examine the flow of several polymer solutions. Although the theory gave good prediction of the vortex length for some solutions, it was concluded that more work was required. It should also be noted that polymer melts were not investigated. As with Cogswell's model, Binding neglects the energy dissipation in the recirculating zones, which again may produce errors at large die angles.

2.5.8 Gibson Model[108,109]

The problem of the recirculating zones was overcome by

83

Gibson who considered the flow of material crossing a spherical surface in the entry region, which was not limited to an optimum region of convergent flow, as with the previous models.

Although this approach ignored the possibility of recirculation zones being present, it was argued that the overall extensional contribution to the pressure drop was not a strong function of the shape of the velocity profile. It was therefore felt that the model would give a reasonable relationship between the pressure drop and extensional viscosity, even in the case where recirculation does occur.

The capillary die was divided into three regions as shown in figure 2.18. The entry zone is divided into two parts: region A, between the spherical boundaries at $r = r_0$ and $r = r_1$, and region B, between the boundary $r = r_1$ and the flat entrance to the capillary.

In each region the pressure drop contains a contribution from shear and extensional flow. The relevant expressions for the shear and extensional contributions are given in table 2.1. The contribution of region B to the overall pressure drop is only significant at large die angles, and the shear component in this region is small enough to be neglected. $\Phi(n,\alpha)$ is an integral which must be evaluated numerically. A table of values of $\Phi(n,\alpha)$ for a
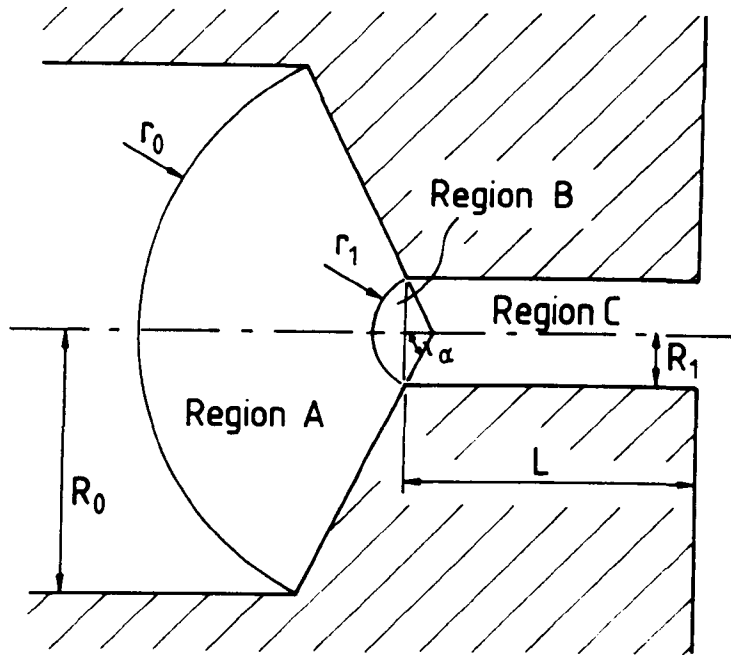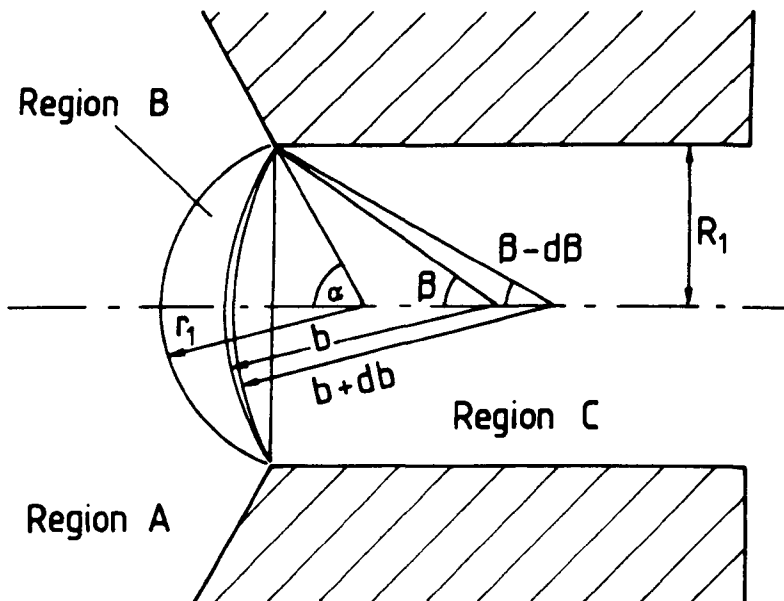
Figure 2.18. Die nomenclature for the Gibson model[108].
a. Die geometry for capillary flow, indicating the
   position of regions A, B, and C.
b. Geometry of region B, showing the nomenclature used in
   deriving the pressure drop, P_{Be}.

Table 2.1. Equations for the shear and extensional components of the pressure for the three regions in the Gibson model.

REGION	SHEAR COMPONENT	EXTENSIONAL COMPONENT
A	$P_{As} = \dfrac{2G\Gamma^m \sin^{3m}\alpha}{3m\alpha^{(1+3m)}} \left[\dfrac{1+3m}{4m}\right]^m \left[1 - \left[\dfrac{R_1}{R_0}\right]^{3m}\right]$	$P_{Ae} = \dfrac{2G\epsilon^n}{3n} \left[1 - \left[\dfrac{R_1}{R_0}\right]^{3n}\right]$
B	$P_{Bs} \approx 0$	$P_{Be} = \dfrac{H\Gamma^n}{4^n} \cdot \Phi(n,\alpha)$
C	$P_{cap} = P_{Cs} = \dfrac{2GL}{R_1} \cdot \left[\dfrac{1+3m}{4m}\right]^m \cdot \Gamma_A^m$	$P_{Ce} = 0$

range of n values and die angles was produced by Gibson[109]. The total entry pressure is given by $P_e + P_s$, while the overall extensional contribution to the pressure, P_e, is given by $P_{Ae} + P_{Be}$.

This model has been extensively used by Gibson and coworkers[108,109,110,111] to model the flow behaviour of several engineering polymers. Over a wide range of shear rates and die angles, the model has been found to be capable of describing, fairly closely, the experimentally obtained entry pressures.

2.5.9 Batchelor Equation[112]

In connection with this work it will be necessary to consider the effect on extensional viscosity of the presence of elongated entities, such as fibres or crystalline domains.

Batchelor derived a model for the stress generated by the pure straining motion of a suspension of particles in a Newtonian fluid. The extensional viscosity of the suspension may be described by the following equation:

$$\eta_{eF} = \eta_{sR} \left[3 + \frac{4}{3} V_f \frac{(L/D)^2}{\ln(\pi/V_f)} \right] \qquad 2.15$$

87

where η_{eF} is the extensional viscosity, η_{sR} is the shear viscosity of the fluid which separates the particles, which have volume fraction V_f, and an aspect ratio of L/D. Where the particles are separated by a non-Newtonian fluid, equation 2.14 may be modified to take account of the contribution due to a higher than ideal extensional viscosity in the suspending fluid[103]:

$$\eta_{eF} = V_R \cdot \eta_{eR} + \frac{4}{3} \eta_{sR} \cdot V_f \cdot \frac{(L/D)^2}{\ln(\pi/V_f)} \qquad 2.16$$

where η_{eR} is the extensional viscosity of the suspending fluid and V_R is the volume fraction of the fluid.

The Batchelor equation is usually restricted to dilute suspensions, with volume fractions in the range of 0.01. However, McClelland and Gibson[103], working with glass fibre filled nylon, have indicated that the equation may well be applicable, to a good approximation, to much higher volume fractions.

The model has also been successfully used to predict the effective aspect ratio of fibres in a thermoplastic matrix[103,111]. Knowing the extensional viscosity of the fibre reinforced polymer, η_{eF}, and the shear viscosity of the base polymer, η_{sR}, the Batchelor equation may be used to find an estimate of the effective aspect ratio, (L/D), of the flowing unit.

88

CHAPTER 3

Experimental and Data Treatment

3.1   Materials

The polymer under investigation was a liquid crystalline polymer produced by ICI. Two grades from the SRP1 range were examined, and are referred to as SRP1500G, a general purpose injection moulding grade, and SRP1500GL30, an equivalent grade with 27% glass reinforcement.

This polymer is produced from four monomers, para-hydroxybenzoic acid (p-HBA), hydroquinone (HQ), isophthalic acid (IA) and hydroxynaphthoic acid (HNA). These are shown schematically in figure 3.1.

.

para-Hydroxybenzoic acid

HOOC—⬡—OH   — HBA

Hydroquinone

HO—⬡—OH   — HQ
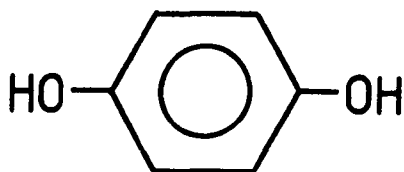
Isophthalic acid
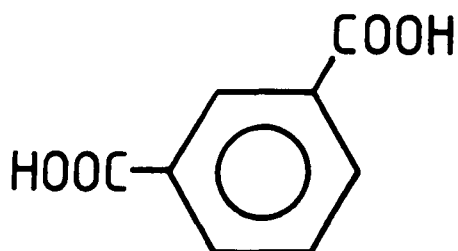
HOOC—⬡(COOH)   — IA

Hydroxynaphthoic acid
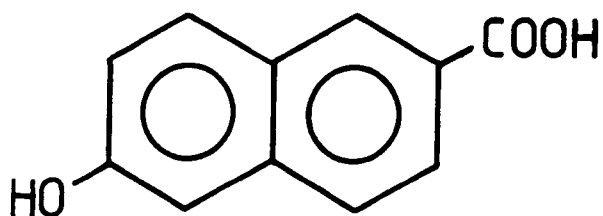
HO—⬡⬡—COOH   — HNA

Figure 3.1. Schematic representation of the four constituent monomers used in the production of SRP1.

3.2   Rheology

3.2.1   Laboratory Rheometer

Two laboratory rheometers were employed in this study.
One, a free standing Davenport with a barrel diameter of
22mm, operated at Liverpool. The other, at ICI Wilton,
was a bench top machine with a barrel diameter of 19mm. A
schematic diagram of a capillary rheometer is shown in
figure 3.2.

Since the polymer is essentially a polyester it was
necessary to carefully dry the granules before charging
the rheometer. Ester groups are susceptible to
hydrolysis[113,114], breaking down the polymer at random
points along the chain. The speed and extent to which
hydrolysis damage occurs depends principally on water
content, time and temperature. Hence, it is important to
dry the polymer prior to the experiment to minimise
hydrolytic degradation.

Drying was achieved by placing trays of the polymer in a
vacuum oven at 120°C for at least two hours. With a
suitable die in position and the barrel set at the
required temperature, small quantities of the polymer
were removed from the oven and the barrel charged as
quickly as possible. This was necessary in order to
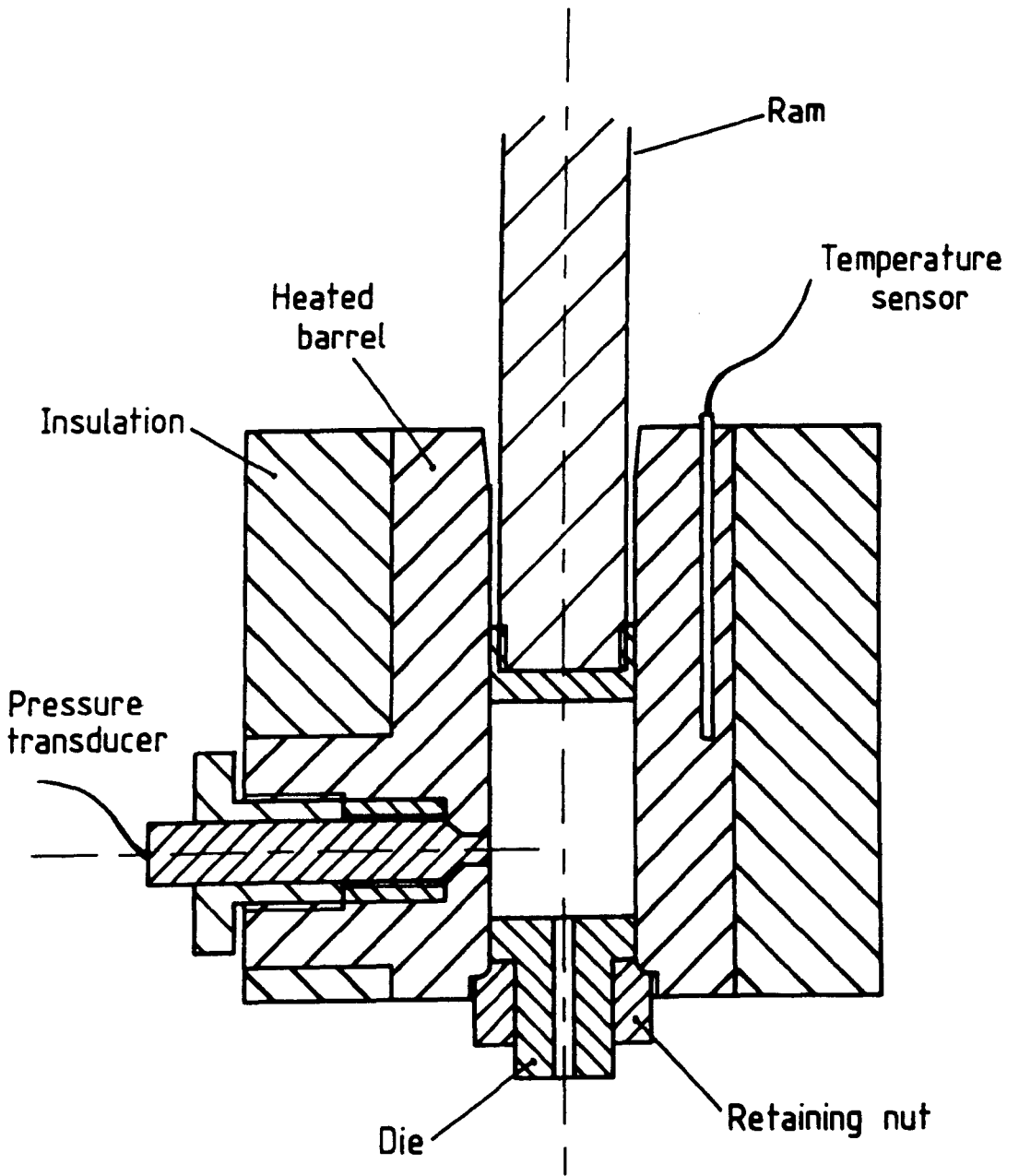
Figure 3.2.   Schematic diagram of laboratory rheometer.

minimise moisture pickup by the polymer which could affect results. Once charging had been completed the temperature was allowed to equilibrate. For the Liverpool rheometer this was achieved by a stand time of 20 minutes, while for the smaller ICI barrel a 15 minute stand time was sufficient.

Once the temperature had equilibrated the ram was moved vertically downwards to force the polymer through the capillary of the die. When the pressure had reached a steady value it was recorded, along with the velocity of the ram. The velocity was then increased to produce a higher shear rate and when the pressure had once again stabilised it was noted down along with the velocity. This procedure was repeated until the full barrel charge had been used.

After each run the ram was withdrawn from the barrel and any residual polymer removed from both it and the barrel using wire brushes, after which the ram and the barrel were polished with gun cloth. The die was then replaced with one of a different capillary length ready for the next run.

3.2.2   Injection Moulding Machine

In addition to the work performed on the laboratory

rheometers some rheology was carried out on an instrumented injection moulding machine. This was a Stubbe SKM 76-110 equipped with a linear velocity transducer, to measure the linear speed of the screw, and a pressure transducer to measure the pressure drop at the nozzle. This is shown schematically in figure 3.3.

As in the case of the laboratory rheometer, the polymer was dried prior to the start of the runs. However, since this rheological method is employed to investigate the flow behaviour under injection moulding conditions, the polymer was dried as if it were being prepared for moulding. Hence it was placed in an air circulating oven at ambient pressure and a temperature of 150°C for four hours.

The injection moulding machine conditions in operation during the rheological measurements were as follows;

Barrel temperatures (°C)	rear	320
	middle	330
	front	340
	nozzle	340
	die	340
Screw speed (rpm)		180
Back pressure (bar)		0

During the charging process, the exit of the die was blocked to prevent drooling, thus allowing the charge to build up. For the capillary dies this was achieved with

94
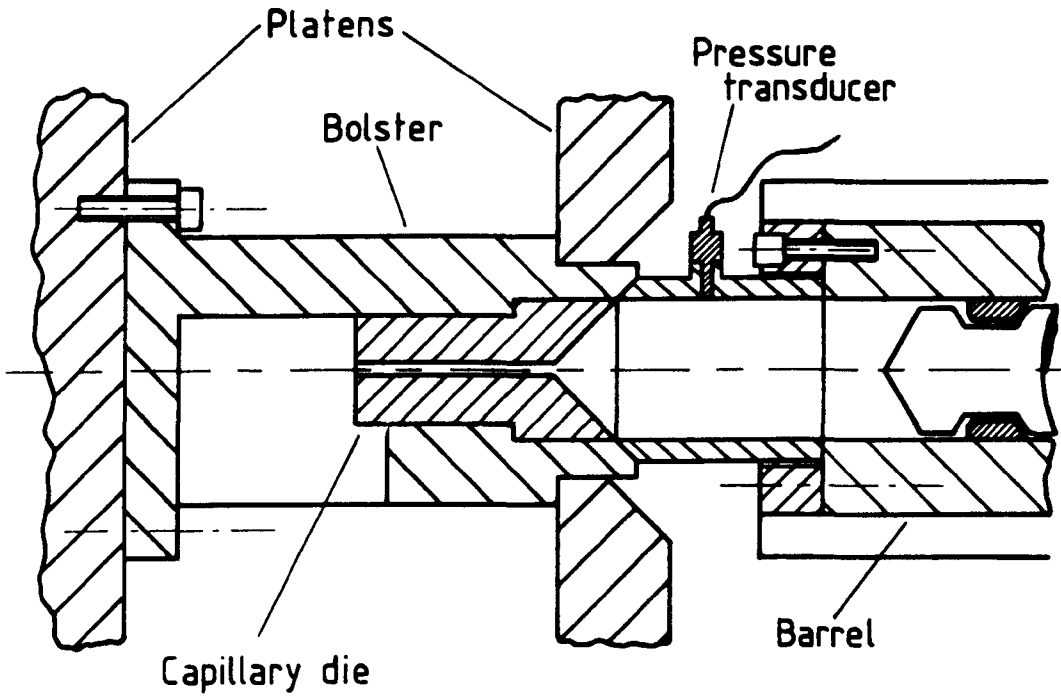
Figure 3.3. Diagram of the rheometer head used in conjunction with the injection moulding machine.

the use of a tapered brass rod which was secured in the
exit of the capillary, shown in figure 3.4.a. This method
was unsuitable for orifice dies, because of possible
damage to the orifice diameter, and so a flat disk of
metal was wedged over the exit surface of the die,
illustrated in figure 3.4.b.

Once charging was complete the melt was left for a few
minutes to reach constant temperature after which the die
exit was unblocked and the polymer injected through the
die. The pressure drop and linear velocity of the screw
were recorded using a chart recorder. The barrel was then
charged again, the linear velocity setting of the screw
increased and another charge of polymer injected through
the die. This was repeated for each die to produce data
at four different shear rates. The total time taken for
the charging and injection process was kept as constant
as possible to minimise possible errors which might arise
from the polymer experiencing different thermal
histories.

3.2.3   Rheological Measurements

The rheological measurements were performed using a
number of capillary and orifice dies, the dimensions of
which are shown in table 3.1.

a.

Tapered
brass rod

Capillary
die

Bolster

b.

Metal disk

Orifice
die

Steel rod

Bolster
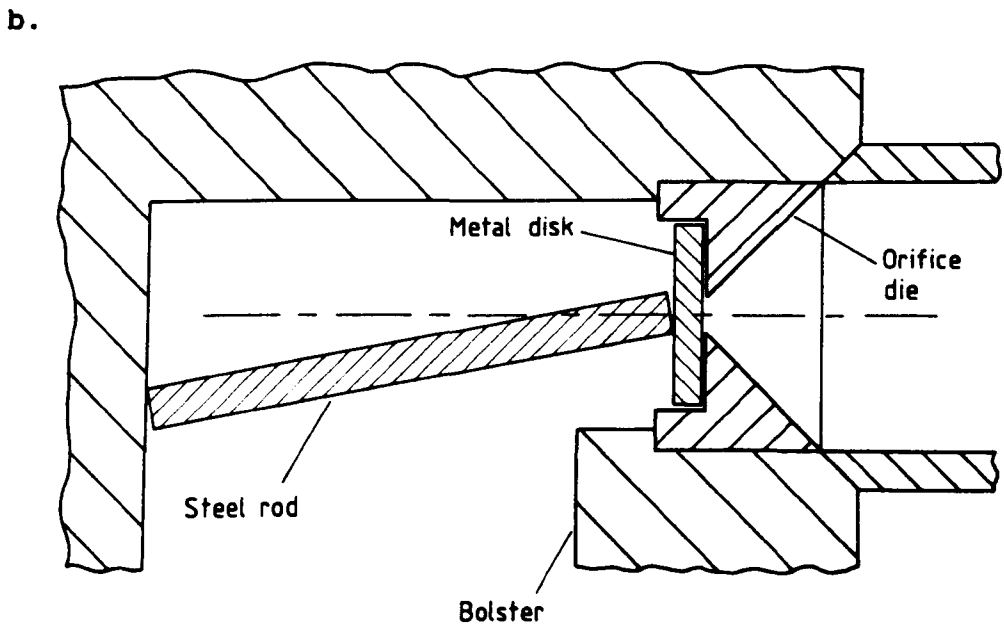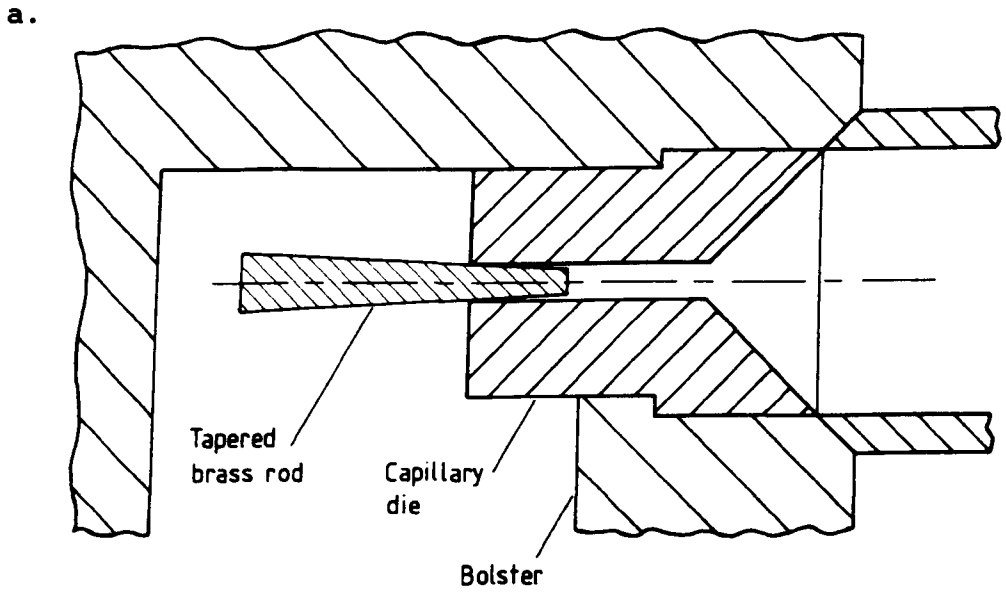
Figure 3.4. Methods of blocking the die exit during the
charging of the injection moulding machine.
a. Capillary die.
b. Orifice die.

	Laboratory rheometer		Injection moulding machine	
Capillary diameter (mm)	1	2	2	4
Capillary length (mm)	0 6.35 12.8 16	0 8 32 61	20 30	0 20 40 60 80
Capillary die semi angle (degrees)	90	90	45	45
Orifice die semi angles (degrees)	30 50 70 90	30 50 70 90		15 30 45 60 90
Shear rate (s^{-1}) min	110	14	6800	850
Shear rate (s^{-1}) max	12800	1600	48000	7400
Material and Temps.	SRP 1500GL30 at 340°C		SRP 1500GL30 at 340°C	
	SRP 1500G at 325, 330, 340, & 350°C			

Table 3.1. The dimensions of the capillary and orifice dies used in the rheological measurements, the shear rates covered by the respective dies and the grade of polymer plus the temperatures at which it was tested.

3.2.4   Treatment of Data

3.2.4.1   Rheological Model

For ease of reference the relevant rheological equations used in the Gibson model are given in tables 3.2 and 3.3. The shear and extensional viscosity were modelled using the four power law expressions in equations 3.1 - 4.

The various steps in the treatment of the data are shown schematically in figures 3.5a — f, and are described in detail below.

Many of the calculations involved in analysing the data were performed with the aid of computer programs. A program previously used by McClelland[110] and Corscadden[111] was modified and used in the calculation of the shear and extensional viscosity.

3.2.4.2   Primary Data

Examples of the outputs are shown in figures 3.6 and 3.7, for the laboratory rheometer and injection moulding machine respectively.

As can be seen in figure 3.6 the laboratory rheometer

Shear stress $= \tau = G\Gamma^m$	3.1
Shear viscosity $= \cap_s = G\Gamma^{m-1}$	3.2
Extensional stress $= \sigma = H\epsilon^n$	3.3
Extensional viscosity $= \cap_e = H\epsilon^{n-1}$	3.4
Apparent wall shear rate $= \Gamma_A = \dfrac{4Q}{\pi R_1^3} = \dfrac{4vR_o^2}{R_1^3}$	3.5
Wall shear stress $= \tau_w = \dfrac{1}{2} \cdot \dfrac{dP}{d(L/R_1)}$	3.6

Table 3.2. Rheological equations.

Total entry pressure $= P_{ent} = P_{As} + P_{Ae} + P_{Be}$	3.7
$$P_{As} = \frac{2G\sin^{3m}\alpha}{3m\alpha^{(1+3m)}} \left[\frac{1+3m}{4m}\right]^{m} \Gamma_{A}{}^{m} \left[1-\left[\frac{R_1}{R_o}\right]^{3m}\right]$$	3.8
Extensional strain rate $= \varepsilon = \frac{1}{4}\cdot\Gamma_{A}\cdot\sin\alpha(1+\cos\alpha)$	3.9
$$P_{Ae} = \frac{2H\varepsilon^{n}}{3n} \left[1-\left[\frac{R_1}{R_o}\right]^{3m}\right]$$	3.10
$$P_{Be} = \frac{H\Gamma_{A}{}^{n}}{4^{n}} \; \Phi(n,\alpha)$$	3.11
$$P_{Ae} + P_{Be} = H\varepsilon^{n} \left[\frac{2}{3n}\left[1-\left[\frac{R_1}{R_o}\right]^{3m}\right] + \frac{\Phi(n,\alpha)}{(\sin\alpha(1+\cos\alpha))^{n}}\right]$$	3.12
$$\sigma = H\varepsilon^{n} = \frac{P_{Ae} + P_{Be}}{\frac{2}{3n}\left[1-\left[\frac{R_1}{R_o}\right]^{3m}\right] + \frac{\Phi(n,\alpha)}{(\sin\alpha(1+\cos\alpha))^{n}}}$$	3.13

Region B

Region A

Region C
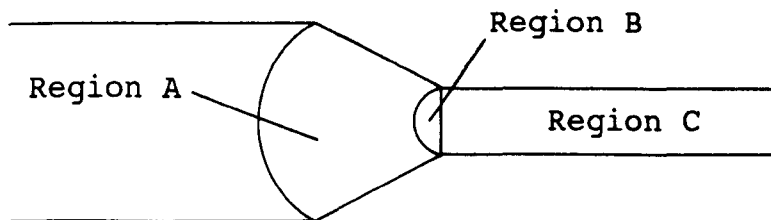
Table 3.3. Rheological equations used in the Gibson model.
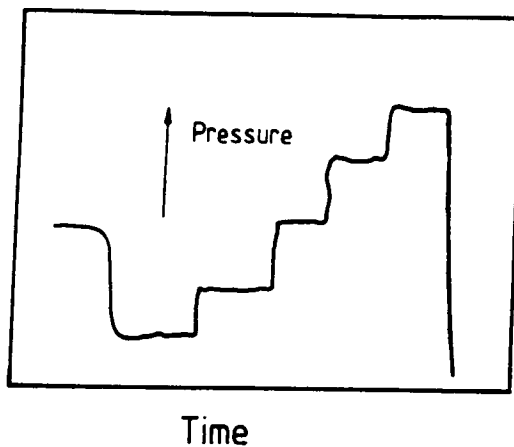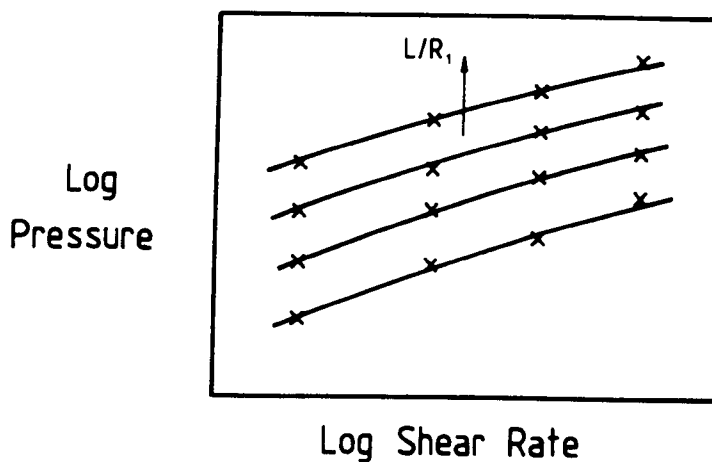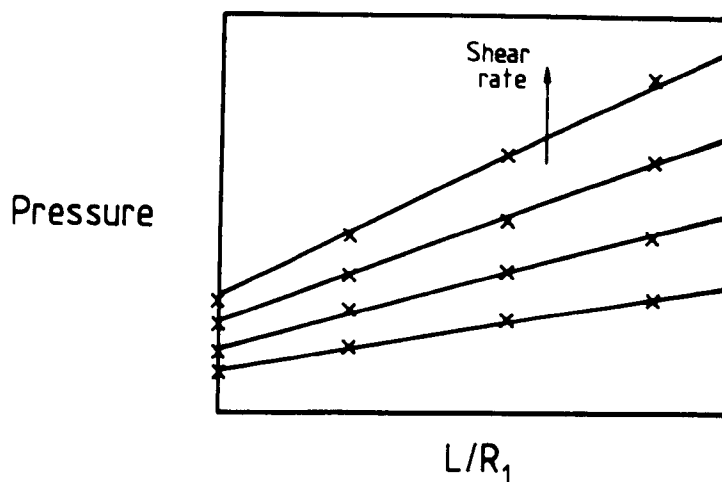
Figure 3.5. Schematic illustration of the various stages
involved in processing the rheological data.
a. Initial pressure vs. time trace obtained from the
   rheometer.
b. Log pressure vs. log shear rate, used to calculate the
   pressure at defined shear rates.
c. Bagley plot, pressure vs. L/R_1, at set shear rates.

d.
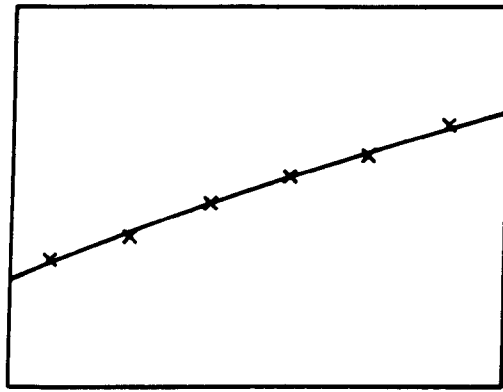
e.

f.
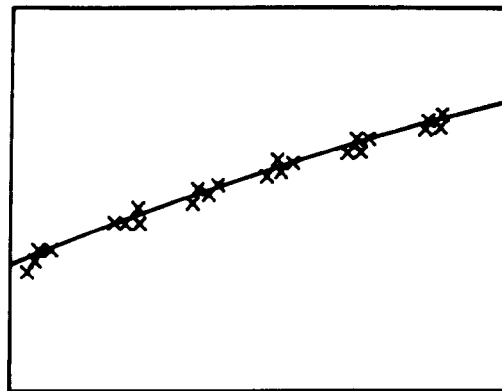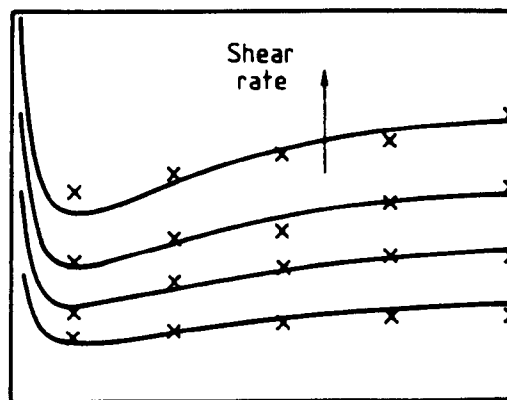
Figure 3.5. continued;
d. Log τ_w vs. log Γ, providing the power law constants
   for shear flow.
e. Log σ vs. log ϵ, providing the power law constants for
   extensional flow.
f. Comparison of the modelled and experimentally obtained
   entry pressure.
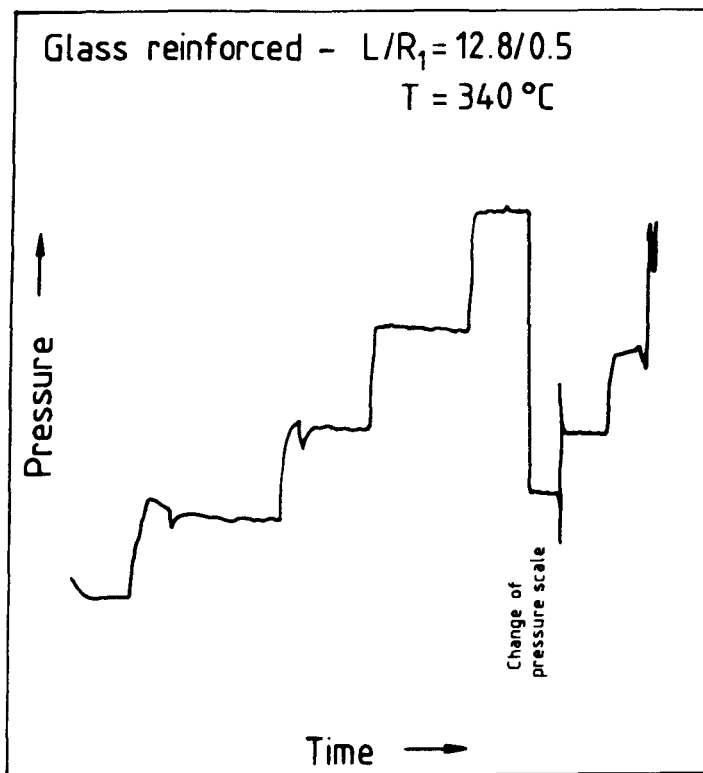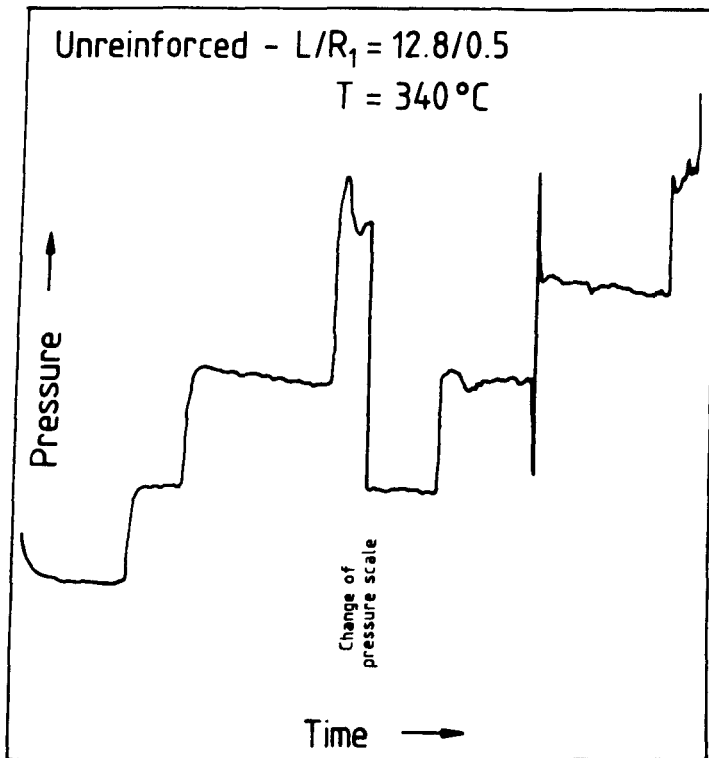
Figure 3.6. Initial pressure traces obtained for the unreinforced and reinforced polymer from the laboratory rheometer.
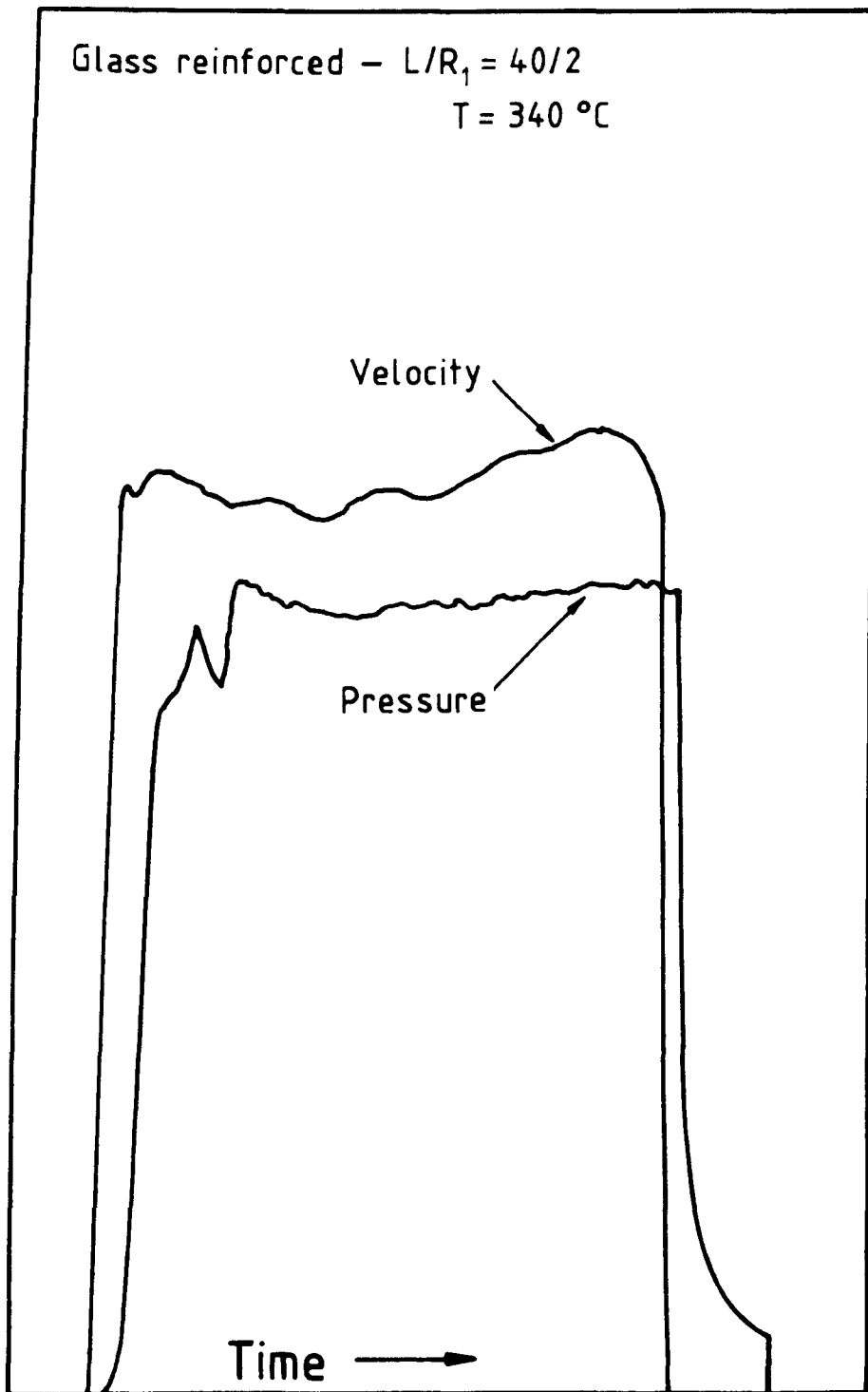
Figure 3.7. Initial pressure and velocity trace obtained from the instrumented injection moulding machine.

produced a single pressure trace, which increased with each increase in the downward velocity of the ram. Hence each plateau on the trace corresponded to a pressure at a known shear rate.

The output from the injection moulding machine, figure 3.7, shows two traces, one for the linear velocity of the screw, the other for the pressure produced at the shear rate associated with the velocity.

3.2.4.3 Pressure vs. Shear Rate Plots

The first step in processing the data was to convert the velocity of the ram and screw into a flow rate, and hence to an apparent shear rate using equation 3.5.

The initial data were plotted in the form of log pressure vs. log shear rate graphs, shown schematically in figure 3.5b. The experimental points were found to be slightly non-linear, and hence a quadratic curve was fitted. It should be noted that this total pressure consists of both the entry and capillary pressure drops. The former is determined primarily by extensional flow and the latter by shear flow, which are assumed to obey independent power laws, equations 3.2 and 3.4. These plots would only be straight lines if the power law indices were equal, and the equations held over a wide strain rate range.

3.2.4.4 Bagley Plots

From the pressure vs. shear rate plots the pressure at a number of specified shear rates, for the different L/R_1 ratios, was calculated. For the laboratory rheometer these apparent shear rates were 25, 50, 100, 250, 500, 1000, 2500, 5000, and 10000 s^{-1}. The 0.5mm capillary dies covered the six higher shear rates, while the 1.0mm capillary dies spanned the six lowest ones. The injection moulding machine covered apparent shear rates from 500 to 50000 s^{-1}, taken in similar steps to the laboratory rheometer.

Using the procedure proposed by Bagley[104] the pressure was plotted against the L/R_1 ratio for each shear rate, figure 3.5c. The Bagley plots were in all cases linear, within experimental error, and so could be fitted by straight lines. These plots enabled the entry pressure and capillary pressure drop to be separated, for the various shear rates, and from the gradient of the plot the value of the wall shear stress, τ_w, could be calculated using equation 3.6.

3.2.4.5 Shear Viscosity

Using the values of the wall shear stress obtained from the Bagley plots, a graph of log τ_w vs. log shear rate

was plotted, figure 3.5d.

Fitting a straight line to these points yielded the
constants G and m, which describe the shear flow.
However, the points were found to be slightly non-linear,
and so a quadratic curve was fitted. By constructing a
tangent to the curve at a defined shear rate, the
constants at that shear rate could be calculated. Using
an iterative process, the value of m was used in the
Rabinowitsch correction[60] to calculate the true shear
rate to produce a final plot of log wall shear stress vs.
log true shear rate.

3.2.4.6 Extensional Viscosity

Once the shear flow constants had been evaluated, the
shear component of the entry pressure, P_{AB}, was
calculated from equation 3.8, for each shear rate point.
This was then subtracted from the total entry pressure to
leave the extensional component (P_{Ae} + P_{Be}).

The extensional component of the entry pressure was used
in equation 3.13 to calculate the maximum extending
stress, σ, and plotted against the strain rate on a log-
log scale. The constants H and n were found from the
intercept and gradient respectively. The nature of the
equation meant that an iterative process was required to

find H and n, starting with a trial value of n. For a
linear plot, three or four iterations were sufficient to
produce convergent values.

As for the shear flow data, log σ vs. log ε plots were
generally found to be slightly non-linear, and so a
quadratic curve was again fitted. Starting with a trial
value of n an iterative process of quadratic curve
fitting was performed. From each data point, new values
of n were calculated for each strain rate to produce a
better estimate of the extending stress. The points were
found to converge on constant values, to four significant
figures, after approximately ten iterations.

3.2.4.7 Comparison of the Modelled and Experimental Entry Pressures

To demonstrate the applicability of the model the four
power law constants G, H, m, and n were used to predict
the entry pressure for a range of die angles and shear
rates. This was done by substituting values into
equations 3.8, 3.10, and 3.11 which when added together
gave the total entry pressure, equation 3.7. These
predicted values were then compared with experimentally
obtained points.

3.3   Mechanical Properties

3.3.1   Injection Moulding of Material

Prior to injection moulding the polymer was dried in an air circulating oven at 120°C overnight and then at 150°C for an hour just before the actual moulding. The machine parameters used during the moulding are shown below;

Injection speed		45 mm/s
Injection pressure		50 bar
1ᵗᵗ hold pressure		25 bar 5 sec
Back pressure	UF	3 bar
	GF	0 bar
Cooling time		35 sec
Temperatures	rear	310 °C
	middle	320 °C
	front	330 °C
	nozzle	340 °C
	mould	40 °C
Screw speed	UF	110 rpm
	GF	180 rpm

These settings were used to mould two types of test component, a plaque with sections of varying thickness

and a plaque containing a seam weld line.

3.3.2 Preparation of Test Specimens

3.3.2.1 Stepped Plaque

The stepped plaque, shown in figure 3.8, was designed to produce a moulding which contained stepped sections of different thickness. A dam was incorporated into the moulding to eliminate problems from jetting and produce an even flow front. Each moulding cycle produced two plaques with three different sections per plaque. The sections produced were approximately 0.7, 2.0 and 3.0mm thick from one plaque and 1.5, 2.5 and 3.5mm thick from the other. From each of these sections four test specimens were produced, two for tensile testing, parallel and perpendicular to the flow direction, and two for DMTA, again parallel and perpendicular to the flow direction. The position and dimensions of the specimens are shown in figure 3.9.

The tensile samples were produced by clamping roughly cut rectangular sections between hardened metal templates and removing excess material with a rotary cutting tool. The DMTA samples were prepared by clamping the rough cut sections between rectangular templates and removing the
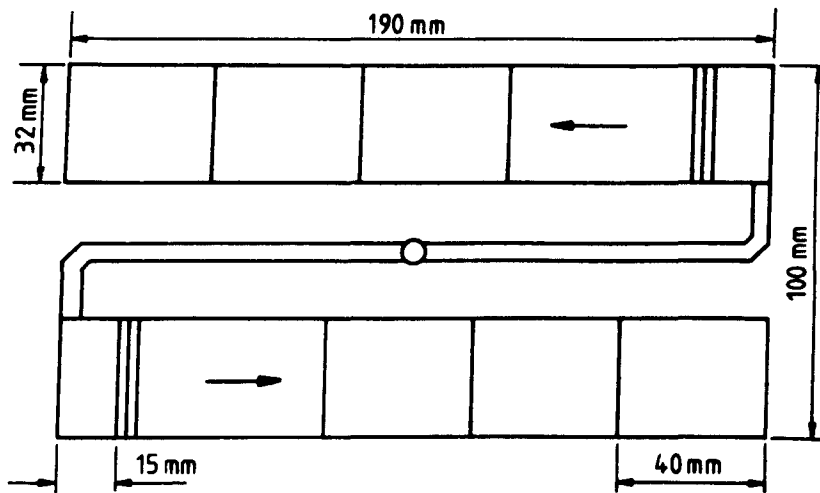
Figure 3.8. Plan and isometric view of the stepped plaque, indicating the major dimensions.
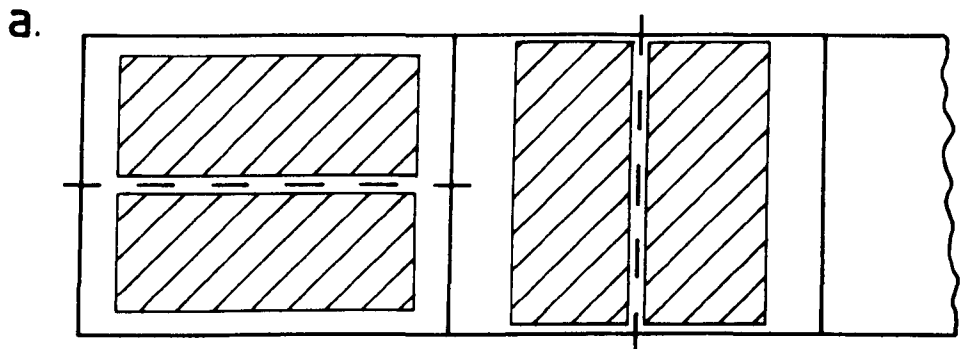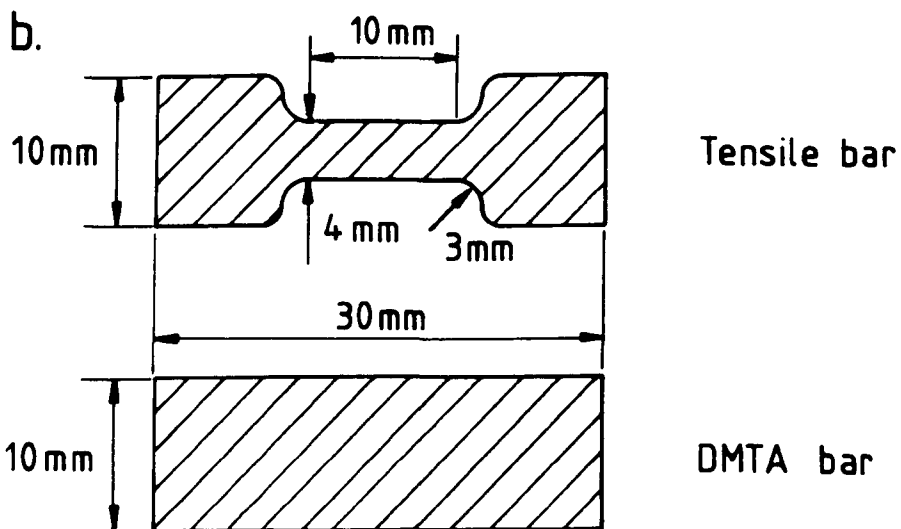
Figure 3.9. Stepped plaque,
a. Areas of the plaque used for the preparation of
   specimens, parallel and perpendicular to the major
   flow direction, which were to be used in mechanical
   testing.
b. Dimensions of the specimens used for tensile testing
   and dynamic mechanical and thermal analysis.

excess polymer on a linisher.

3.3.2.2 Weld Line Plaque

The weld line plaque, shown in figure 3.10, was used to produce a standard 4mm thick section with a seam weld running down the centre of the plaque. The weld line strength was examined by cutting tensile specimens, perpendicular to the flow, at specified distances along the weld line. The position and dimensions of the specimens are shown in figure 3.11. These were produced using the same technique as was employed to produce the tensile samples from the stepped plaque.

3.3.3 Mechanical Testing

3.3.3.1 Tensile Testing

The tensile tests were performed on an Instron machine, model 1185, using a 10KN load cell and a cross head speed of 1mm/min.

For the stepped plaque, ten samples for each thickness and grade of polymer were tested parallel and perpendicular to the flow direction. An average and
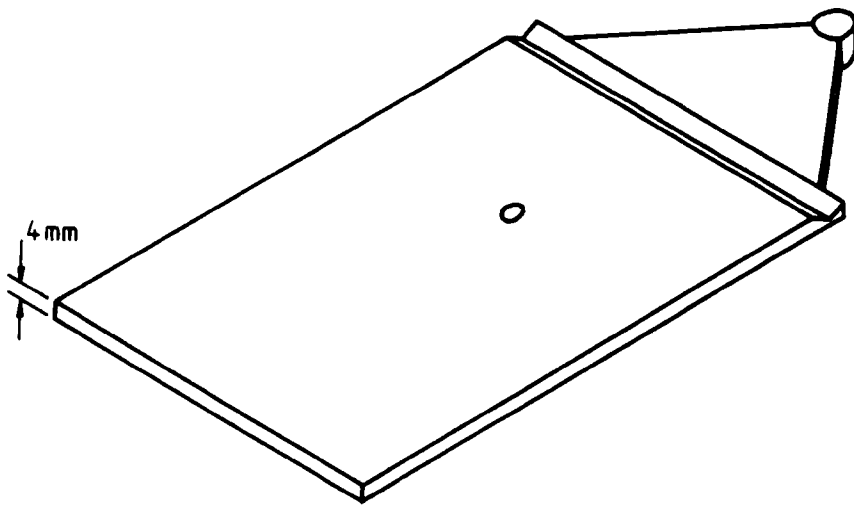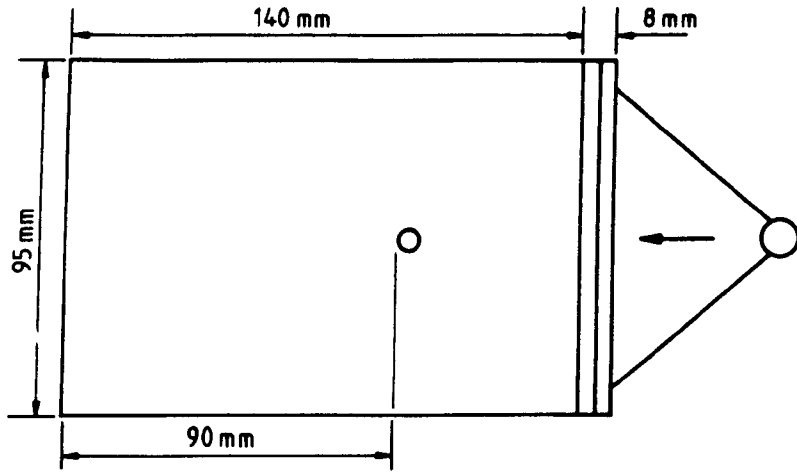
Figure 3.10. Plan and isometric view of the weld line plaque, indicating the major dimensions.

a.
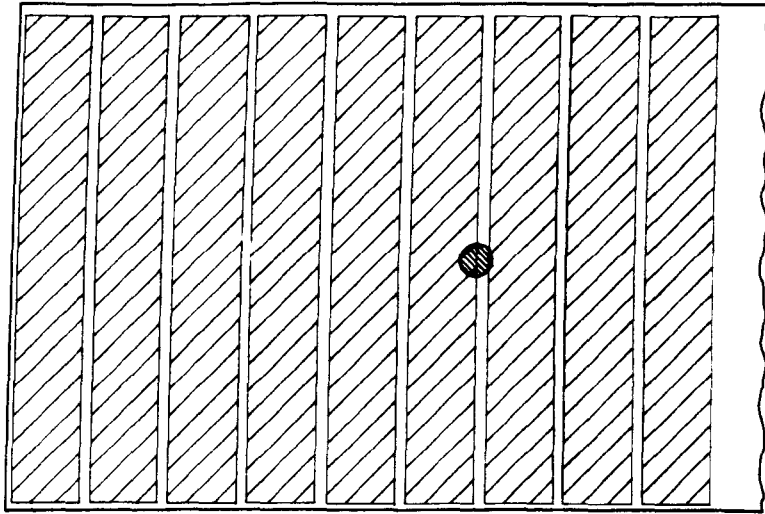
b.
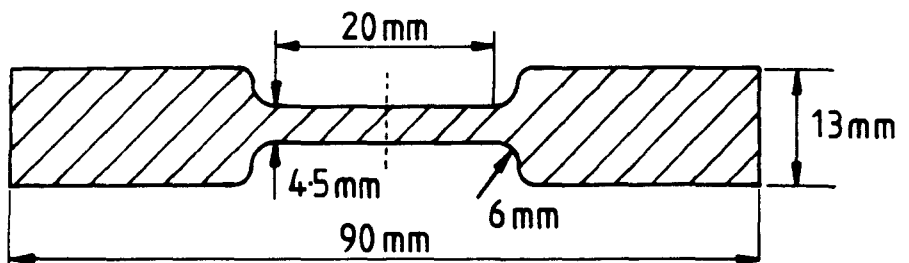
Figure 3.11. Weld line plaque,
a. Positions on the plaque from which the tensile samples
   were cut.
b. Dimensions of the tensile samples.

standard deviation of the tensile strength was calculated and plotted against section thickness.

For the weld line plaque, five samples were tested for each distance along the weld line for the filled and unfilled polymer. The tensile strength was calculated and an average taken. Due to the small number of specimens tested a t-test was performed to obtain 95% significance levels. The tensile strength was then plotted against distance.

3.3.3.2 Dynamic Mechanical and Thermal Analysis

The DMTA of samples from the stepped plaque was performed using a Polymer Laboratories Mark II Dynamic Mechanical Thermal Analyser. Sections were tested in single cantilever mode at a strain of x4, giving a nominal peak to peak displacement of 64μm, and a frequency of 10Hz. The temperature range was set from -100°C to 300°C, and a heating rate of 4°C per minute was employed. To prevent degradation a nitrogen bleed was used to surround the sample in an inert atmosphere. The results were obtained in graphical form, with plots of tanδ and storage modulus against temperature being produced.

3.4   Morphological Examination

3.4.1 Optical Microscopy

In order to examine the morphology of the polymer in
transmitted light, thin sections, less than 30μm, had to
be produced.

Initial attempts at microtoming sections of the LCP from
the mouldings proved to be unsuccessful, due to the
fibrous nature of the polymer. The knife of the
microtome, rather than slicing through the polymer,
caused the sample to split along the flow direction or
produce small chips which curled up and were unsuitable
for microscopic examination. Hence it was necessary to
adopt a process which involved grinding to produce
sections of the required dimensions. Figure 3.12a-h shows
schematically the different stages of this process.

A small sample of polymer, with an area of approximately
10mm², was sectioned from one of the injection moulded
plaques, making careful note of the flow direction. This
section was embedded in Epofix cold mounting resin, a
clear epoxy resin, with the surface to be examined facing
downwards. The resin and hardener were mixed as per the
manufacturers instructions and placed under vacuum for
several minutes to remove entrapped air. The resin was

a.

LCP section

b.

resin

mould

c.

finely ground
surface

d. force

resin

glass
slide

e.

coarse
grinding

f.

medium
grinding

g.

fine grinding

h.

cover
slip

immersion
oil
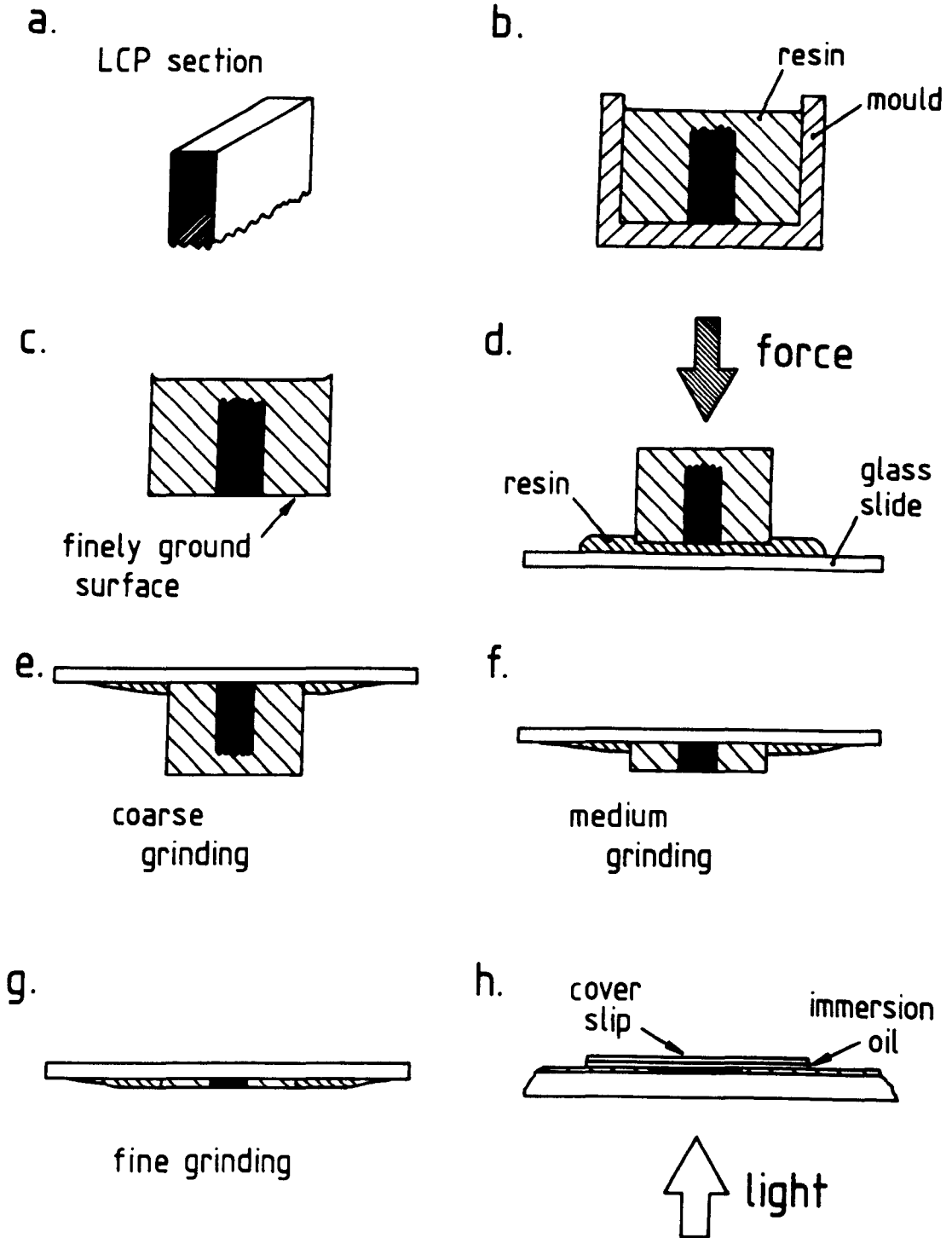
light

Figure 3.12. Schematic diagrams illustrating the sequence
of steps performed in the preparation of sections
suitable for examination by transmitted light microscopy.

119

then poured over the sample, which was held in a rubber mould, and left over night to solidify, figure 3.12b.

Once the resin had set, the sample was removed from the mould and the surface of the LCP to be examined was exposed by removing the excess resin, shown in figure 3.12c. This was achieved by grinding away the sample on successively finer and finer emery paper until a smooth surface had been prepared. This surface was examined under the microscope to ensure no deep scratches were present.

The ground surface was then secured to a glass slide using the Epofix resin, as illustrated in figure 3.12d. It was important at this stage to ensure that both the glass slide and the sample were clean and free from oil and grease. If this was not done, the resin would fail to make a strong bond between the sample and the glass. While the resin was setting, the sample was held firmly in position by use of a press, and left over night.

After the resin block had been securely fixed to the glass slide the upper part of the sample was ground away to produce a thin section. Initial grinding, figure 3.12e, was performed on coarse emery paper to rapidly remove excess material. As the section got thinner, a medium grade of paper was used, figure 3.12f, with the final stages of grinding were carried out with a fine

emery paper, shown in figure 3.12g. This ensured that the polymer was not ground away completely and also prevented any deep scratches being present in the finished section.

During the final stage of grinding it was possible to periodically examine the section under the microscope and thus determine whether or not the grinding process needed to be continued. When the section had been ground down to the required thickness, a drop of Fractoil immersion oil and a cover slip were placed over the sample, illustrated in figure 3.12h.

The sections produced by the above method were examined using two optical microscopes, a Leitz Metalloplan and a Reichert Zetopan, operating with plane polarised transmitted light. Representative photographs of the observed morphology were produced using standard photographic techniques.

3.4.2   Etched Specimens

The initial stages of sample preparation were the same as for the optical microscopy specimens, but after the first grinding process (figure 3.12c.), the samples were placed on an automatic polishing wheel. Using successively finer cloths, down to 1μm, a highly polished surface was obtained. The samples were examined using reflected light

microscopy to ensure no scratches remained after
polishing.

The samples were then etched by placing them in
concentrated sulphuric acid for 20 minutes. After
etching, the samples were carefully washed in distilled
water and then ultrasonically cleaned in acetone.

After cleaning, the etched samples were glued on to
aluminium stubs and gold coated, using an Edwards S150
sputter coater. The samples were coated for approximately
20 minutes, using a coating time of 2 seconds with a 20
second interval. A short coating time combined with a
long interval was used to prevent damage to the polymer.
The coated samples were subsequently examined by scanning
electron microscopy, using a Philips 501 SEM, at an
operating voltage of 30KV.

3.4.3 Fracture Surfaces

Samples from the stepped plaque which had been tensile
tested, as described in section 3.3.3.1, were retained
for the examination of fracture surfaces.

After the samples had been broken in tension, a fracture
surface was examined for each of the different sample
configurations. These were fracture surfaces from

specimens cut parallel and perpendicular to the flow
direction for the filled and unfilled polymer, from each
of the different thicknesses of the moulding. The
fracture surfaces were carefully mounted on aluminium
stubs and gold coated, following the same procedure as
outlined above, after which they were examined by
scanning electron microscopy.

3.4.4 Wide Angle X-ray Diffraction

In order to look at the variation of molecular
orientation through the thickness of a moulding, thin
layers, of the unfilled polymer were prepared for use
with X-ray diffraction equipment. The samples were
produced from a section of the stepped plaque. By
measuring the thickness of the section a known amount of
material could be ground away from the top surface. This
was then fixed to a flat surface and the polymer ground
away from the bottom of the section until a sample of
approximately 0.2mm had been produced. Five sections were
produced which covered areas from the surface to the core
of the moulding.

The X-rays were produced using a copper target with a
voltage of 35kV and current of 25mA producing Cu-Kα
radiation with a wavelength of 1.54Å. The position of the
polymer and the film, with respect to the X-ray beam, is

shown in figure 3.13. The film was placed 47.82mm from the polymer specimen and exposed for nine hours, after which it was processed in the conventional manner.

3.4.4.1 Crystalline Orientation

The degree of crystalline orientation may be evaluated by the well known method of calculating the mean-square cosine[115],

$$<\cos^2\Phi> = \frac{\int_0^{\frac{1}{2}\pi} I(\Phi) \sin\Phi \cos^2\Phi \, d\Phi}{\int_0^{\frac{1}{2}\pi} I(\Phi) \sin\Phi \, d\Phi} \qquad 3.14$$

where $I(\Phi)$ is the intensity at the angle Φ.

In the present work no diffractometry measurments were made. However, a quantitative, if approximate, means of describing the amount of crystalline orientation was felt to be desirable. This was achieved by measuring the arc position on the radiographs using a protractor and making the approximate assumption that the intensity was constant over the arc length. This is shown schematically in figure 3.14.

By assuming a constant intensity out to an angle ß, and zero beyond this angle, equation 3.14 may be rewritten

a.

Meridian

Major flow
direction

Equator

X-RAYS   POLYMER

FILM

b.

l

X-rays

2θ
2θ

r
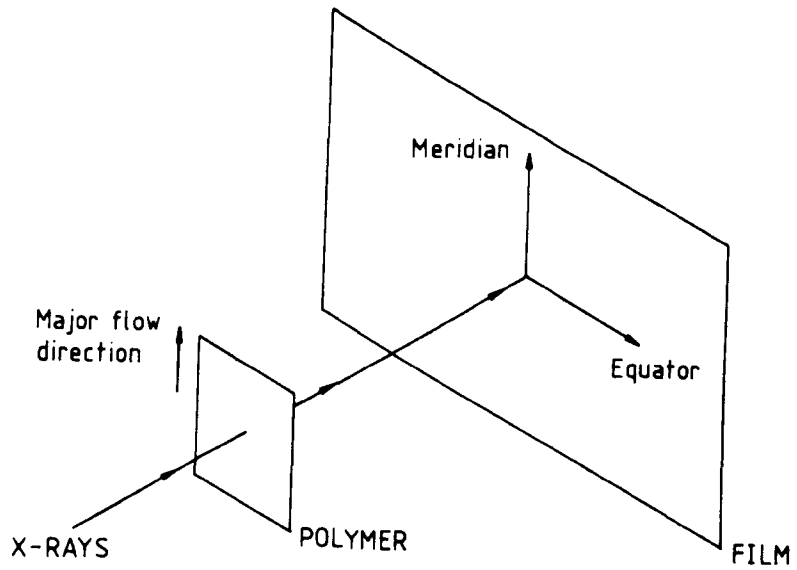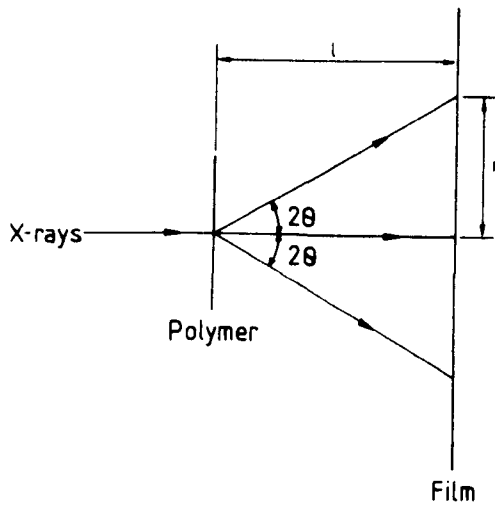
Polymer

Film

Figure 3.13. Schematic diagrams of the relative positions
of the polymer sample and film with respect to each other
and the X-ray beam.
a. Isometric view.
b. Side view.

a.
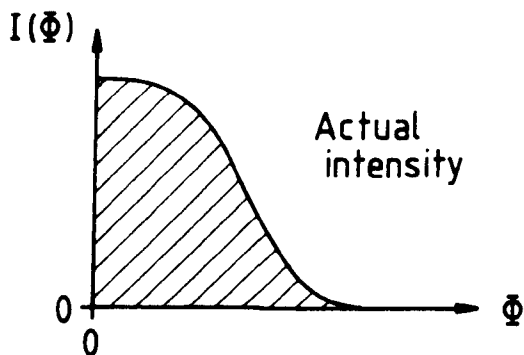
b.
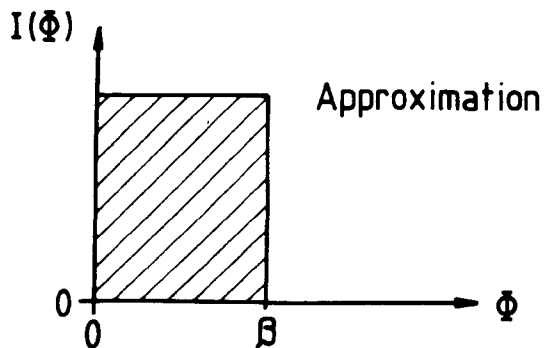
Figure 3.14. Schematic representation of the variation in
intensity distribution, I(Φ), with angle, Φ.
a. Actual intensity.
b. Approximation made to facilitate the calculation of an
orientation function.

as,

$$\langle \cos^2 \Phi \rangle = \frac{\int_0^\beta \sin\Phi \, \cos^2\Phi \, d\Phi}{\int_0^\beta \sin\Phi \, d\Phi} \qquad\qquad 3.15$$

The value of $\langle \cos^2\Phi \rangle$ can then be substituted into Hermans orientation function, $f_H = \frac{1}{2}(3\langle \cos^2\Phi \rangle - 1)$, to give the degree of orientation. For uniaxial orientation f_H equals unity, zero for random orientation, and $-\frac{1}{2}$ for transverse orientation.

Chapter 4

Results

4.1   Rheology

4.1.1 Pressure vs. Shear Rate

An example of the initial pressure vs. shear rate plots
obtained from the laboratory rheometer opperated at ICI
Wilton, is given in figure 4.1. This shows the plots for
the unreinforced polymer from the laboratory rheometer
for a die diameter of 2.0mm.

This is a typical example of the plots obtained and
clearly shows the almost linear relationship between the
log of the pressure and the log of the shear rate, within
the shear rate covered. A quadratic curve was fitted to
such data and the pressure at specified shear rates
evaluated, as described in section 3.2.4.4.

4.1.2 Bagley Plots

Figure 4.2 shows an example of a Bagley plot obtained
from the laboratory rheometer with a 1.0mm diameter die
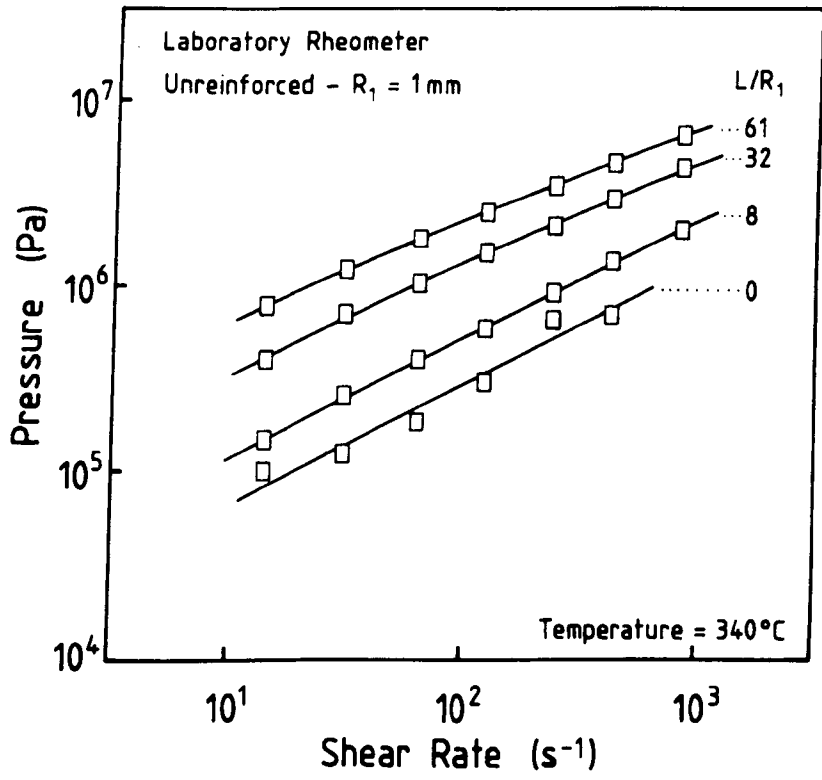
Figure 4.1. Log pressure vs. Log shear rate plot for the unreinforced polymer, using the laboratory rheometer with a capillary diameter of 2mm, at 340°C.
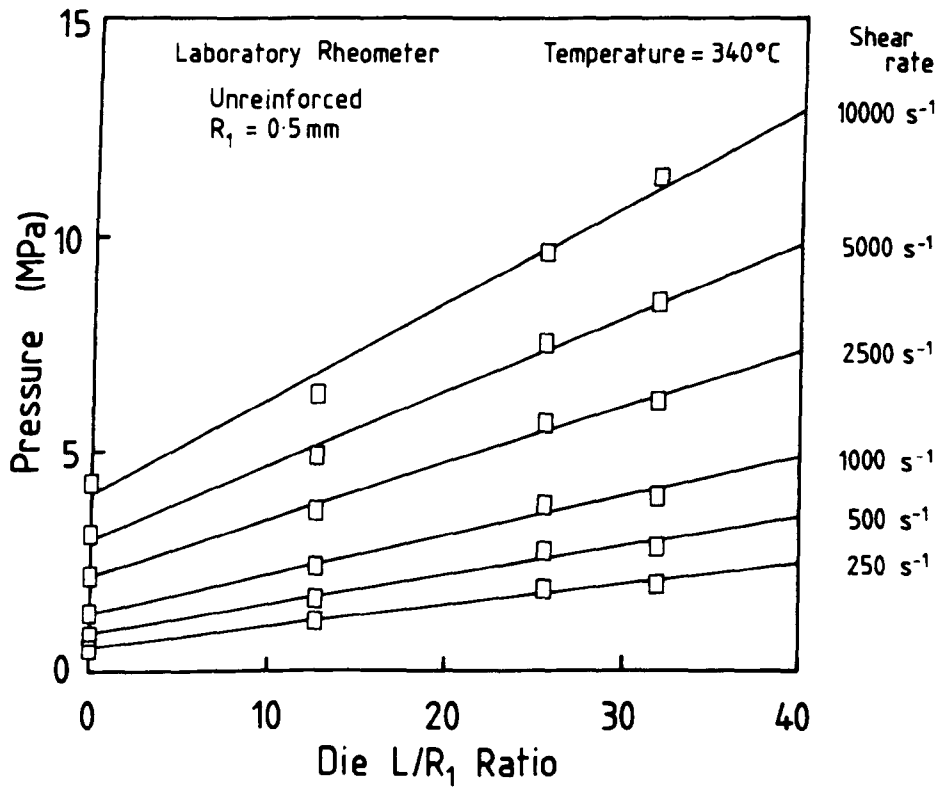
Figure 4.2. Bagley plot, pressure vs. L/R_1, for the unreinforced polymer, using the laboratory rheometer with a capillary diameter of 1mm, at 340°C.

and the unreinforced polymer at a temperature of 340°C.
The plot covers the highest shear rates produced by the
laboratory rheometer and indicates a linear relationship
between the pressure and aspect ratio of the die. Bagley
plots of this nature were found to occur for the other
test geometries and the reinforced polymer.

4.1.3   Temperature Dependence

In evaluating the temperature dependence of the polymer,
the unreinforced version was tested using a laboratory
rheometer at four temperatures.

The procedures described in section 3.2.4 were performed
on the data to produce the power law constants, which
were then used to calculate the shear and extensional
viscosities at various shear and strain rates.

4.1.3.1   Shear viscosity

The shear viscosity at shear rates of 10, 100, 1000, and
10000 s^{-1} was evaluated and plotted against temperature,
and is shown in figure 4.3. Over the temperature range
examined, from 325°C to 350°C, the shear viscosity
follows the same general pattern for each of the four
shear rates. A large initial drop in the viscosity
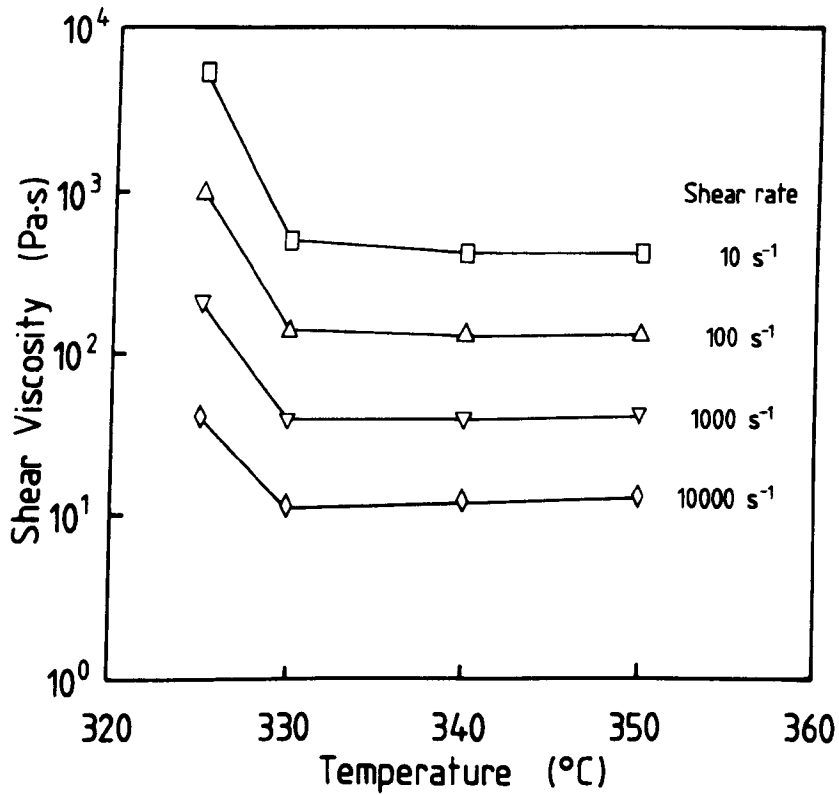
131

Figure 4.3. Shear viscosity vs. temperature, for the unreinforced polymer, using laboratory rheometer. Calculated at shear rates of 10, 100, 1000 and 10000s^{-1}.

between 325°C and 330°C, followed by a region of almost constant viscosity.

4.1.3.2 Extensional viscosity

Figure 4.4 shows the graph of extensional viscosity vs. temperature. This again covers the temperature range of 325°C to 350°C, with the viscosity being evaluated at strain rates of 1, 10, 100 and $1000s^{-1}$. At the lower strain rates the extensional viscosity shows a minimum value at approximately 340°C. As the strain rate is increased the temperature dependence becomes less pronounced, finishing with a region of almost constant viscosity between 330°C and 350°C at the highest strain rate of $1000s^{-1}$.

4.1.4 Shear Flow

4.1.4.1 Laboratory rheometer

The results from the laboratory rheometer for the glass reinforced and unreinforced polymer are shown in figure 4.5, in the form of log τ_w vs. log Γ.

As can be seen from this plot, the points produced by
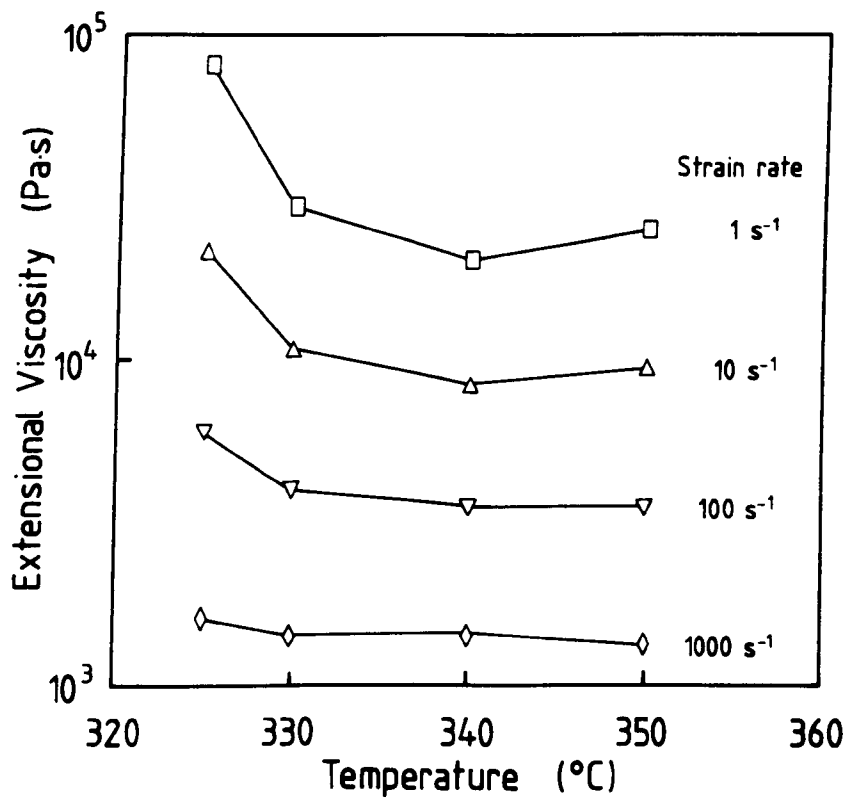
Figure 4.4. Extensional viscosity vs. temperature, for the unreinforced polymer, using laboratory rheometer. Calculated at strain rates of 1, 10, 100 and 1000s^{-1}.

Figure 4.5. Log τ_w vs. Log Γ, for the glass reinforced and unreinforced polymer, from the laboratory rheometer at 340°C.

using 1mm and 2mm diameter dies are in close agreement, and there is little difficulty in fitting a smooth curve. The wall shear stress produced by the reinforced polymer is consistantly greater than that produced by the unreinforced polymer over the shear rate covered.

Although the relationship between Log τ_w and Log Γ could be described approximately by a straight line, it is clear that there is a degree of non-linearity. For this reason a quadratic curve was fitted to the points. By finding the tangent to this curve it was possible to calculate the power law constants G and m at particular shear rates.

4.1.4.2 Injection moulding machine

The shear flow of the glass reinforced polymer through the injection moulding machine and the laboratory rheometer are compared in figure 4.6.

The points produced by the 2mm and 4mm diameter dies used with the injection moulding machine show a relatively large ammount of experimental scatter in comparison with the laboratory rheometer. However, using a least squares fit method a quadratic curve was forced through the points. Again the constants were found from the tangent to the curve.

Figure 4.6. Log τ_w vs. Log Γ, comparing the results for the glass reinforced polymer using the laboratory rheometer and the injection moulding machine, at 340°C.

137

The shear flow constants and the viscosity obtained for
the unreinforced and the reinforced polymer, from both
the laboratory rheometer and the injection moulding
machine, are presented in table 4.1 for three different
shear rates.

4.1.5 Extensional Flow

4.1.5.1 Curve fitting

Figure 4.7 shows the effect on the extensional stress of
fitting a linear and a quadratic curve to the data
points. The initial linear plot, produced by assuming a
straight forward power law relationship, indicates a
degree of curvature, particularly at the higher strain
rates. By fitting a quadratic curve to these points, and
calculating H and n from the tangent to the curve, new
values for the extensional stress were found. After
repeating this process, approximately ten times, the
quadratic curve shown in figure 4.7 was produced.

4.1.5.2 Laboratory rheometer

The extensional stress is plotted against the strain rate
on a log-log plot in figure 4.8 for the reinforced and

Table 4.1. Shear flow constants, G and m, and the viscosity calculated at shear rates of 100, 1000, and 10000s^{-1}.

Apparatus	Material			Shear rate (s^{-1})		
				100	1000	10000
Laboratory rheometer	SRP 1500G Unreinforced	Constants	G	1491	2031	3145
			m	0.467	0.412	0.357
		Shear Viscosity (Pa.s)		128.0	34.9	8.39
Laboratory rheometer	SRP 1500GL30 Glass reinforced	Constants	G	2320	3603	6728
			m	0.480	0.402	0.323
		Shear Viscosity (Pa.s)		211.9	57.8	13.2
Injection moulding machine	SRP 1500GL30 Glass reinforced	Constants	G	—	1134	5708
			m	—	0.553	0.348
		Shear Viscosity (Pa.s)		—	51.6	14.1
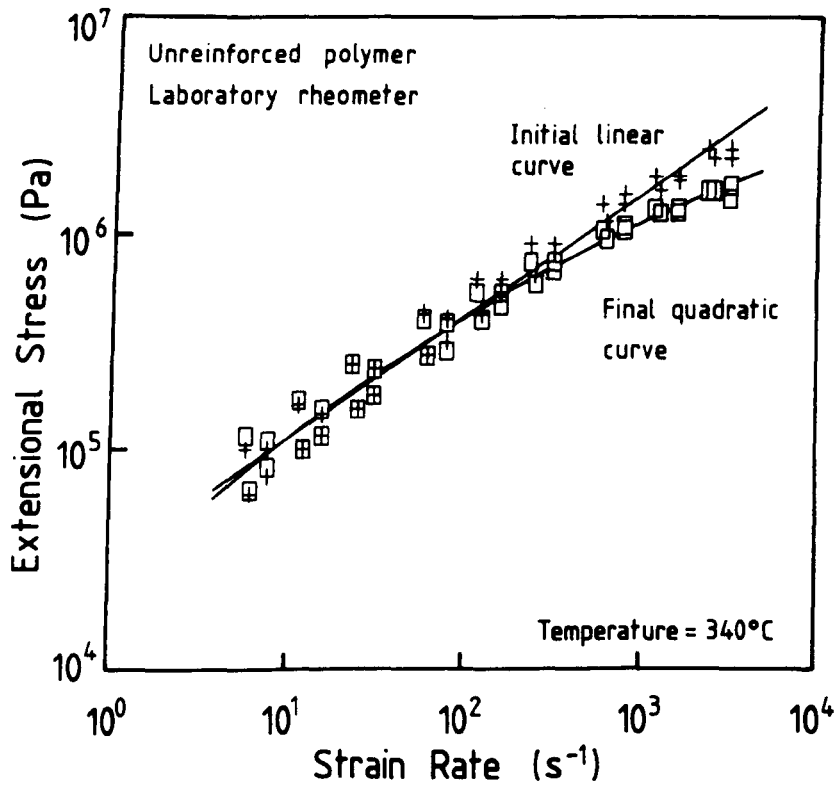
Figure 4.7. Log σ vs. Log ε, indicating the effect of fitting a straight line and a quadratic curve to the data obtained for the unreinforced polymer, using the laboratory rheometer at 340°C.
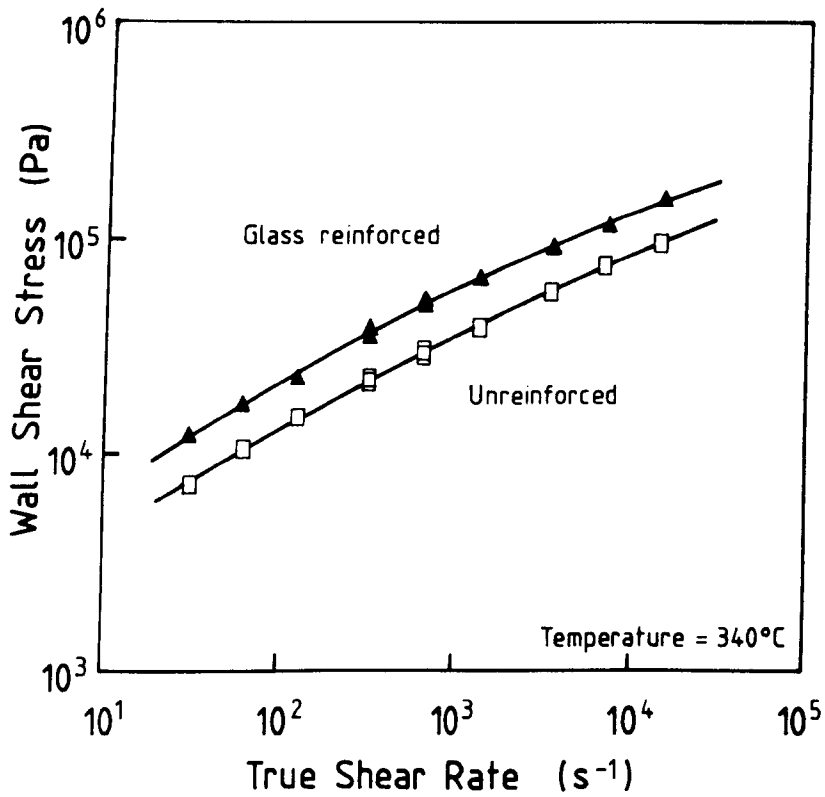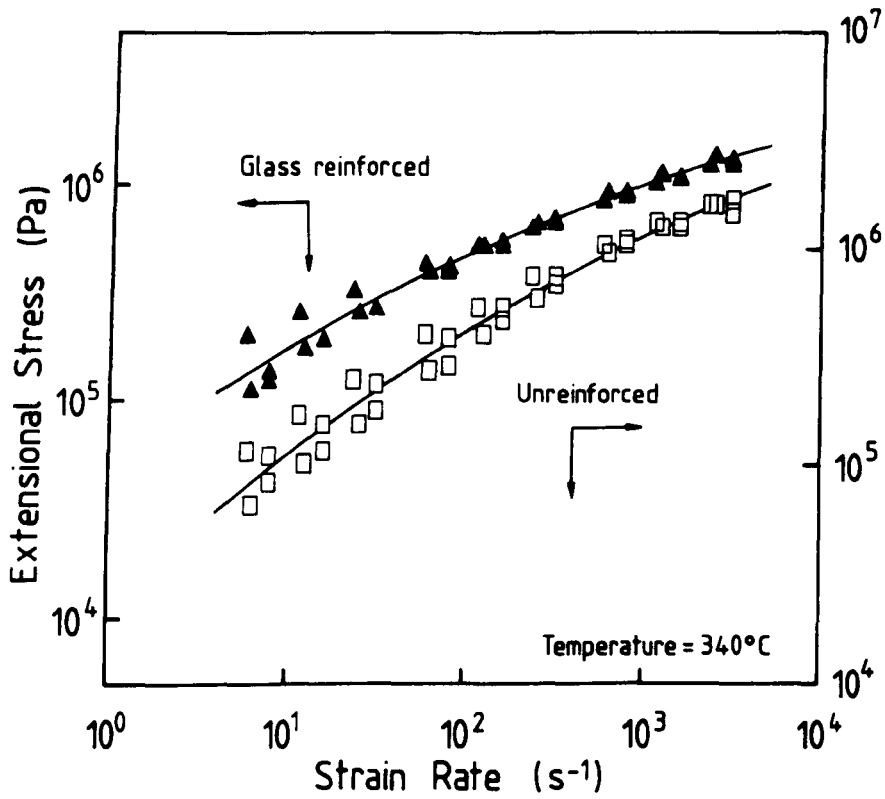
Figure 4.8. Log σ vs. Log ε, for the glass reinforced and unreinforced polymer, from the laboratory rheometer at 340°C.

unreinforced polymer.

For clarity the two curves have been shifted on the
stress scale. This was necessary because at the higher
strain rates the data points overlap. At the lower strain
rates the glass reinforced polymer produces a larger
extensional stress, with the unreinforced polymer giving
the greater values at the higher strain rates.

4.1.5.3   Injection moulding machine

The results from the laboratory rheometer and the
instrumented injection moulding machine are compared in
figure 4.9, for the reinforced polymer.

The extensional flow constants and viscosities for the
different test methods and polymer are given in table 4.2
for three strain rates.

4.1.6   Application of Theory

4.1.6.1   Modelling of the entry pressure

Figure 4.10 shows the predicted entry pressure for a
polymer at a shear rate of 1000 s^{-1} with power law
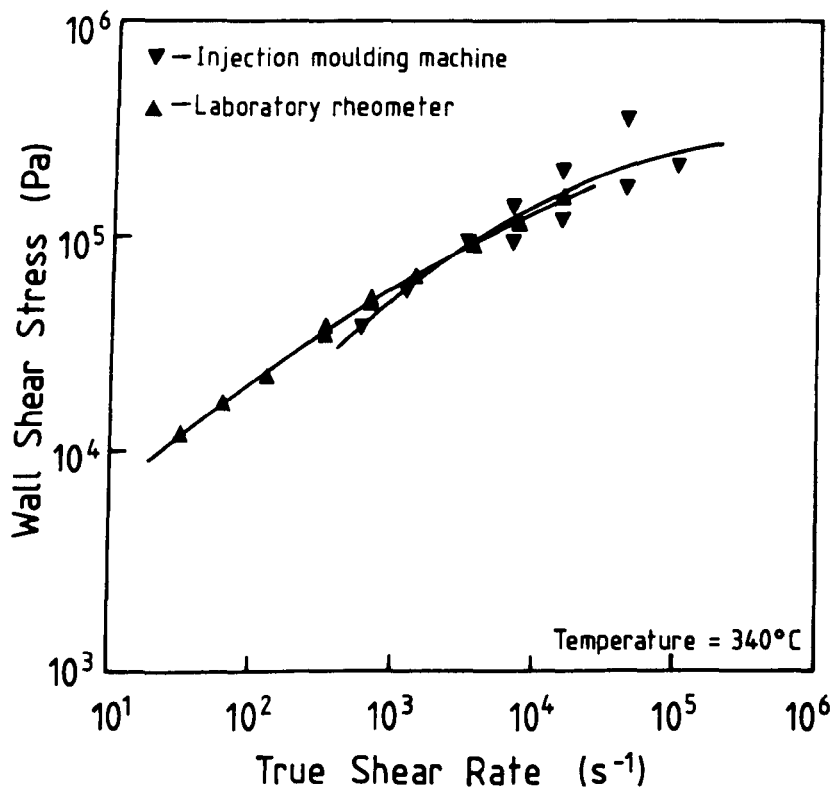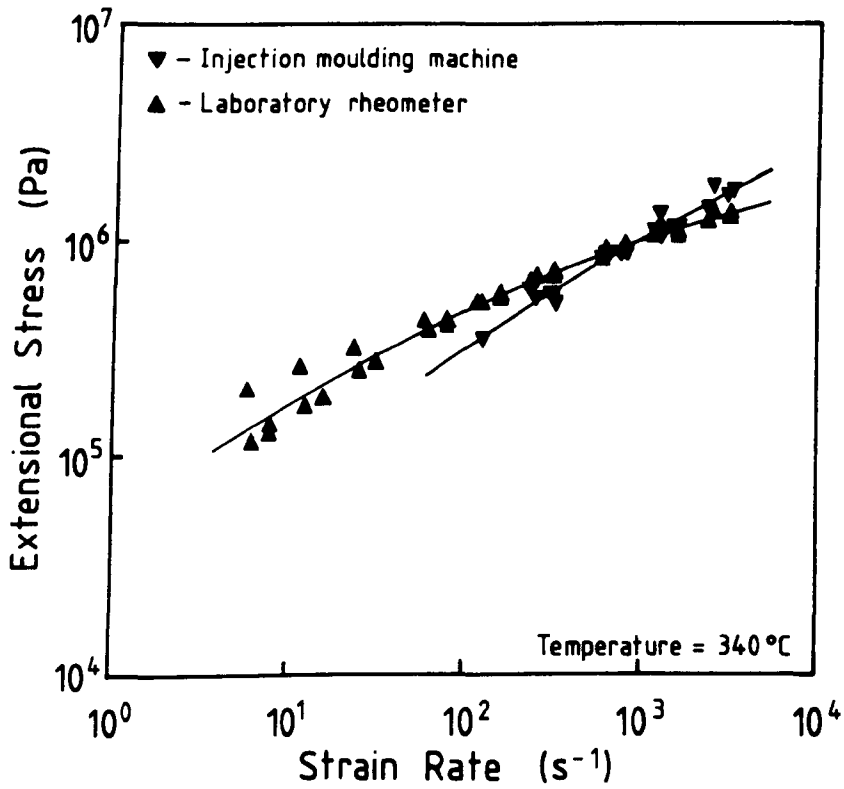
Figure 4.9. Log σ vs. Log ε, comparing the results for the glass reinforced polymer using the laboratory rheometer and the injection moulding machine, at 340°C.

Table 4.2. Extensional flow constants, H and n, and the viscosity calculated at strain rates of 10, 100, and $1000s^{-1}$.

Apparatus	Material			Strain rate (s^{-1})		
				10	100	1000
Laboratory rheometer	SRP 1500G Unreinforced	Constants	H	26500	40100	80000
			n	0.625	0.505	0.385
		Exten. Viscosity (Pa.s)		11170	4106	1145
Laboratory rheometer	SRP 1500GL30 Glass reinforced	Constants	H	57200	81100	145000
			n	0.481	0.380	0.279
		Exten. Viscosity (Pa.s)		17300	4660	995
Injection moulding machine	SRP 1500GL30 Glass reinforced	Constants	H	—	24300	41300
			n	—	0.555	0.463
		Exten. Viscosity (Pa.s)		—	3140	1010
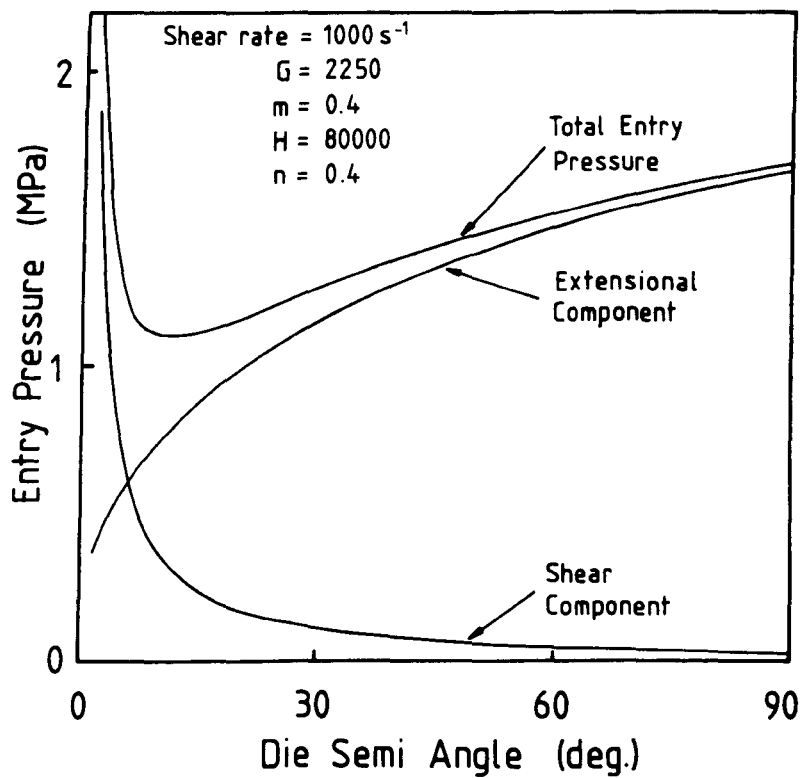
Figure 4.10. Predicted entry pressure as a function of
die angle, indicating the contributions made by shear and
extensional flow to the total entry pressure drop.

constants as set out below :—

Shear flow ... G = 2250
                m = 0.4

Extensional flow ... H = 80000
                     n = 0.4

The plot shows the contribution from the shear flow and
extensional flow, which are found by substituting the
four power law constants into the theoretical equations.
Addition of the shear and extensional flow components
produces the predicted total entry pressure. The
contribution made by the shear flow is seen to decrease
rapidly as the die angle increases, while the extensional
component increases with the increase in die angle.

4.1.6.2   Experimental entry pressures

To evaluate the applicability of the theory, the
predicted entry pressures were compared with
experimentally obtained values. These were found using
orifice dies with varing entry angles.

The results are shown in figures 4.11, 4.12 and 4.13 for
the laboratory rheometer with the unreinforced and
reinforced polymer and the injection moulding machine for
the reinforced polymer. The lines represent the predicted
pressures, while the points refer to the experimental
values.
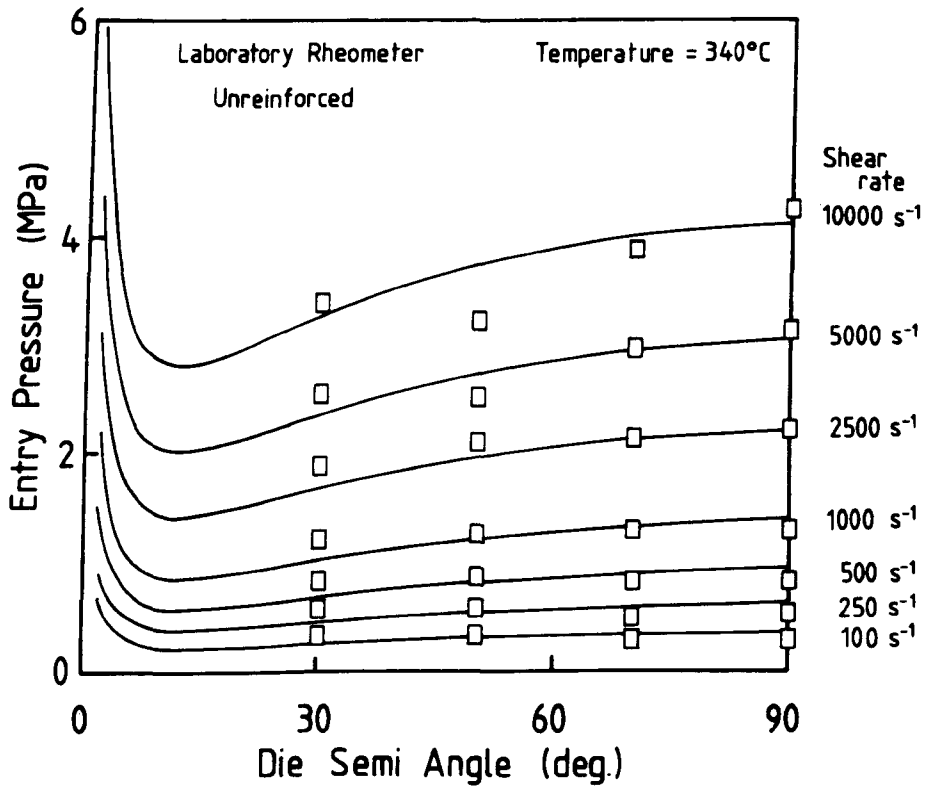
146

Figure 4.11. Entry pressure vs. die semi angle, for the
unreinforced polymer, using the laboratory rheometer,
comparing the predicted entry pressure with
experimentally obtained values.

Figure 4.12. Entry pressure vs. die semi angle, for the glass reinforced polymer, using the laboratory rheometer, comparing the predicted entry pressure with experimentally obtained values.

Figure 4.13. Entry pressure vs. die semi angle, for the glass reinforced polymer, using the injection moulding machine comparing the predicted entry pressure with experimentally obtained values.

4.2   Mechanical Properties

4.2.1   Tensile Properties

The tensile strength of the reinforced and unreinforced polymer, as a function of section thickness is shown in figure 4.14. A number of features are visible from this plot.

The highly anisotropic nature of the mouldings is clearly seen by the large difference between the tensile strengths parallel and perpendicular to the flow direction. For the unreinforced polymer, approximate average values of 150 and 30 MPa are found for the two orientations. Parallel to the major flow direction, the tensile strength shows a gradual decrease as the section thickness is increased, while the strength increases perpendicular to the flow. A 33% drop in tensile strength, approximately 50 MPa, is observed in going from the thinnest to the thickest section for the unreinforced polymer, parallel to the flow direction.

The addition of the glass fibres to the polymer has the effect of reducing the tensile strength parallel to the flow, and increases the strength perpendicular to the flow, thus reducing the overall mechanical anisotropy of the moulding. The differences in the section thickness
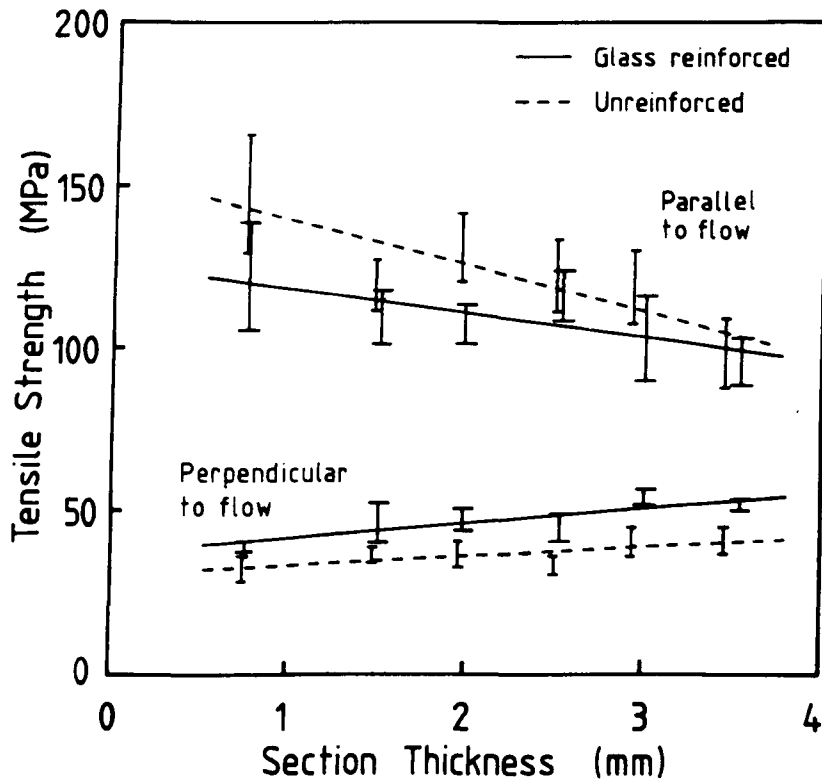
150

Figure 4.14. Tensile strength vs. section thickness for the reinforced and unreinforced grades of polymer, tested parallel and perpendicular to the major flow direction.

for the two grades of polymer shows the variation of
mould shrinkage with the addition of glass fibres. For
the unreinforced polymer, the through thickness shrinkage
is approximately 4.1%, which is reduced to 2.3% for the
glass filled grade.

4.2.2   Weld Line Strength

Figure 4.15 shows the tensile strength as a function of
distance along the weld line, and clearly indicates the
deleterious effect of a weld line on the strength of a
moulding. Ahead of the weld line, the strength shows a
slight improvement, indicating an increase in the amount
of transversally oriented material. Immediately after the
obstruction causing the weld line, the tensile strength
drops to less than 20% of its upstream value. As the
distance along the weld line increases, so the tensile
strength increases. For the glass reinforced polymer, a
maximum value of approximately 26 MPa is attained at
about 20mm from the obstruction, after which the strength
remains roughly constant. The unreinforced polymer shows
a sharp increase to the 20mm mark, followed by a gradual
improvement with distance, reaching a maximum of 34 MPa.
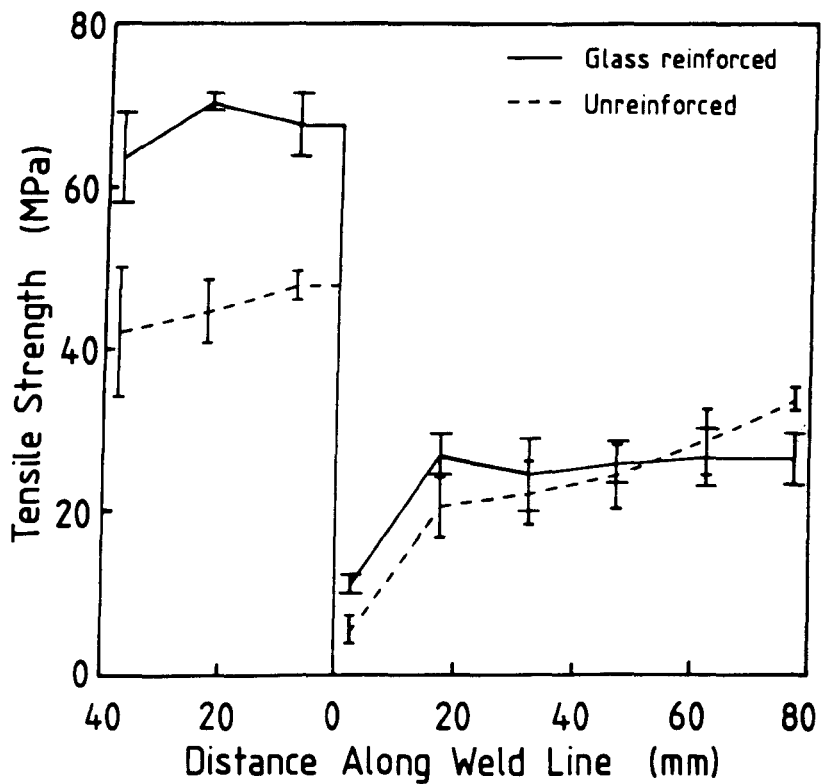
Figure 4.15. Tensile strength vs. distance along the weld line, indicating the weld line strength of the reinforced and unreinforced polymer.

4.2.3 Dynamic Mechanical and Thermal Analysis

Figures 4.16 - 20 show the results of the DMTA for various test configurations.

The temperature dependence of the mechanical loss factor, tan δ, and the storage modulus for the reinforced and unreinforced polymer is shown in figure 4.16. This is for the 0.7mm section parallel to the flow direction. The tan δ plots show three processes which, following custom, are labelled α, ß, and Γ, in order of decreasing temperature. The temperatures of these processes were found to be approximately 140˚C, 62˚C and -30˚C respectively, for samples tested parallel to the flow direction.

Figure 4.17 shows a plot of tan δ vs. temperature for the unreinforced polymer, parallel and perpendicular to the flow direction. For the samples tested perpendicular to the flow, the α, and Γ processes are found to occur at 138˚C and -32˚C, 2˚C lower than the values stated above. The temperature of the much smaller ß process remains unchanged. The large variation in the magnitude of tan δ, at the α transition, is associated with a much greater temperature dependence of the storage modulus for orientations perpendicular to the flow, compared with those parallel to the flow. This is illustrated by the plot of storage modulus against temperature shown in figure 4.18.
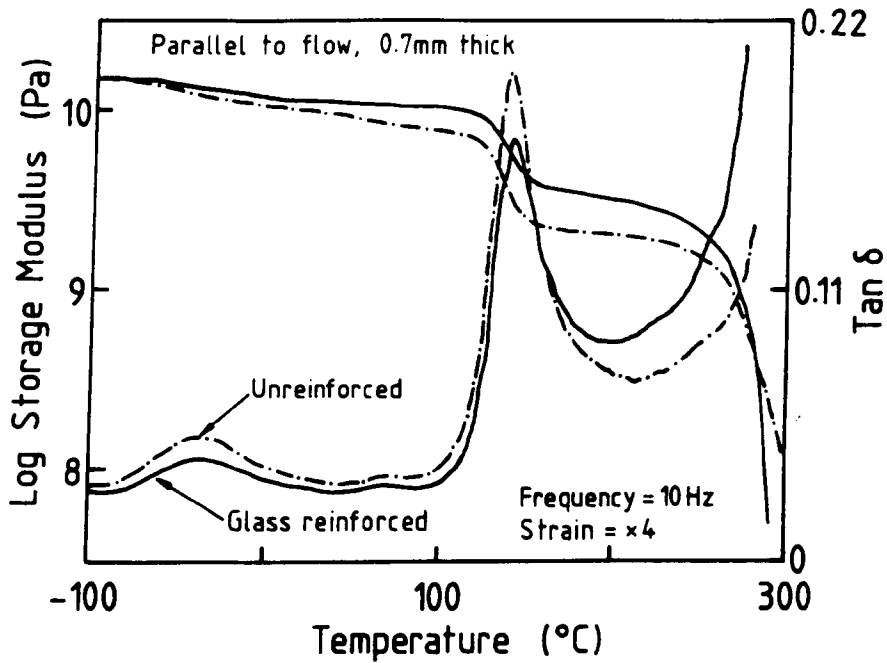
154

Figure 4.16. Plot of log storage modulus and tan δ
against temperature, obtained by DMTA. Results for a
0.7mm thick section, parallel to the flow direction for
the reinforced and unreinforced polymer.
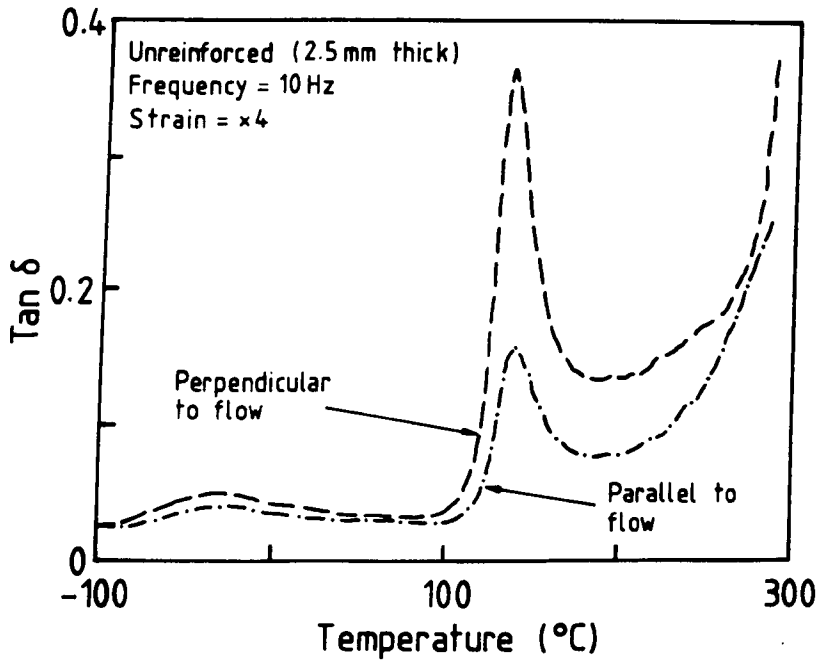
Figure 4.17. Tan δ vs. temperature, obtained by DMTA.
Results for a 2.5mm thick section, tested parallel and
perpendicular to the flow direction for the unreinforced
polymer.
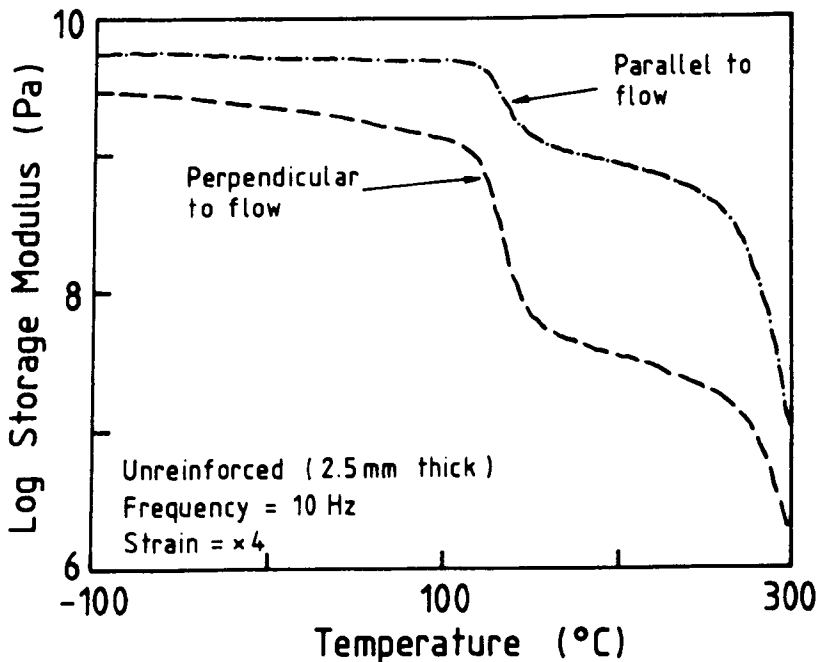
Figure 4.18. Log storage modulus vs. temperature,
obtained by DMTA. Results for a 2.5mm thick section,
tested parallel and perpendicular to the flow direction
for the unreinforced polymer.

156

The effect of section thickness is illustrated by figures 4.19 and 4.20, which show plots of the storage modulus and tan δ respectively. At temperatures below the α process, the modulus remains relatively constant, despite the two low temperature processes. The storage modulus is found to decrease with increasing section thickness, following the same pattern as was seen with the tensile strength. The value of tan δ decreases with increasing section thickness, but the transition temperatures remain unchanged.
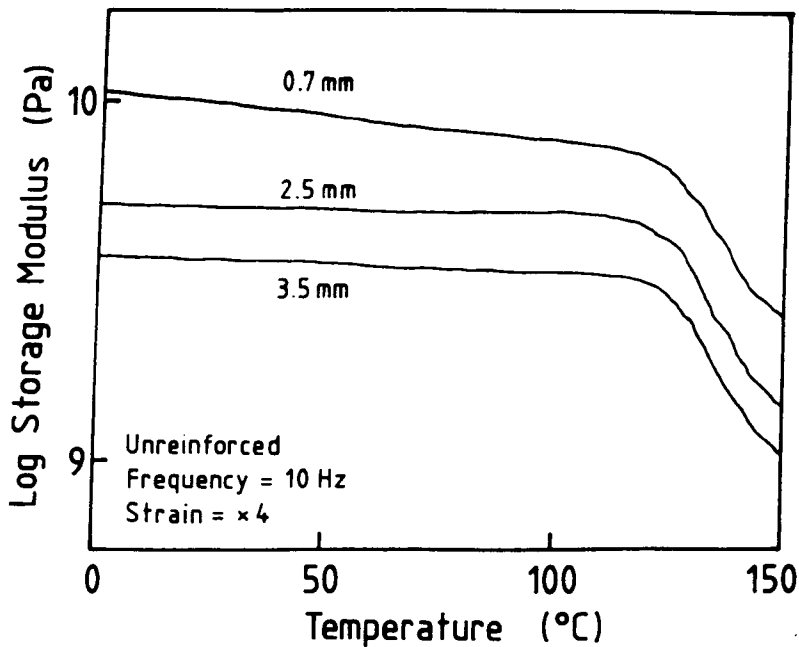
Figure 4.19. Log storage modulus vs. temperature, obtained by DMTA. Results for section thicknesses of 0.7, 2.5, and 3.5mm, tested parallel to the flow direction for the unreinforced polymer.
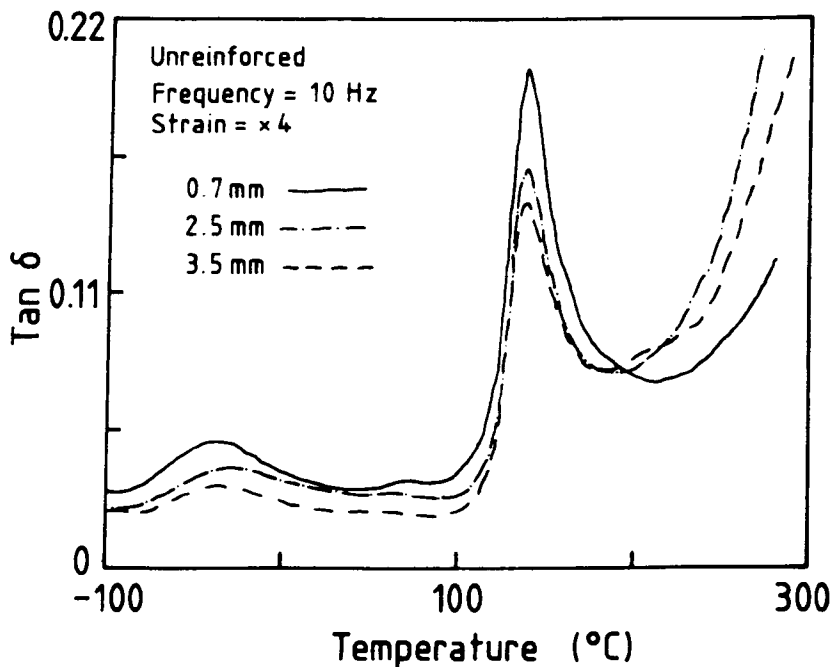
Figure 4.20. Tan δ vs. temperature, obtained by DMTA. Results for section thicknesses of 0.7, 2.5, and 3.5mm, tested parallel to the flow direction for the unreinforced polymer.

4.3   Morphology

4.3.1 Optical Microscopy

Examples of two, low magnification, optical micrographs
are shown in figures 4.21 and 4.22. These illustrate the
macroscopic layer structure of the 0.7mm and the 2.0mm
sections respectively. When examined in transmitted
light, all the sections revealed a light coloured skin
layer, followed by a dark layer, another light layer, and
a dark core. These colours are the reverse of those
mentioned in section 2.4.5.2, because the sections have
been viewed in transmitted, rather than reflected light.
Starting from the surface of the moulding, the layers
have been numbered I, II, III, and IV, as shown in figure
4.22.

By measuring the thickness of the individual layers it
was possible to examine the variation with section
thickness. Figure 4.23 shows the layer thickness as a
function of section thickness for each of the four
layers. Layer I, the skin layer, shows a gradual increase
with section thickness, going from approximately 0.20mm
to 0.56mm. The increase in layer II is more rapid, but
appears to reach a maximum value of about 0.95mm at
sections greater than 2.5mm. Layer III also shows a
constant thickness, of approximately 0.47mm, which is
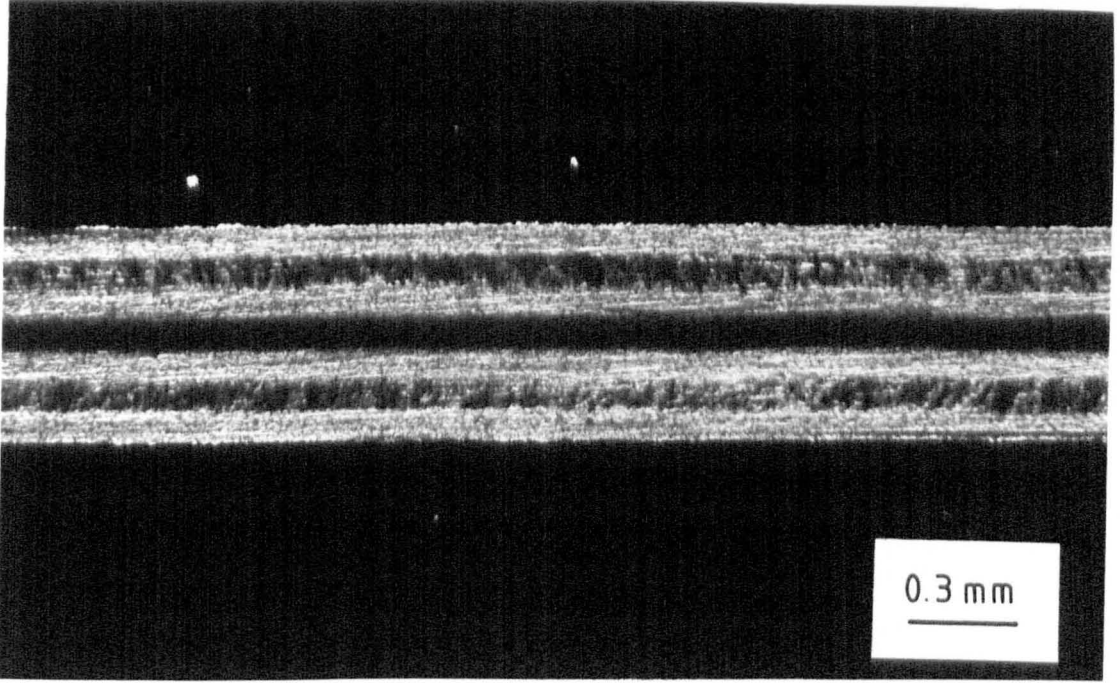
Figure 4.21. Optical transmitted light photograph of the unreinforced polymer, 0.7mm section, parallel to the flow direction. Magnification ≈ 47.
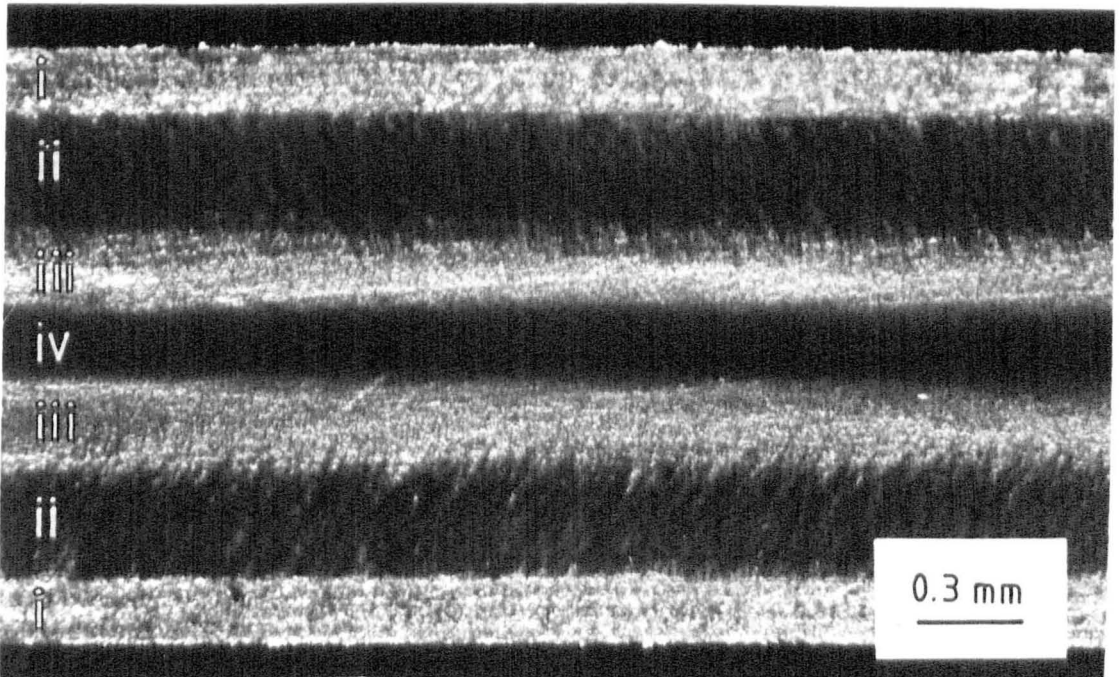
Figure 4.22. Optical transmitted light photograph of the unreinforced polymer, 2.0mm section, parallel to the flow direction, showing the nomenclature used to represent the layers. Magnification ≈ 47.

160
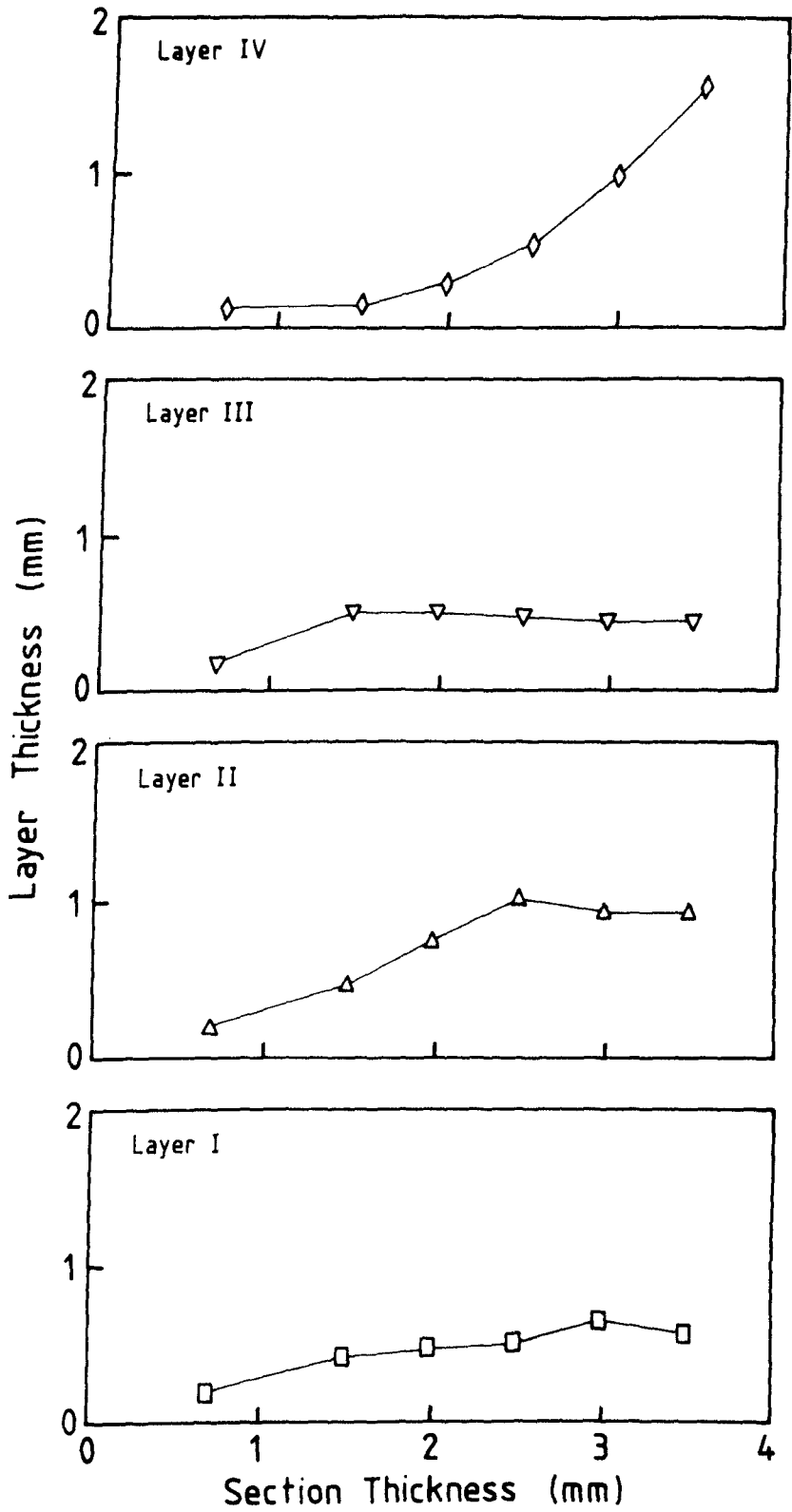
Figure 4.23. The thickness of the individual layers plotted against the section thickness.

reached at a section thickness of 1.5mm. The thickness of the core layer follows an almost exponential curve, reaching a maximum value of 1.55mm. The dimensions of the layers, as illustrated in figure 4.23, are expressed as a percentage of the total section thickness in figure 4.24. These plots indicate a reduction in the proportion of the moulding occupied by the skin layer, and layer III as the section thickness increases. Layer II shows a small increase followed by a slight decrease, while an initial drop in the percentage of the core layer is followed by a steady increase.

Figures 4.25 and 4.26 show high magnification micrographs of a 1.5mm section of the unreinforced polymer, at the surface of the moulding, and at the boundary of layer III and IV respectively. Micrographs of the reinforced polymer, near the edge and the centre of the moulding are shown in figures 4.27 and 4.28.

4.3.2   Fracture Surfaces

A view of the cross section of a fracture surface, parallel to the flow direction, is given in figures 4.29 and 4.30. Figure 4.29 shows the fracture crossing a region of the skin, and then moving down an interface within the layer. The fracture tip is shown in figure 4.30.
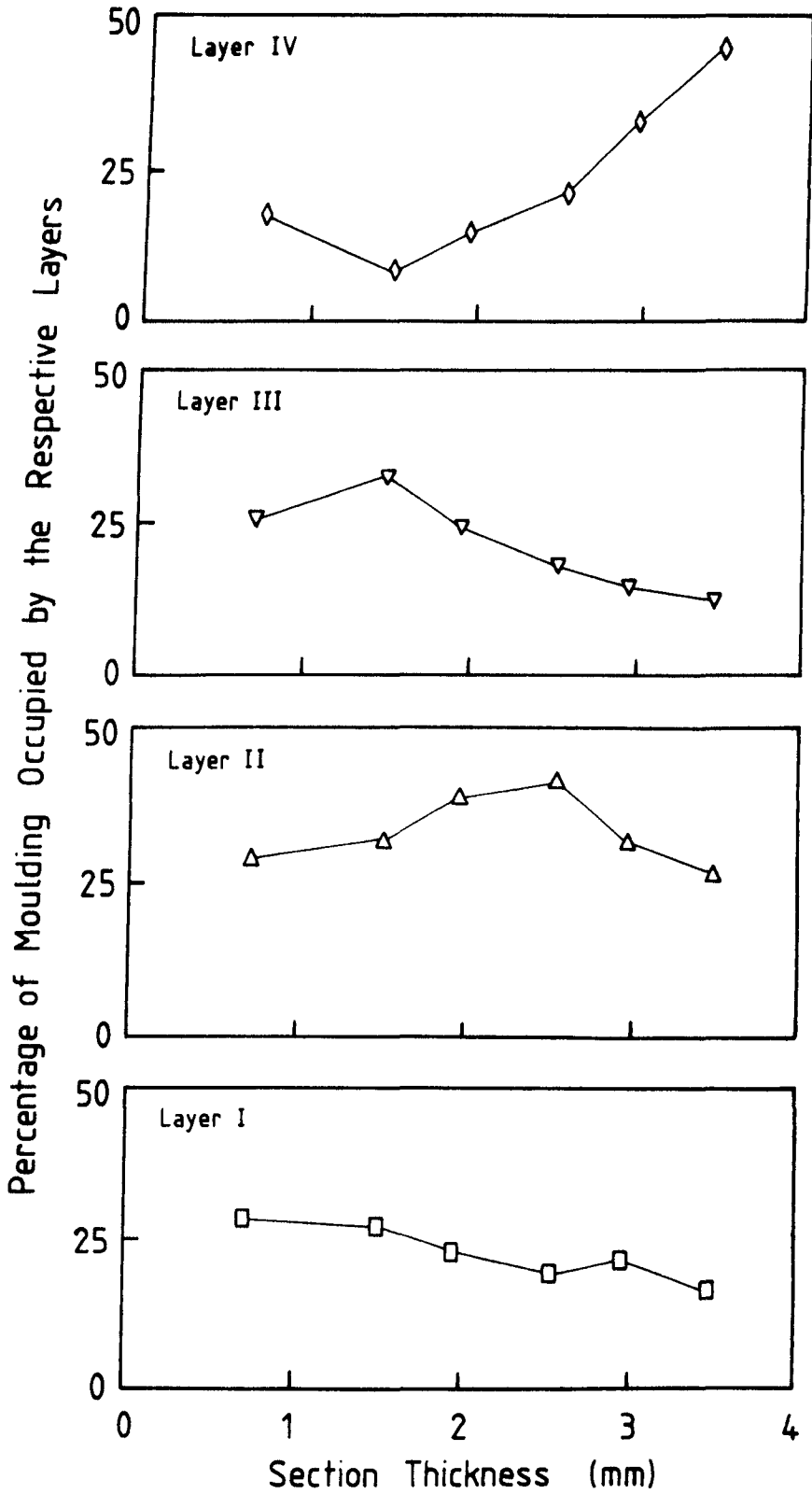
162

Figure 4.24. The thickness of the individual layers,
expressed as a percentage of the section thickness,
plotted against the section thickness.
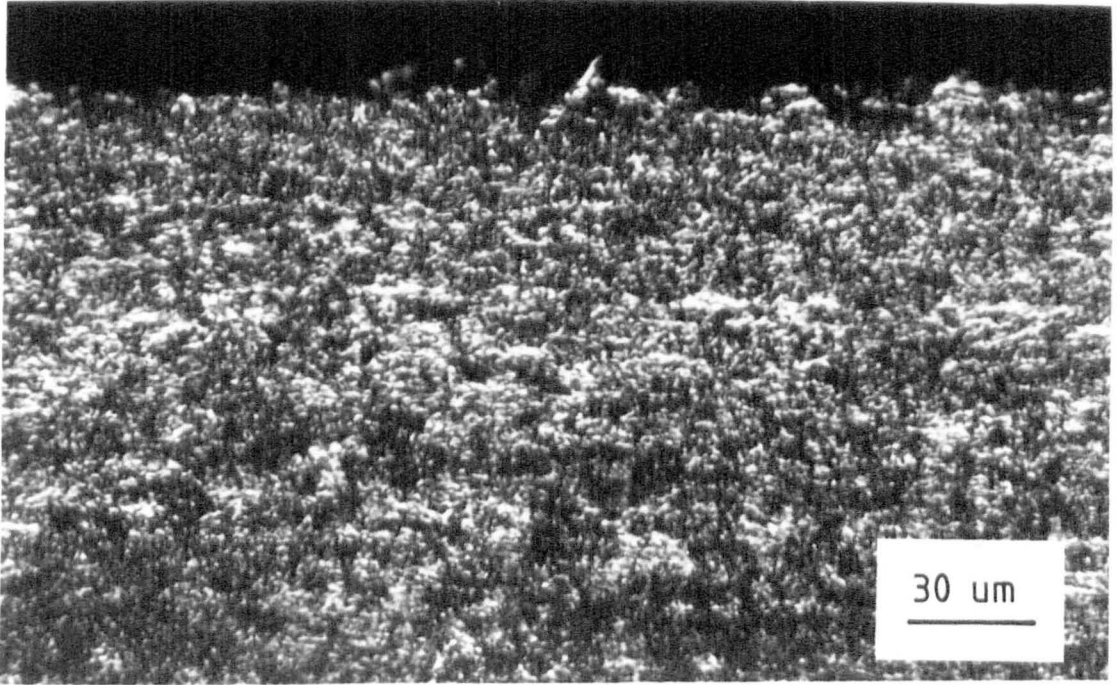
Figure 4.25. Optical transmitted light photograph of the unreinforced polymer, 1.5mm section at the surface of the moulding, layer I, parallel to the flow direction. Magnification ≈ 560.
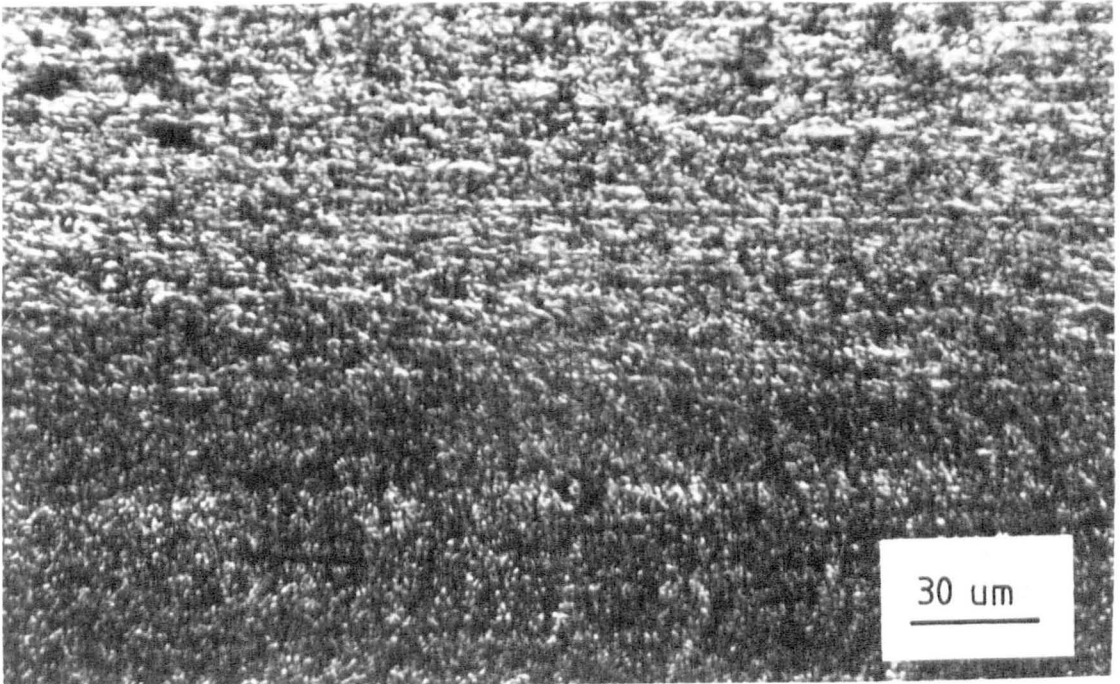
Figure 4.26. Optical transmitted light photograph of the unreinforced polymer, 1.5mm section at the interface between layers III an IV, parallel to the flow direction. Magnification ≈ 560.
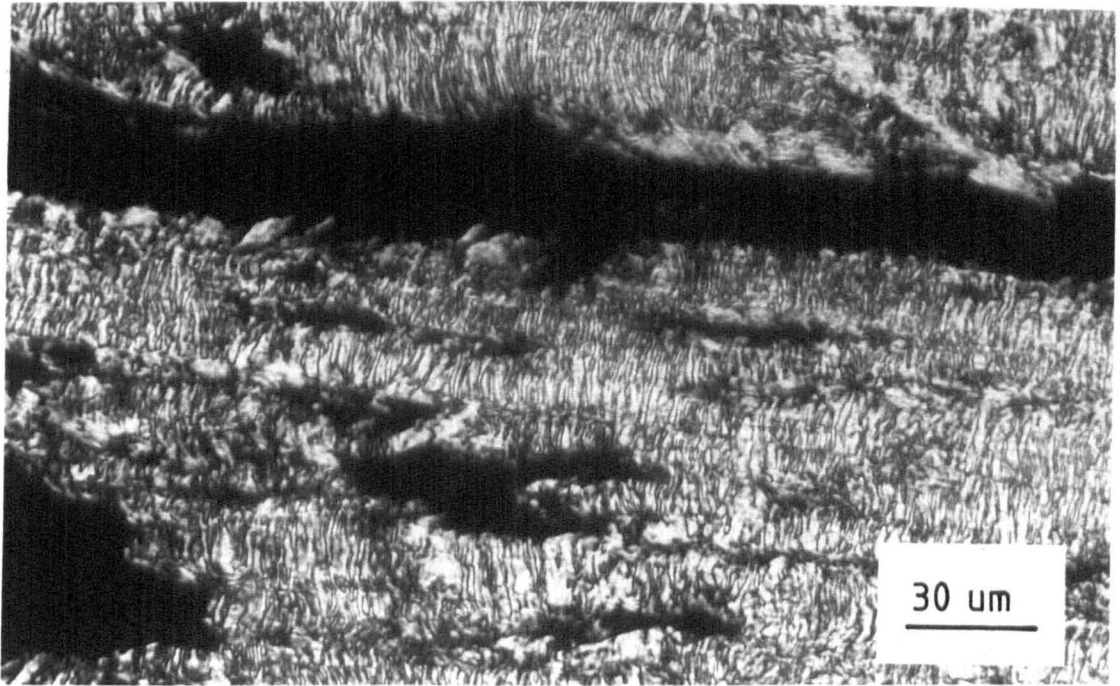
Figure 4.27. Optical transmitted light photograph of the reinforced polymer, 3.0mm section near the surface of the moulding, layer I, parallel to the flow direction. Magnification ≈ 560.

Figure 4.28. Optical transmitted light photograph of the reinforced polymer, 2.0mm section at the centre of the moulding, layer IV, parallel to the flow direction. Magnification ≈ 560.
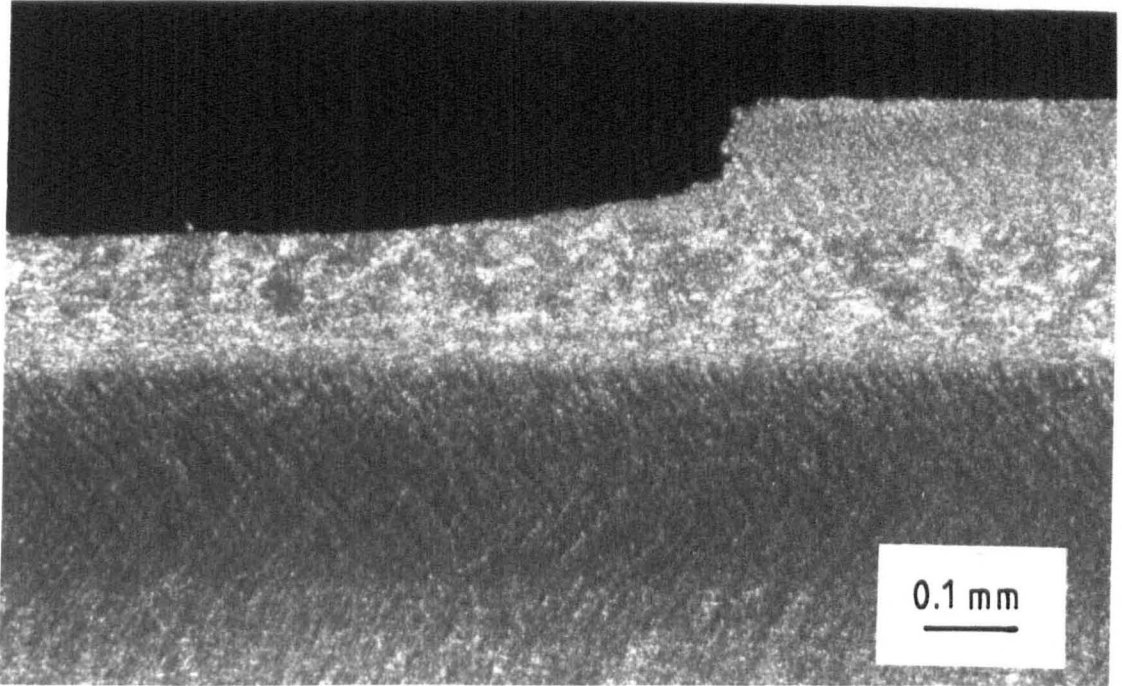
Figure 4.29. Optical transmitted light photograph of a
fracture surface for the unreinforced polymer, 2.5mm
section at the surface of the moulding, parallel to the
flow direction. Magnification ≈ 120.
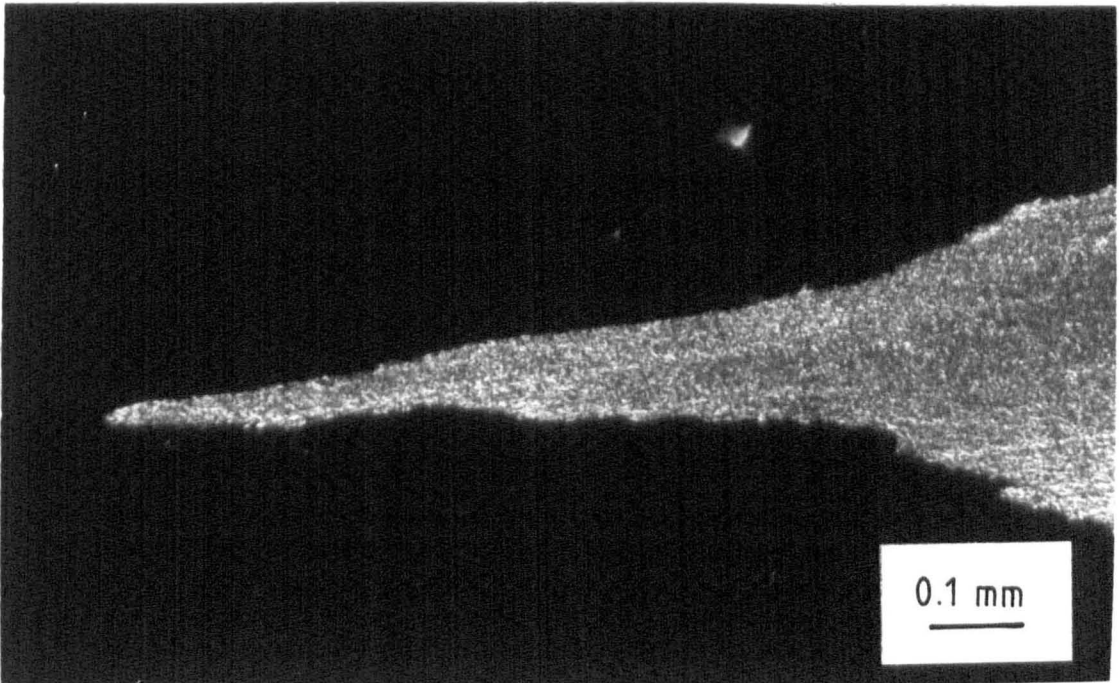
Figure 4.30. Optical transmitted light photograph of a
fracture surface for the unreinforced polymer, 2.5mm
section at the centre of the moulding, parallel to the
flow direction. Magnification ≈ 120.

Scanning electron micrographs of fracture surfaces, for
unreinforced specimens tested parallel to the flow, are
shown in figures 4.31 - 34. They indicate mouldings with
different levels of organisation. Micro fibrils, on the
submicron scale, are clearly visible.

Fracture surfaces for the glass reinforced polymer are
given in figures 4.35 - 38. The micrographs, for samples
tested parallel and perpendicular to the flow direction,
indicate a poor bond between the fibres and the matrix.
This is characterised by the large degree of fibre pull
out, and the clean appearance of the exposed fibres.
Figures 4.37 and 4.38, again show the hierarchical
organisation in the polymer.

4.3.3   Etch Morphology

The macroscopic layer structure is clearly visible on
samples of the polymer which have been etched. This can
be seen in figure 4.39, which shows the 2.0mm section,
parallel and perpendicular to the flow direction, and in
figure 4.40.

Figure 4.41 shows the microstructure at the centre of the
0.7mm section, parallel to the flow direction, while the
transition from layer III to IV is shown in figure 4.42
for the 3.0mm section, perpendicular to the flow.
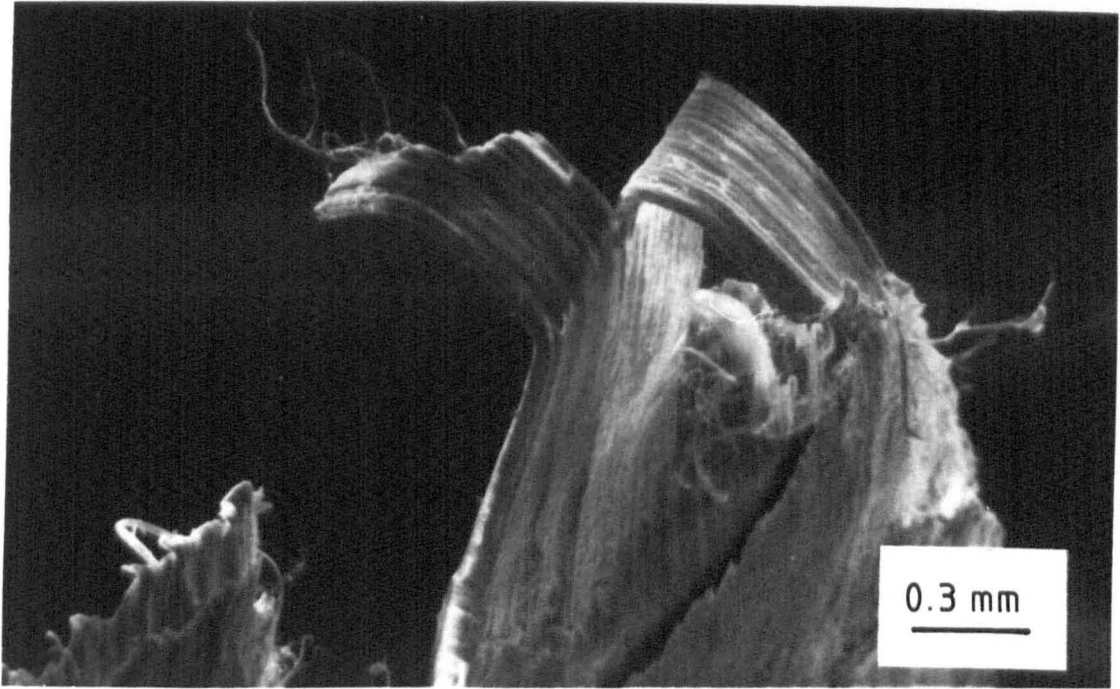
Figure 4.31. Scanning electron micrograph of a fracture surface for the unreinforced polymer, 1.5mm section, tested in tension, parallel to the flow direction. Magnification ≈ 50.
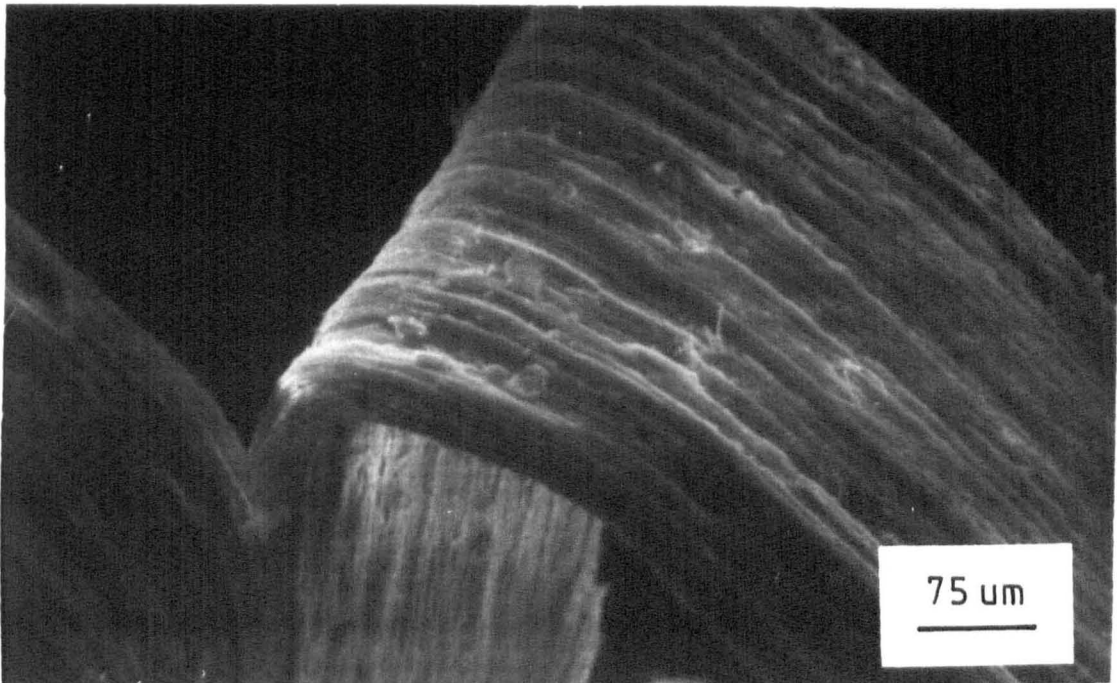
Figure 4.32. Scanning electron micrograph of a fracture surface for the unreinforced polymer, 1.5mm section, tested in tension, parallel to the flow direction. Magnification ≈ 200.

Figure 4.33. Scanning electron micrograph of a fracture
surface for the unreinforced polymer, 2.0mm section,
tested in tension, parallel to the flow direction.
Magnification = 50.
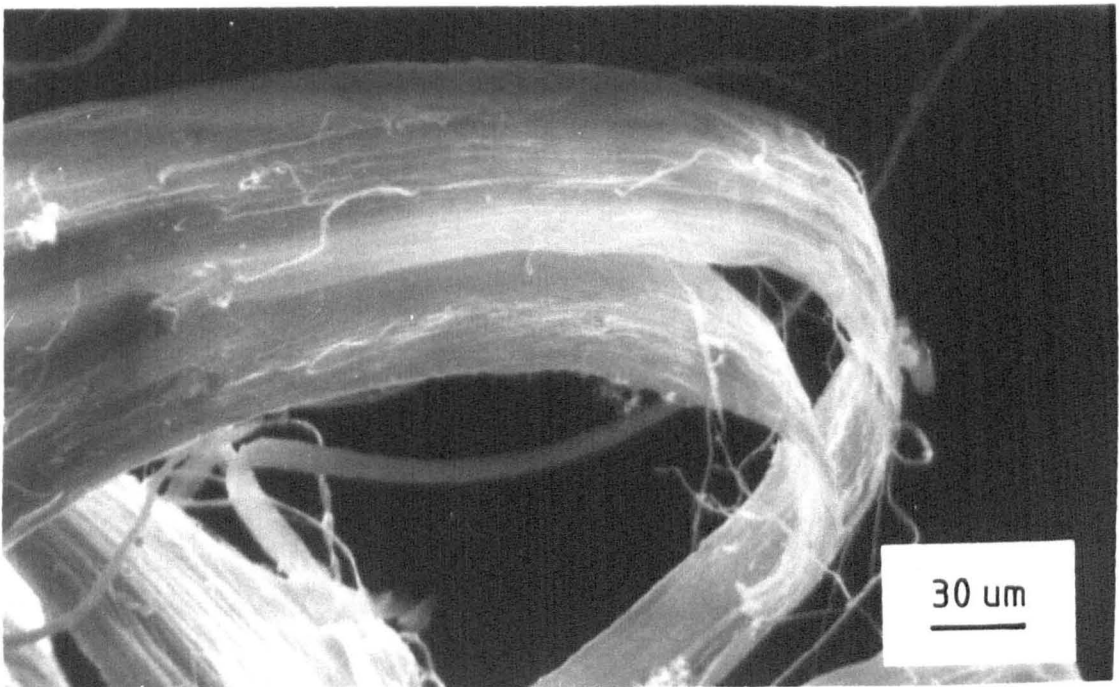
Figure 4.34. Scanning electron micrograph of a fracture
surface for the unreinforced polymer, 2.0mm section,
tested in tension, parallel to the flow direction.
Magnification = 400.
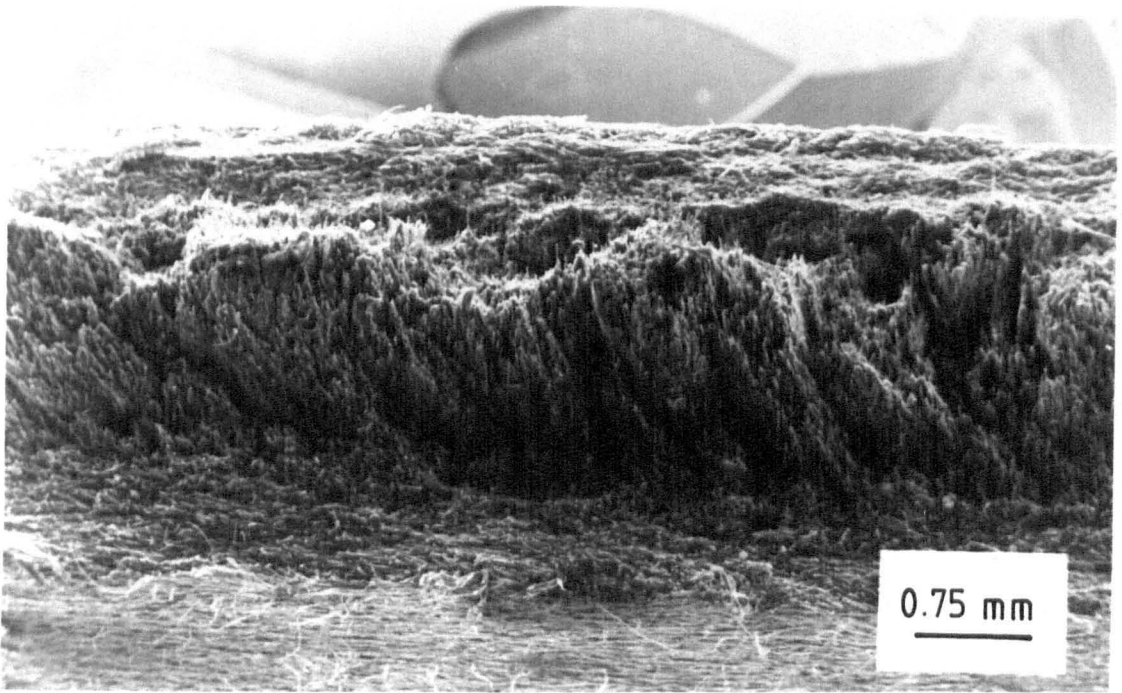
Figure 4.35. Scanning electron micrograph of a fracture
surface for the reinforced polymer, 3.5mm section, tested
in tension, perpendicular to the flow direction.
Magnification = 20.
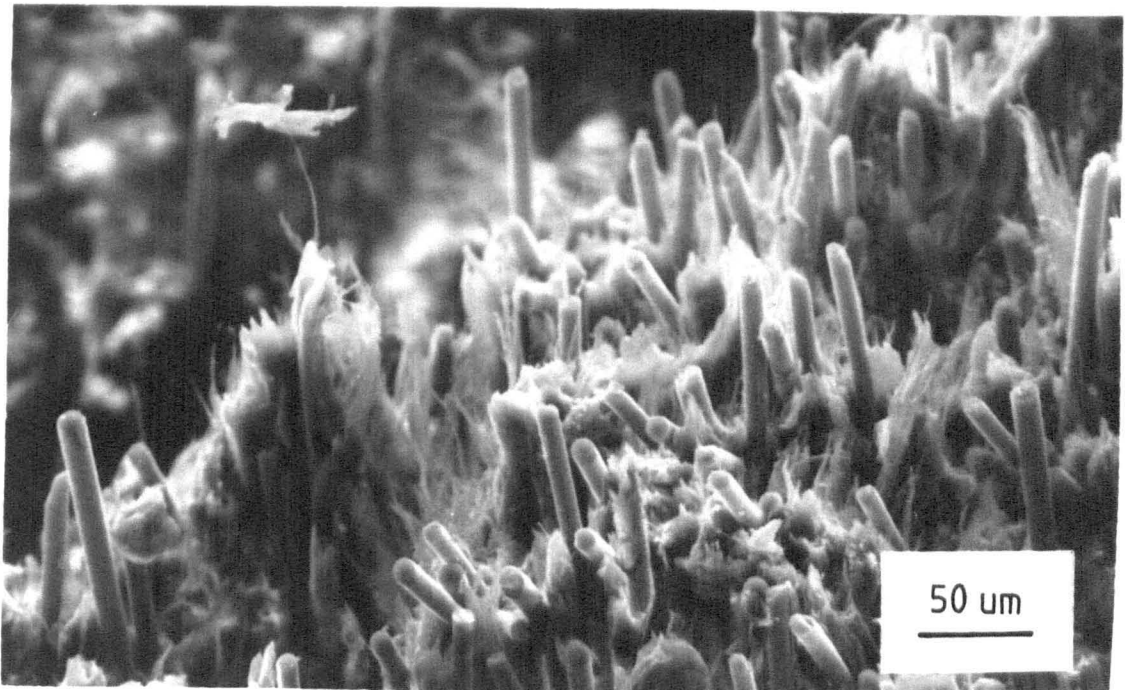
Figure 4.36. Scanning electron micrograph of a fracture
surface for the reinforced polymer, 3.5mm section, tested
in tension, perpendicular to the flow direction.
Magnification = 300.
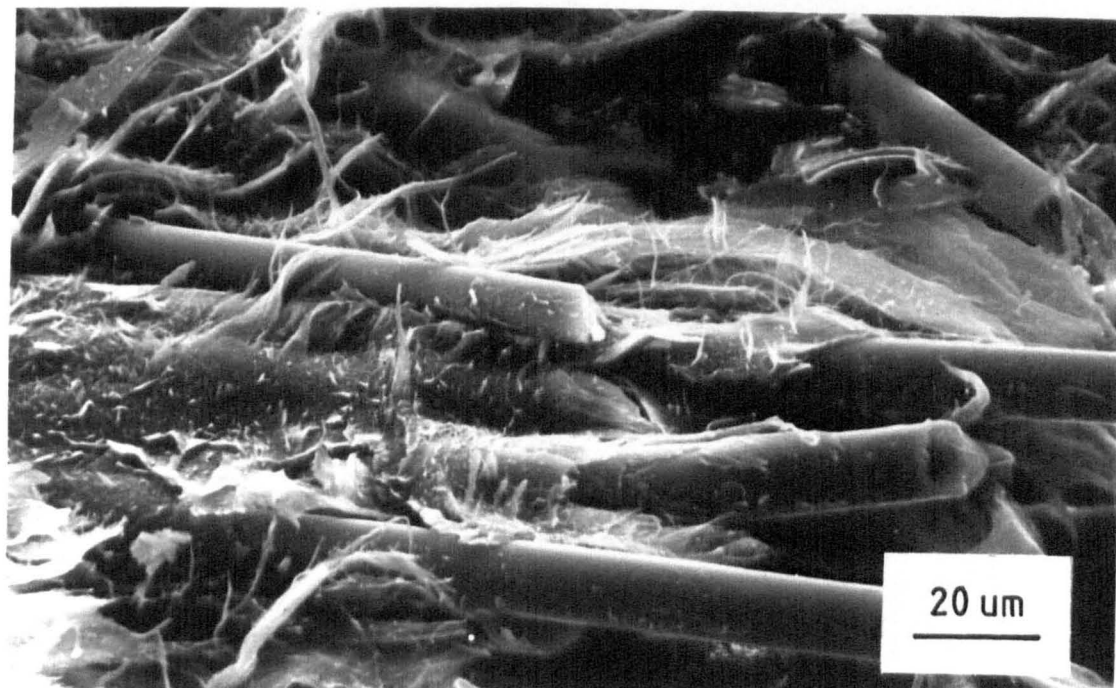
Figure 4.37. Scanning electron micrograph of a fracture
surface for the reinforced polymer, 3.5mm section, tested
in tension, parallel to the flow direction. Magnification
≈ 820.
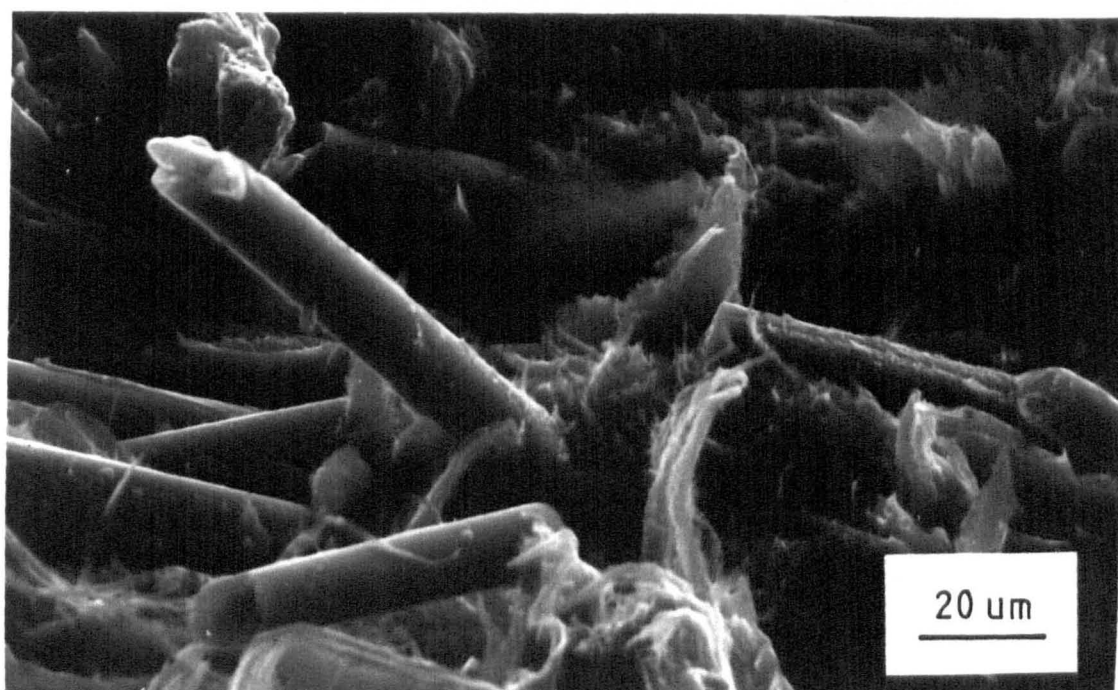
Figure 4.38. Scanning electron micrograph of a fracture
surface for the reinforced polymer, 3.5mm section, tested
in tension, parallel to the flow direction. Magnification
≈ 820.

171
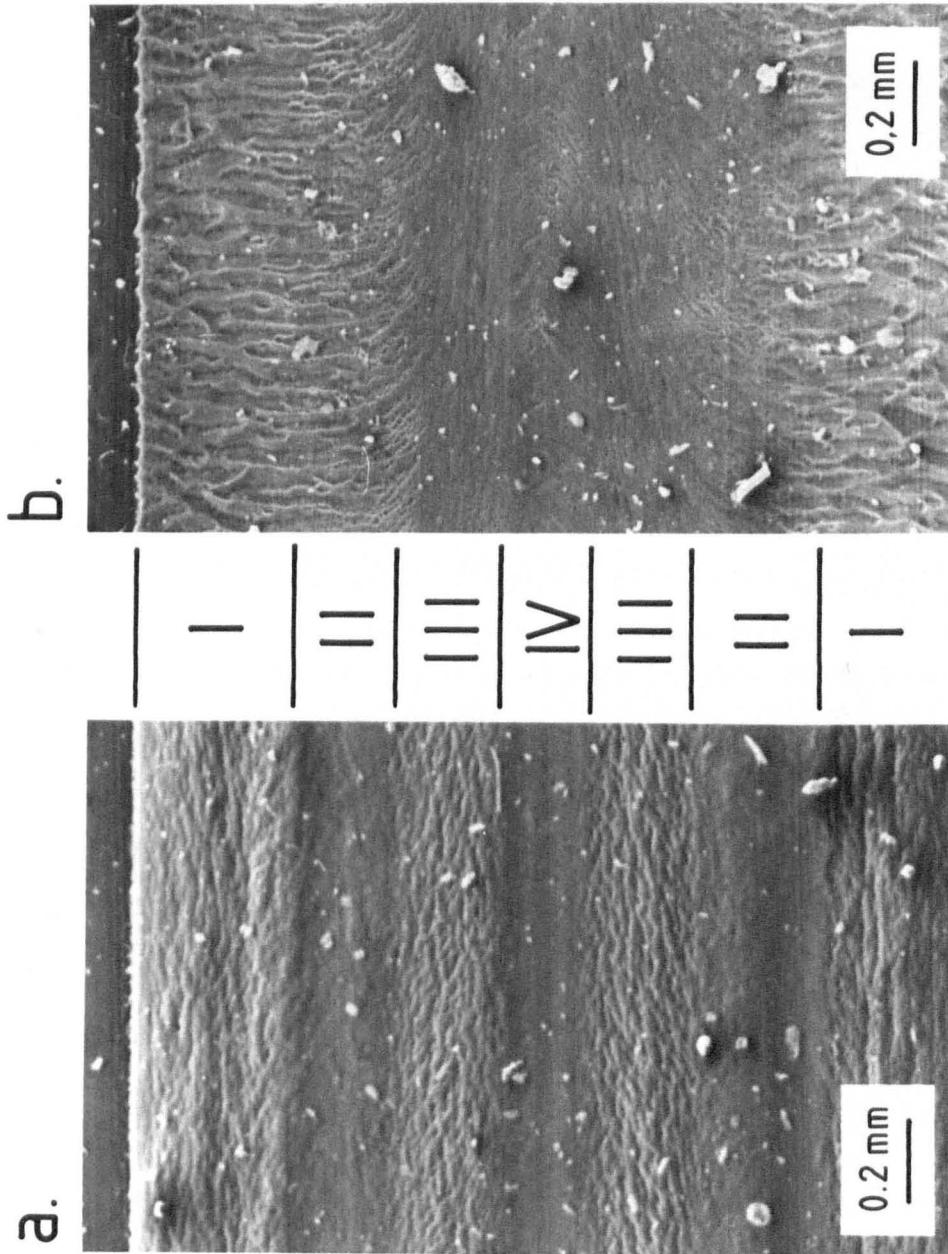
Figure 4.39. Scanning electron micrograph of an etched
surface for the unreinforced polymer, 2.0mm section,
indicating the individual layers. Magnification = 57.
(a) Perpendicular to the flow direction.
(b) Parallel to the flow direction.
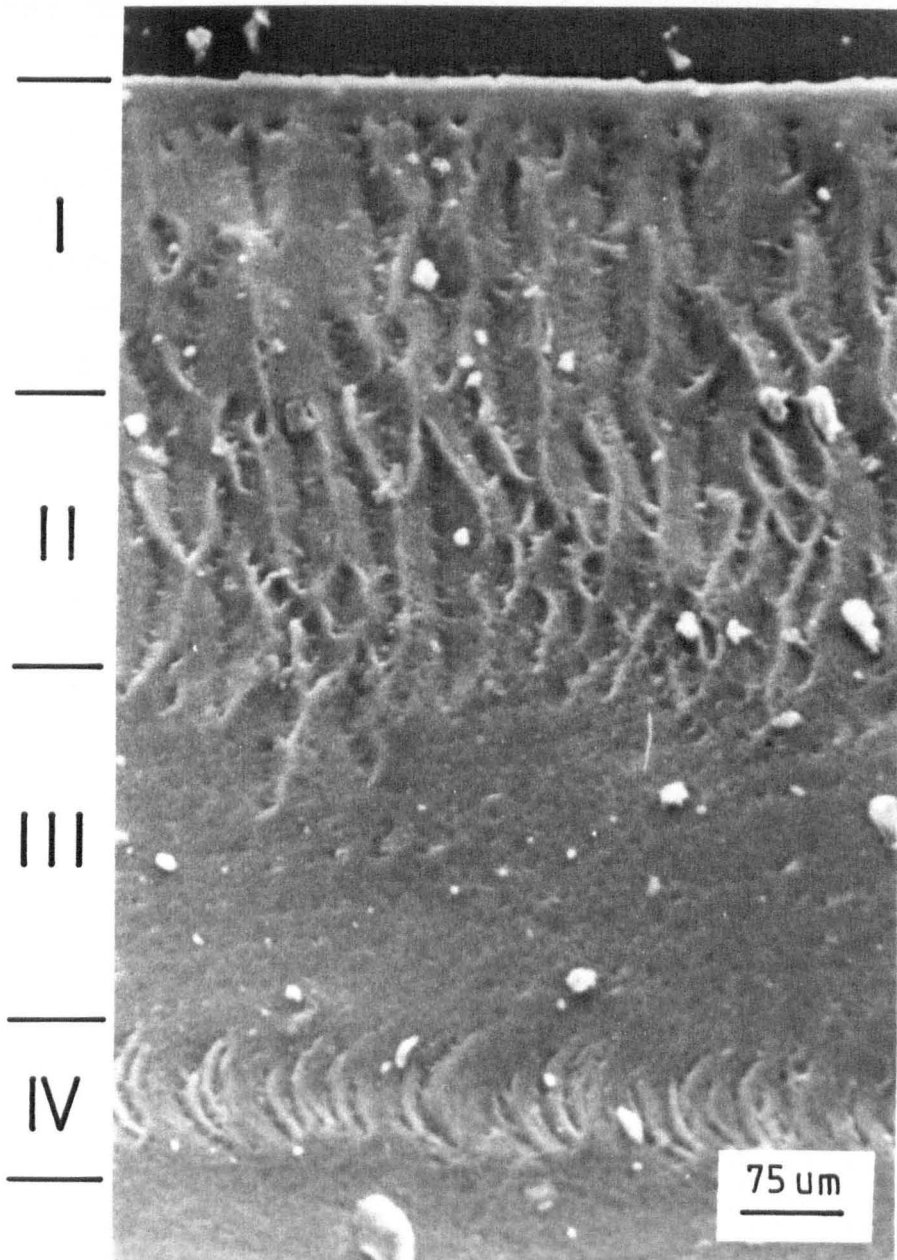
Figure 4.40. Scanning electron micrograph of an etched surface for the unreinforced polymer, 1.5mm section, parallel to the flow direction, indicating the individual layers. Magnification = 180.
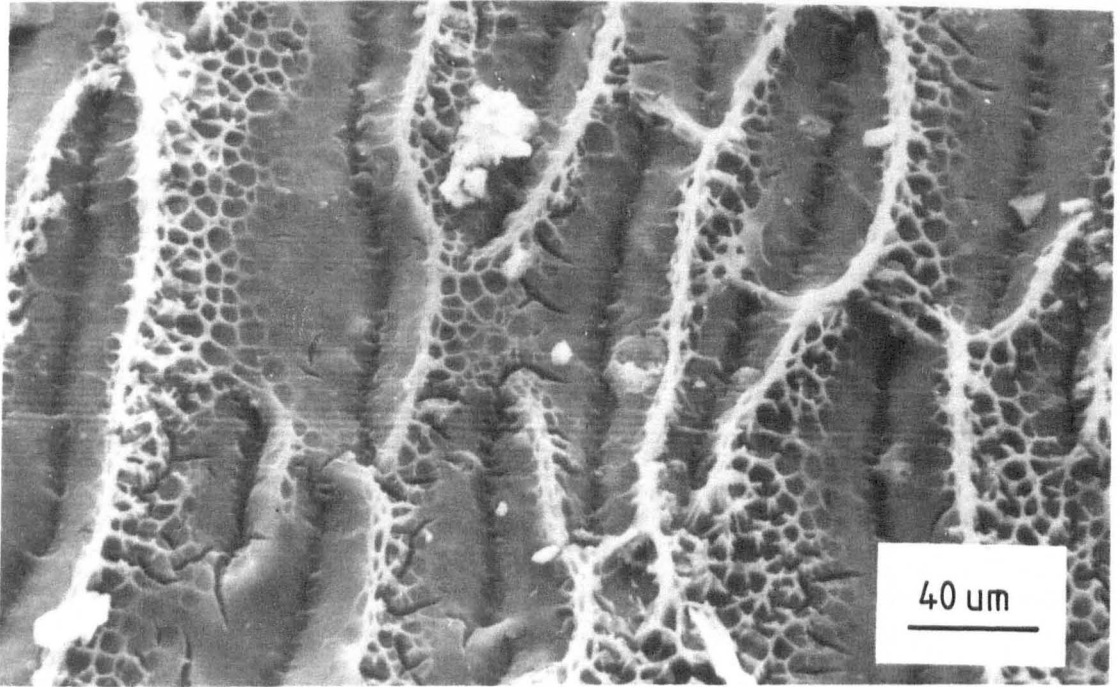
Figure 4.41. Scanning electron micrograph of an etched
surface for the unreinforced polymer, centre of the 0.7mm
section, parallel to the flow direction. Magnification
≈ 415.
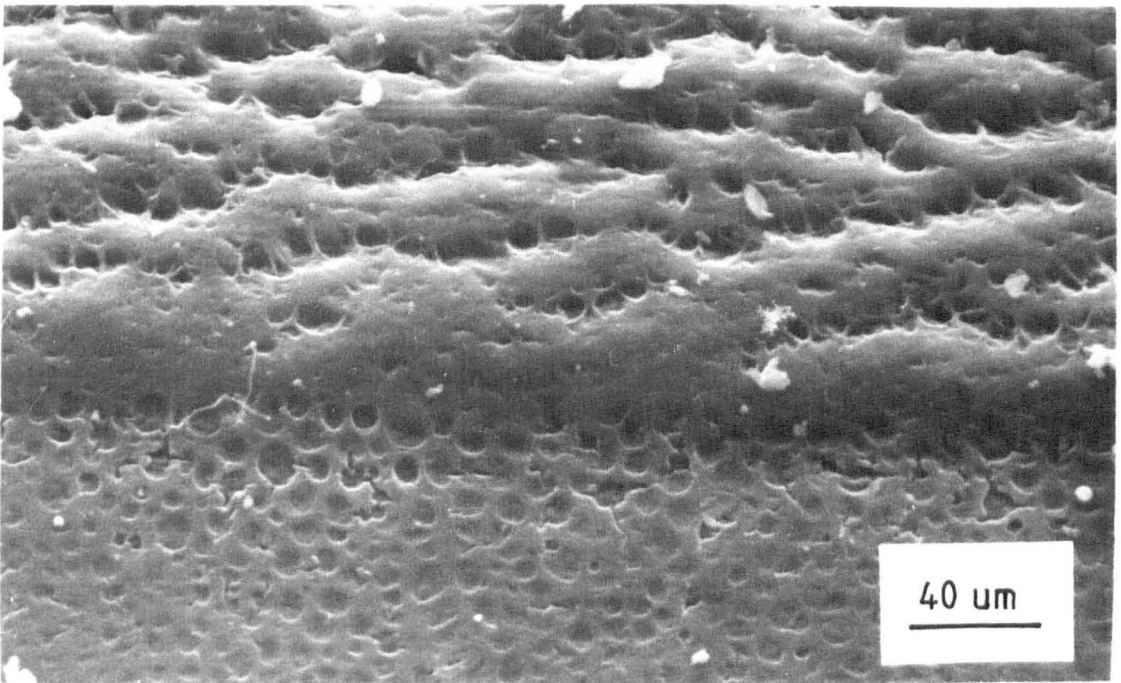
Figure 4.42. Scanning electron micrograph of an etched
surface for the unreinforced polymer, at the interface
between layer III and IV for the 3.0mm section,
perpendicular to the flow direction. Magnification ≈ 415.

4.3.4 X-Ray Diffraction

The results of the X-ray diffraction are presented in figure 4.43. Samples A and B shows bright diffraction spots in the equatorial direction, and arcs in the meridional direction. The equatorial reflection becomes broader in section C, while section D produces a pattern with only a little evidence of crystalline order. The core of the moulding, section E, reveals a diffuse meridional reflection.

The degree of crystalline orientation was evaluated, for each section, using the approximate method described in section 3.4.4.1. A plot of Hermans orientation function vs. the position of the sections through the thickness of the moulding is shown in figure 4.44.
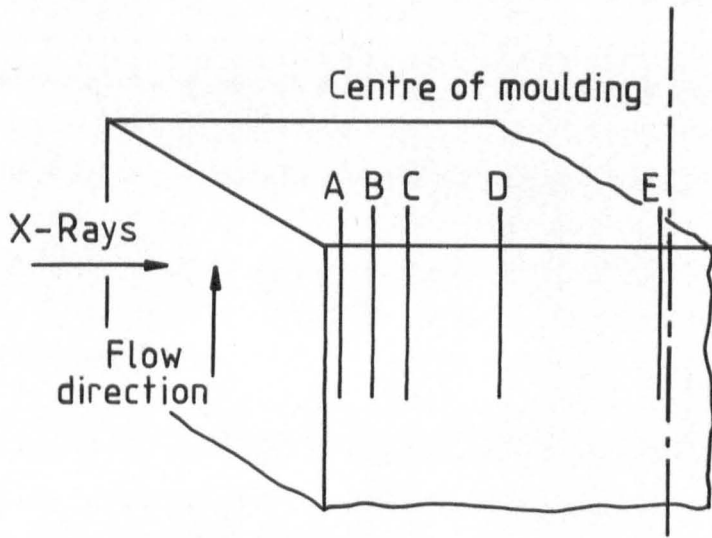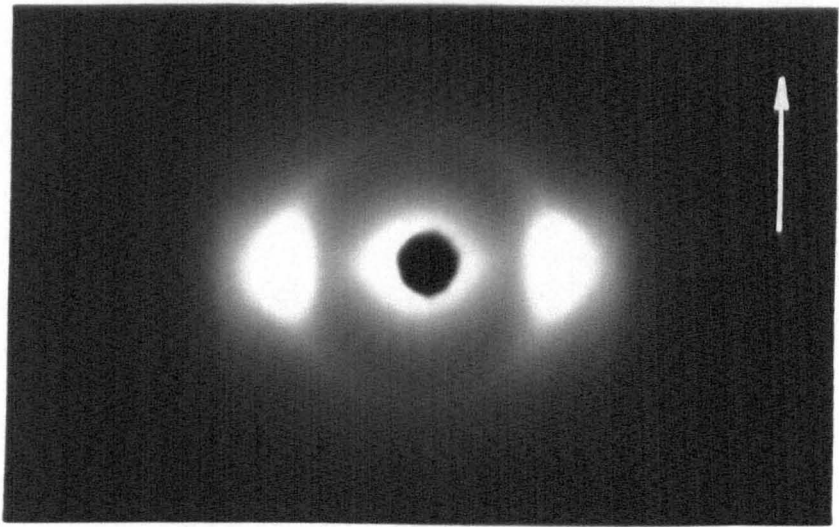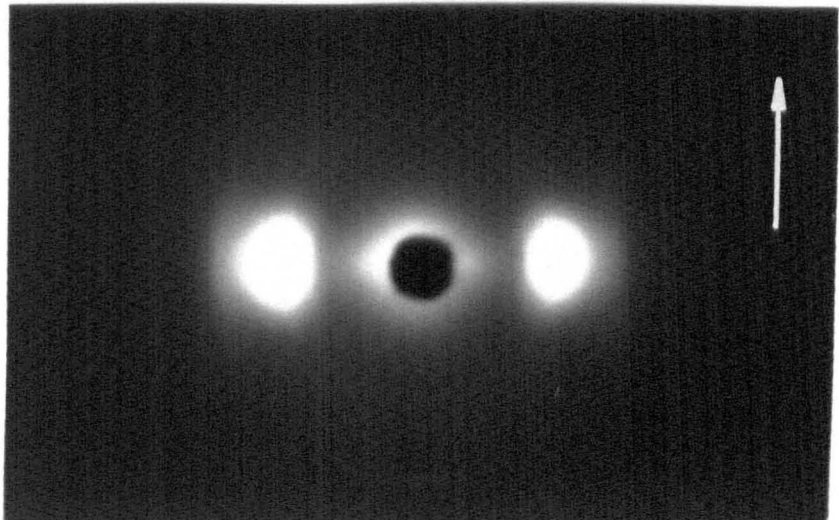
Figure 4.43. (i) Diagram of the position of the sections
through the thickness of the moulding.
(ii) X-ray radiograph of section A.
(iii) X-ray radiograph of section B.

176
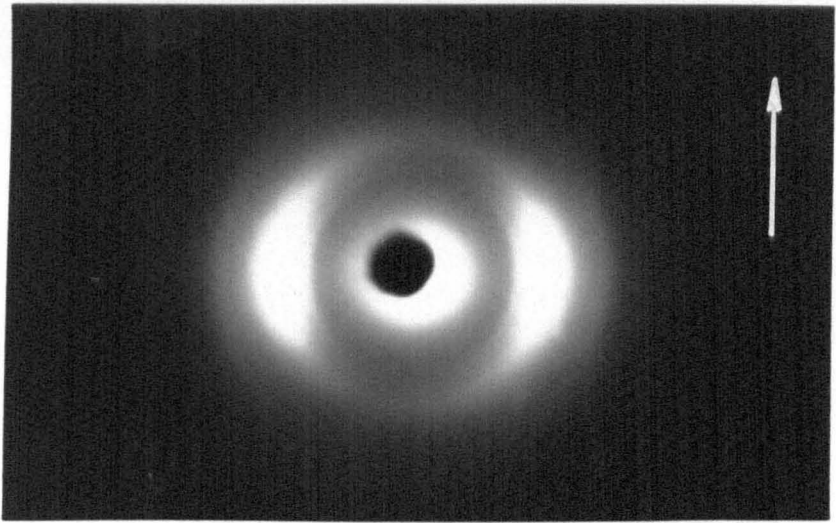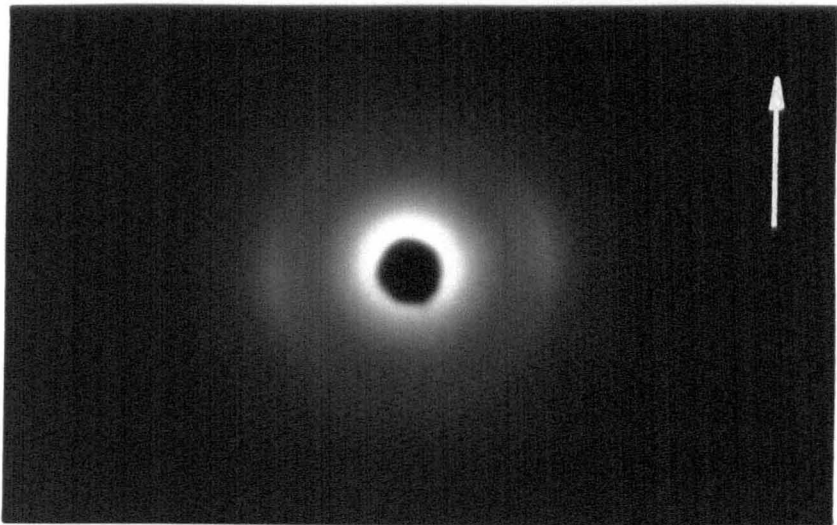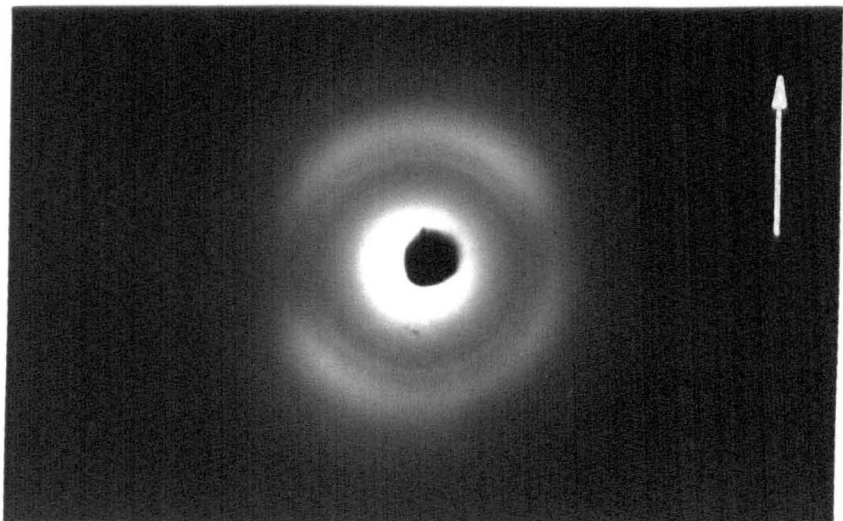
Figure 4.43. continued
(iv) X-ray radiograph of section C.
(v) X-ray radiograph of section D.
(vi) X-ray radiograph of section E.
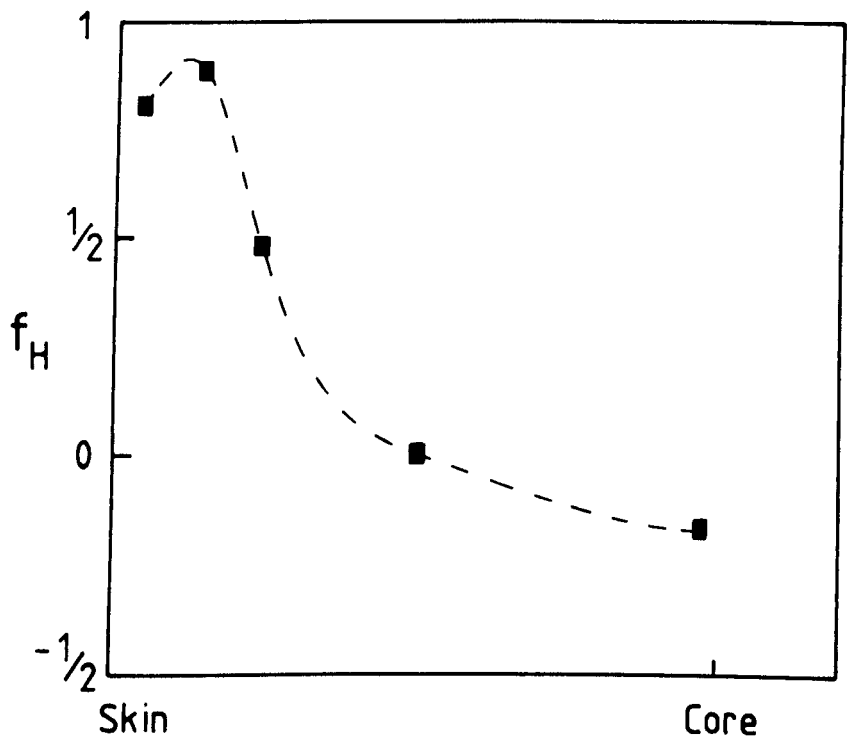
177

Figure 4.44. Hermans orientation function plotted against position through the thickness of the moulding.

CHAPTER 5

Discussion

5.1   Introduction

Thermotropic liquid crystalline polymers represent a
relatively new class of polymer which exhibits enhanced
mechanical properties, but does not require special
processing techniques. Chapter 1 gave a brief account of
the historical developments, while more specific topics
were reviewed in chapter 2. The methods of examining the
rheological properties, mechanical properties and
morphology were presented in chapter 3. The results, as
presented in chapter 4, will be discussed in this
chapter.

To aid the reader, relevant figures from the results
chapter have been reproduced, in a reduced format, and
placed as close as possible to the appropriate text.

5.2   Materials

The polymer under investigation was a thermotropic liquid crystalline polymer produced by ICI, from the SRP1 range. Two grades of polymer were examined, a general purpose injection moulding grade, and an equivalent grade with 27% glass reinforcement.

The polymer was produced from four monomers, HBA, HQ, IA and HNA. Work carried out previously by Kiss[44] on a similar polymer system indicated a minimum in the melting point at a HBA content of 35 mole%, very close to the fraction employed by ICI. With only a small fraction of HNA being used the majority of the remaining polymer is comprised of equal mole fractions of IA and HQ.

HBA is able to react with itself to form runs of HBA units resulting in long stiff sequences. IA and HQ are diacids and diols respectively, and are able to react together to form IA/HQ pairs which can then react with other pairs to produce runs. Hence the polymer chain consists of runs of HBA and IA/HQ units with occasional HNA groups.

It was mentioned in section 2.1.4.1 that the almost perfect regularity of para linked aromatic chains must be disrupted in order for the polymer to be processable. In this particular polymer this is achieved by the

incorporation of a meta link into the polymer chain. The
IA in this polymer introduces the meta link, thus
reducing chain linearity and allowing the polymer to melt
at a reasonable temperature.

A representation of possible sequences for HBA and IA/HQ
are shown in figure 5.1. It is clearly seen that the HBA
units are able to form a linear chain, while the IA/HQ
pairs produce a meandering chain. Although bond rotation
will be possible, the overall linear structure of the
chain will be maintained. The runs of HBA and IA/HQ will
also produce chains which will be planar in nature. This
will permit relatively close, transverse packing of the
chains and may promote the formation a sheet-like
structure.
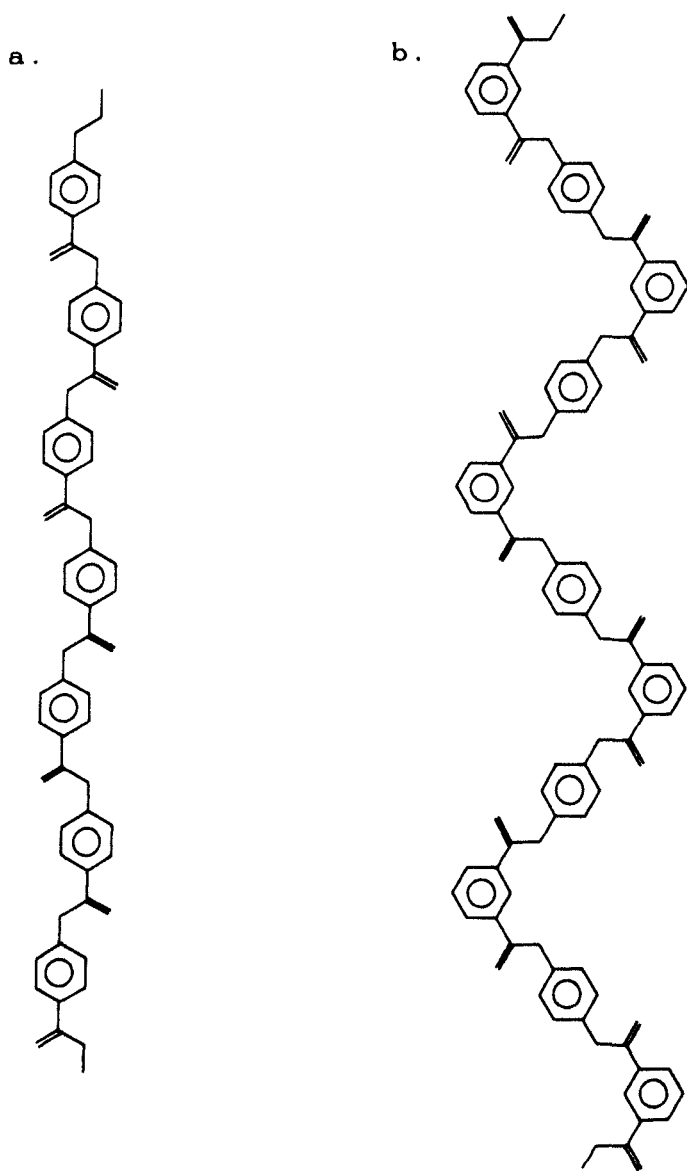
Figure 5.1. Schematic representation of molecular chains in SRP1.
a. A run of HBA monomers producing linear chain.
b. A run of IA/HQ pairs forming a meandering chain.

5.3 Rheology

5.3.1 Temperature Dependence

Figures 4.3 and 4.4 show the temperature dependence of
the shear and extensional viscosity respectively. The
shear viscosity shows a large decrease from 325°C to
330°C, after which it is virtually temperature
independent. The extensional viscosity shows a similar
dependency, except that the initial drop in viscosity is
proportionally smaller than that seen in the shear
viscosity, and at the lower strain rates there is a
minimum at 340°C.

Some information relating to the temperature dependence
may be obtained from the DSC trace is shown in figure
5.2[116]. The heating trace shows two main features, a
transition at 130°C and a broad melting endotherm at
301°C. For the rheological work, the endotherm is the
important feature.

This endotherm corresponds to the transition from the
solid state to the nematic phase. By constructing a base
line to the trace, the start and finish temperatures,
labelled T1 and T2, can be calculated. These were found
to be approximately 248°C and 334°C respectively. Hence,
above 334°C it may be assumed that the polymer is fully
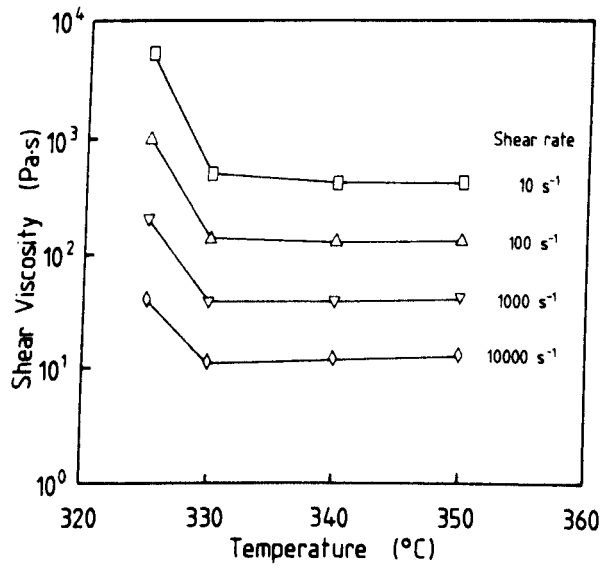
Figure 4.3. Shear viscosity vs. temperature, for the
unreinforced polymer, using laboratory rheometer.
Calculated at shear rates of 10, 100, 1000 and 10000s⁻¹.

Figure 4.4. Extensional viscosity vs. temperature, for
the unreinforced polymer, using laboratory rheometer.
Calculated at strain rates of 1, 10, 100 and 1000s⁻¹.

184
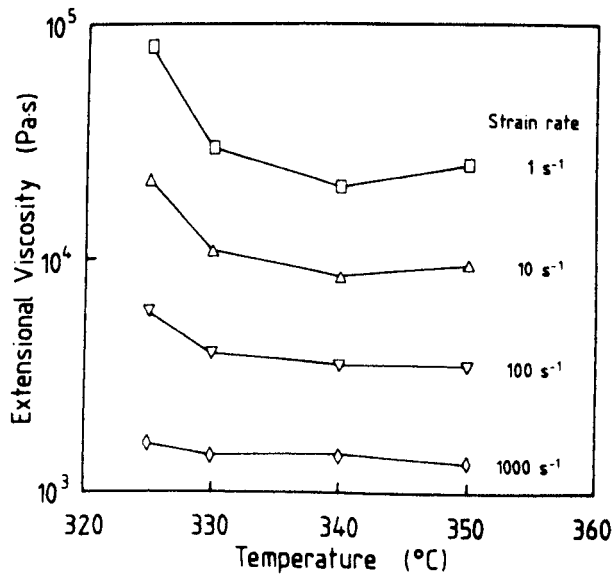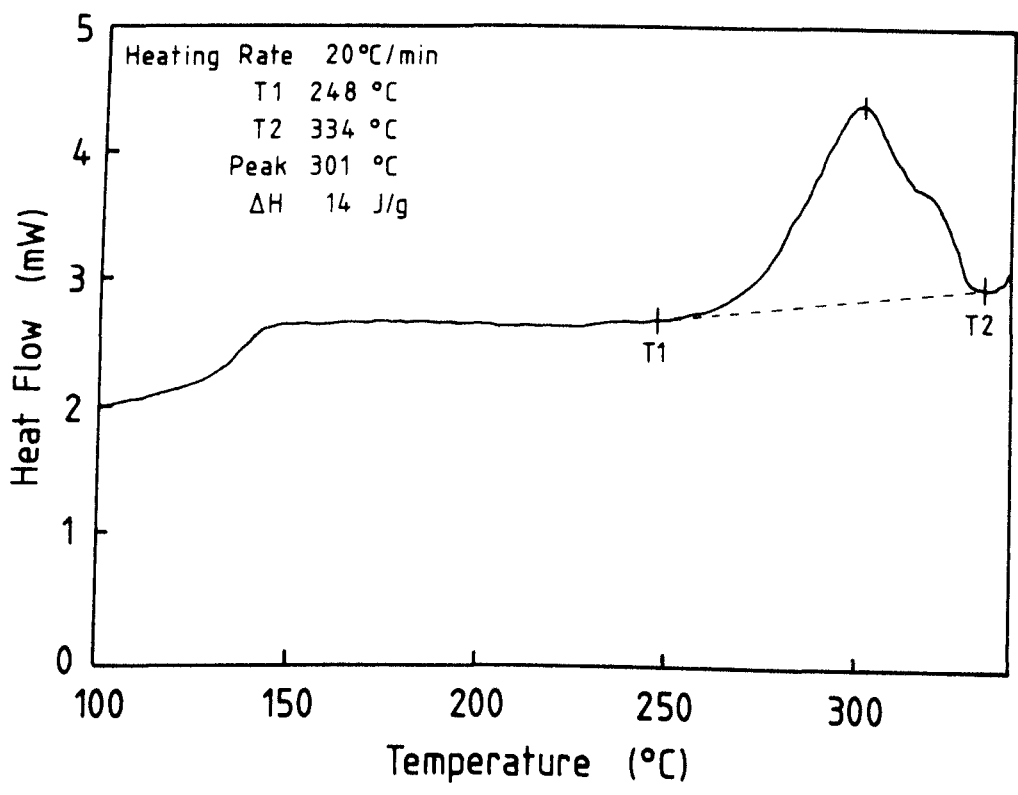
Figure 5.2. DSC thermogram showing a heating trace for SRP1, produced at a heating rate of 20°C/min.

185

in the nematic phase.

At a temperature of 325°C the polymer will not be completely in the liquid phase, and as a result of this it exhibits a relatively high viscosity. The values of the viscosity attained above 325°C appear to indicate that at a temperature of 330°C a nematic structure has fully developed.

Although the DCS trace indicates a value of 334°C for T2, this temperature is dependent on the heating rate, and may be associated with an error in the region of ±2°C. Also, the melt temperature is subject to errors, due to variations in the barrel temperature, which may again be about ±2°C. Another possible factor for the appearance of a nematic structure at 330°C, is that the flow process may help to promote the formation of the nematic state at a slightly lower temperature than when the polymer is at rest.

As the temperature is raised above 330°C the viscosity changes very little, up to a temperature of 350°C. In conventional thermoplastic polymers an increase in temperature results in a decrease in viscosity, which can be measured by a relative fluidity index[100]. A drop in viscosity by a factor of 1.2 to 2.5 is usually observed for a 10°C increase in temperature. This behaviour is clearly not apparent with this particular LCP.

The constant viscosity, observed above 330°C, may be explained by assuming that there is a competitive process taking place between the temperature, lowering the viscosity, and the proportion of isotropic phase, raising the viscosity. Thermotropic LCPs are known to show a transition from an anisotropic to an isotropic state, although it is sometimes not observed due to polymer decomposition.

Biphasic structures, in the form of anisotropic and isotropic phases, have been observed for lyotropic solutions, and are predicted by Flory's lattice model[4]. Kiss also postulated the existence of a biphasic melt to explain the temperature dependence of a thermotropic polymer consisting of HBA, IA and HQ[44].

Although Kiss provided no direct evidence for the existence of a biphasic melt, the conditions necessary for its formation were shown to be possible. Also, the results of etching certain thermotropic polymers has indicated a biphasic structure in mouldings. Hedmark et al.[87] found morphologies in a HBA/PET polymer which indicated a discontinuous PET phase in the form of spherical particles. Hence, without evidence to the contrary, the presence of an anisotropic and an isotropic phase appears to be the best explanation for the observed temperature dependence of the viscosity.

At 350°C the extruded polymer appeared dark brown in colour, suggesting that degradation had occurred. Under normal processing conditions the polymer has a light brown, or cream colour. For this reason, a detailed examination of the shear and extensional flow properties was performed at 340°C, below the temperature at which degradation started, but still in the region of constant viscosity. This temperature also corresponds to the processing temperature, as recommended by ICI[63].

5.3.2 Shear and Extensional Flow

Figure 4.5 shows a plot of the wall shear stress against shear rate at 340°C. The slight non-linearity of the plots indicates that the shear flow is not fitted exactly by the power law model. However, the slight curvature indicates that the flow may be adequately described by a power law relationship over an order of magnitude of shear rate. Thus, the power law constants, as calculated by constructing a tangent to the curve, will be valid over an order of magnitude, centred around the shear rate at which they were calculated. A similar degree of curvature is observed for the extensional flow, as illustrated by figure 4.8.

Values for the shear and extensional flow constants and viscosities for some engineering thermoplastics are
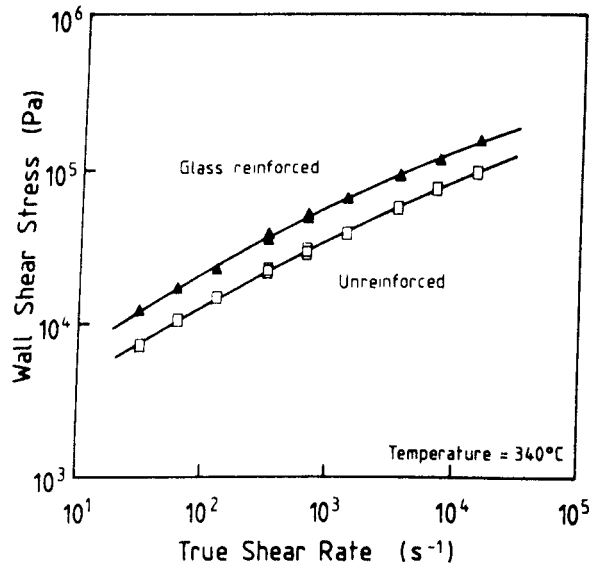
188

Figure 4.5. Log τ_w vs. Log Γ, for the glass reinforced and unreinforced polymer, from the laboratory rheometer at 340°C.

Figure 4.8. Log σ vs. Log ϵ, for the glass reinforced and unreinforced polymer, from the laboratory rheometer at 340°C.

189
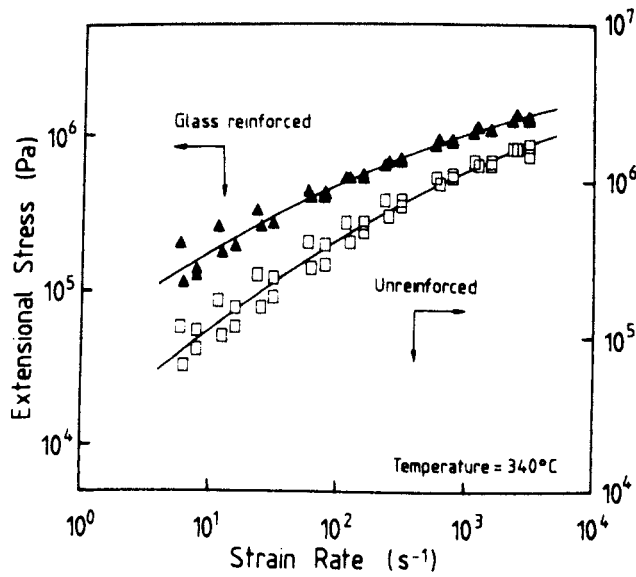
compared in tables 5.1 and 5.2[108,111]. It can be seen that at 1000 s^{-1}, the shear viscosity of SRP1 resembles that of the lower viscosity melts used in the production long fibre reinforced polymers. Comparing the values of extensional viscosity, calculated using the Gibson model, at a strain rate of 1000 s^{-1}, it can be seen that SRP1 is similar to that of an injection moulding grade of polypropylene, but an order of magnitude greater than that of grades of nylon and polypropylene used in the production of long fibre reinforced polymers. The power law index also differs considerably. For other thermoplastics, the Gibson model has indicated power law indices in the region of 0.8 to 0.9. A value of approximately 0.4 for SRP1 indicates an extensional viscosity which is more sensitive to variations in strain rate.

The near power law behaviour of the shear and extensional viscosities, over the strain rates covered, does not support the concept of a three stage flow curve as proposed by Onogi and Asada[50]. However, it is not possible to completely discount the Onogi-Asada model due to the limited range of shear rates over which the present experiments were performed. The direction of curvature may indicate a transition to a Newtonian plateau at low shear rates, but this can not be confirmed by the rheological methods used in this study. The method of capillary rheometry is unsuitable for obtaining data

Material	Temp. (°C)	G	m	η_s (Pa·s)
SRP1	340	2031	0.412	34.9
PP [108]	240	4771	0.343	51.0
PP* [111]	240	611	0.523	22.7
Nylon 66* [108]	285	62.1	0.810	16.7

Table 5.1. Shear flow constants, and shear viscosity at a shear rate of 1000 s^{-1}. '*' indicates base resin used for long fibre reinforced polymers.

Material	Temp. (°C)	H	n	η_e (Pa·s)
SRP1	340	80000	0.385	1145
PP [108]	240	2800	0.914	1546
PP* [111]	240	626	0.809	168
Nylon 66* [108]	285	356	0.901	179

Table 5.2. Extensional flow constants, and extensional viscosity at a strain rate of 1000 s^{-1}. '*' indicates base resin used for long fibre reinforced polymers.

Nb. Numerical values of the power law constants, G and H, correspond to strain rates in s^{-1}, and stresses in Pa.

at low shear rates, and to obtain data below $10s^{-1}$ apparatus such as cone-and-plate rheometers would have been desirable.

5.3.3 Glass Reinforcement

The effect of the addition of glass fibres on the rheological properties is shown in figures 4.5 and 4.8. The fibres produce a consistent increase in the wall shear stress over the entire range of shear rates studied. The effect on the extensional stress is less clear. At low strain rates the reinforcement increases the extensional stress, but the two curves intersect at a strain rate of approximately $286s^{-1}$, resulting in the glass filled polymer having the lower extensional stress at the high strain rates.

Comparing these results with those obtained for other glass filled polymers, table 5.3, a similar pattern for the shear viscosity is observed. The reinforcement increases the constant G, while slightly reducing m, with the net result being an increase in the viscosity. The shear viscosity of SRP1 is again similar to that of the low viscosity melts. Table 5.4 shows the constants for the extensional flow. The reinforcement again increases the constant H, while reducing the power law index n. For the melts used in the production of long fibre reinforced

Material	Temp. (°C)	G	m	η_s (Pa·s)
SRP1	340	3603	0.402	57.8
PP [108]	240	6224	0.301	49.8
PP (SF) [111]	240	1365	0.430	26.6
PP (LF) [111]	240	1641	0.485	46.9
Nylon 66 (SF) [108]	285	376	0.683	42.0
Nylon 66 (LF) [108]	285	1418	0.572	73.6

Table 5.3. Shear flow constants, and shear viscosity at a shear rate of 1000 s^{-1} for glass filled polymers. SF = short glass fibre ($\approx$ 0.4mm), LF = long glass fibre ($\approx$ 10mm), with low viscosity base polymer.

Material	Temp. (°C)	H	n	η_e (Pa·s)
SRP1	340	145000	0.279	995
PP [108]	240	10000	0.678	1081
PP (SF) [111]	240	8866	0.691	1047
PP (LF) [111]	240	73600	0.707	9747
Nylon 66 (SF) [108]	285	3820	0.766	761
Nylon 66 (LF) [108]	285	221000	0.555	10240

Table 5.4. Extensional flow constants, and extensional viscosity at a strain rate of 1000 s^{-1} for glass filled polymers. SF = short glass fibre ($\approx$ 0.4mm), LF = long glass fibre ($\approx$ 10mm), with low viscosity base polymer.

Nb. Numerical values of the power law constants, G and H, correspond to strain rates in s^{-1}, and stresses in Pa.

polymers this produces a large increase in the
extensional viscosity, believed to be associated with the
alignment of the reinforcement[103]. However, for SRP1
and an injection moulding grade of polypropylene, a
reduction in the extensional viscosity is observed. The
similarity between the extensional viscosity of the
filled and unfilled LCP may indicate that a high degree
of molecular orientation is occurring in the convergence
of the die. The orientation of the rod-like molecules
then having a similar effect to the aligned fibres.

5.3.4   Batchelor Equation

The Batchelor equation was introduced in section 2.5.9 as
a method of examining the effect of elongated units on
the extensional viscosity. In previous work by McClelland
and Gibson[103] and also by Corscadden[111], the
Batchelor equation has been successfully used to predict
the effective aspect ratio of fibres in a thermoplastic
matrix. In addition to such studies, it is envisaged that
due to the highly extended nature of the rod-like
molecules in LCPs, it may be informative to apply the
Batchelor equation to the unreinforced polymer. In so
doing it is believed that an aspect ratio of a flowing
unit within the polymer can be calculated.

5.3.4.1 Carreau-Ysasuda Equation

The Batchelor equation is essentially a relationship
between Newtonian viscosities, and for this reason it was
felt to be desirable that an estimate of the zero-rate-
viscosity, η_o, was made. Although the quadratic curve
fitted to the experimental points gave a good fit, within
the shear rate covered, such a curve will not behave
sensibly once outside the empirical points. For this
reason, the results were fitted using a Carreau-
Ysasuda[117] type equation:

$$\frac{\eta - \eta_\infty}{\eta_o - \eta_\infty} = \left[1 + (\Omega \cdot \Gamma)^f \right]^{(1-m)/f} \qquad 5.1$$

where Ω and f are constants, η_∞ is the viscosity at an
infinitely high shear rate, and will be assumed to be
zero, and the other symbols have their usual meaning. In
this particular model, at low shear rates the viscosity
is Newtonian in character, with $\eta = \eta_o$, while at high
rates it predicts a power law relationship, where
$\eta = (\eta_o \cdot \Omega^{(1-m)}) \cdot \Gamma^{(1-m)}$.

Varying the constant f alters the rate at which the
viscosity goes from being Newtonian to power law. Initial
plots with $f = 2$, the Bird-Carreau model, were felt to
curve too rapidly, and so f was set equal to unity to
allow the transition from Newtonian to power law
behaviour to occur over a wider shear rate interval. The

results of this fit on the experimental data are shown in figures 5.3a - d. It is accepted that the values of η_o, shown in table 5.5, for the shear and extensional viscosities are some what arbitrary, due to the lack of data available at low shear rates, but are believed to be reasonably valid within the limits imposed by the experimental data available. Also, the values of the power law constants are in close agreement to those calculated from the quadratic fit, lending credence to the Carreau model.

5.3.4.2   Effective Aspect Ratio of Glass Fibres

Knowing the extensional Newtonian viscosity of the fibre reinforced polymer, $\eta_{o \bullet F}$, and the shear and extensional Newtonian viscosity of the base polymer, $\eta_{o \bullet R}$ and $\eta_{o \bullet R}$, the Batchelor equation, 2.16 (p. 88), may be rewritten as follows:

$$\frac{L}{D} = \left[\frac{3 \cdot (\eta_{o \bullet F} - V_R \cdot \eta_{o \bullet R})}{4 \cdot V_f \cdot \eta_{o \bullet R}} \ln\left[\frac{\pi}{V_f}\right] \right]^{\frac{1}{2}} \qquad 5.2$$

From this, the effective aspect ratio of the flowing unit may be estimated.

Using the Newtonian viscosities given in table 5.5, equation 5.2 predicts L/D = 18.2. By means of optical microscopy, the effective fibre length, L^*, as described

196
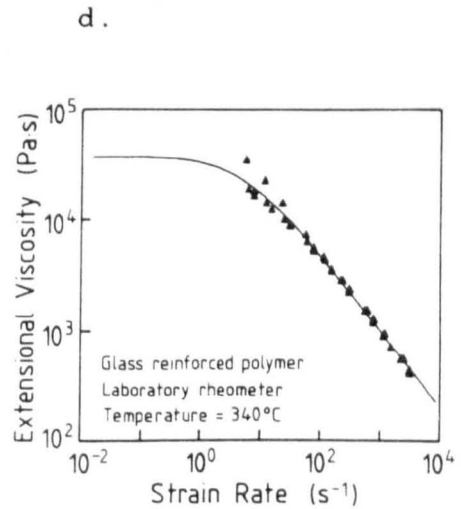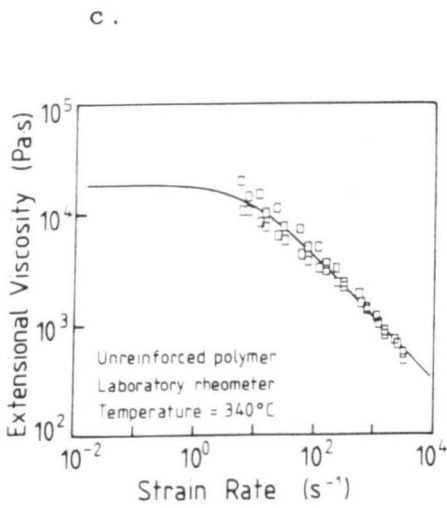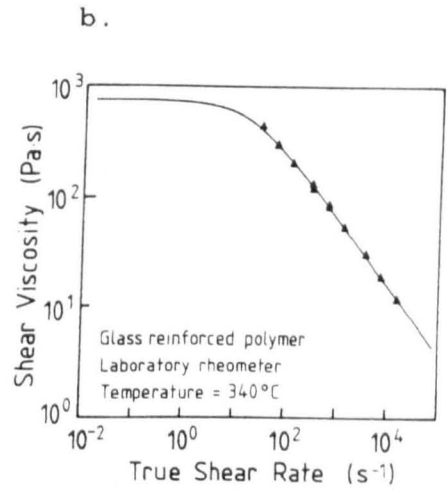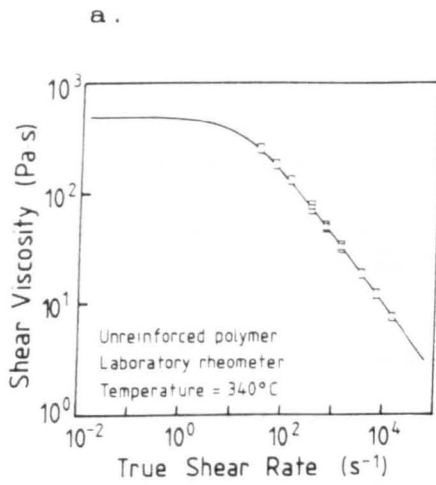
Figure 5.3. Results of fitting the Carreau-Ysasuda
equation to the empirical data points.
a. Shear viscosity vs. true shear rate for the
   unreinforced polymer.
b. Shear viscosity vs. true shear rate for the
   reinforced polymer.
c. Extensional viscosity vs. strain rate for the
   unreinforced polymer.
d. Extensional viscosity vs. strain rate for the
   reinforced polymer.

197

Constants	Unreinforced polymer	Glass reinforced polymer
η_{ao}	494 Pa·s	739 Pa·s
η_{oo}	18100 Pa·s	37100 Pa·s
m	0.388	0.372
G	2710	4980
n	0.425	0.313
H	60400	113000

Nb. Numerical values of the power law constants, G and H, correspond to strain rates in s^{-1}, and stresses in Pa.

Table 5.5. Constants obtained from the Carreau model for the unreinforced and glass reinforced polymer.

by equation 8.16 in Appendix 1, was estimated. In the as-received granules this was found to be approximately 378μm, giving an aspect ratio of 31.5. Assuming the fibre length remains constant, an aspect ratio of 18.2 implies a flowing unit with a diameter of approximately 20.8 μm. This value is equivalent to a single glass fibre which is surrounded by a thin cylinder of the polymer, or it may indicate an aggregation of fibres flowing as a single unit.

5.3.4.3 Effective Flowing Unit in The Base Polymer

It was mentioned previously that the rod-like nature of the molecules in LCPs may act as elongated entities which could be examined using the Batchelor equation. Rearranging equation 2.15 (p. 87), as shown below,

$$
\frac{L}{D} = \left[\frac{3}{4 \cdot V_f} \left[\frac{n_{o\bullet R}}{n_{o\bullet R}} - 3 \right] \ln \left[\frac{\pi}{V_f} \right] \right]^{\frac{1}{2}}
\qquad 5.3
$$

an effective aspect ratio for a flowing unit in the unfilled polymer may be evaluated. In the original equation, V_f corresponds to the volume fraction of fibres, or aligned unit. In this analysis the volume fraction will be equivalent to the proportion of polymer which is in the highly extended state. It is probable that this will be equal to the amount of polymer which becomes oriented in the flow direction during processing.

199

We will assume that is between 30% and 70%, implying that V_f is in the region of 0.3 to 0.7. Substituting the values of $\eta_{o \bullet R}$ and $\eta_{o \bullet R}$ into equation 5.3, aspect ratios of 14.0, and 7.3 are obtained for volume fraction of 0.3 and 0.7 respectively.

5.3.4.4 Power Law Version of Batchelor Equation

Equation 5.3 essentially predicts an aspect ratio for the polymer at a low strain rate, which is constant for a given volume fraction. However, it is probable that during processing, the higher strain rates would elongate the flowing units, and so increase the effective aspect ratio. The effect on the flowing unit of increasing the strain rate may be investigated by use of a power law version of the Batchelor equation[118]:

$$\eta_e = \frac{\dfrac{V_f}{m+2} \cdot 2G\epsilon^{(m-1)} \cdot \left[\dfrac{L}{D}\right]^{(m+1)} \cdot \left[\dfrac{1-m}{m}\right]^m}{\left[1 - \left[\dfrac{V_f}{\pi}\right]^{(1-m)/2m}\right]^m} \qquad 5.4$$

which may be rearranged to give a prediction of the aspect ratio:

$$\left[\frac{L}{D}\right]^{(m+1)} = \frac{\eta_e \cdot \left[1 - \left[\dfrac{V_f}{\pi}\right]^{(1-m)/2m}\right]^m}{\dfrac{V_f}{m+2} \cdot 2G\epsilon^{(m-1)} \cdot \left[\dfrac{1-m}{m}\right]^m} \qquad 5.5$$

The values of L/D obtained by substituting the power law constants, given in table 5.5 into equation 5.5, for a number of volume fractions and strain rates, are shown in table 5.6. The results of using the power law version of the Batchelor equation clearly indicate that as the strain rate is increased, so the aspect ratio of the flowing unit increases. For a volume fraction of 0.5, the aspect ratio increases from 10.7 to 12.1 as the strain rate goes from 25 s^{-1} to 2500 s^{-1}.

The relatively low values of the aspect ratios obtained for the polymer appear to indicate a flowing unit which consists of more than a single chain. It would seem probable that the flowing unit is an aggregate of a number of aligned chains which then flow as a single unit. Such a unit could be envisaged as a domain in which the chains lie parallel to each other.

5.3.4.5 <u>Limitations of Batchelor Equation</u>

Although the Batchelor equation has been successfully used to examine the aspect ratio of flowing units in the filled and unfilled polymer, its limitations should also be noted.

As mentioned in section 5.3.4.1, the values of η_o can not be taken as exact values, due to the lack of data at low

V_f	Strain Rate (s^{-1})						
	25	50	100	250	500	1000	2500
0.3	16.4	16.7	17.0	17.4	17.7	18.1	18.5
0.4	12.9	13.1	13.4	13.7	13.9	14.2	14.6
0.5	10.7	10.9	11.1	11.3	11.5	11.8	12.1
0.6	9.1	9.3	9.4	9.7	9.9	10.0	10.3
0.7	7.9	8.1	8.2	8.4	8.6	8.8	9.0

Table 5.6. Aspect ratios of the flowing unit in the unfilled polymer, for a number of volume fractions and strain rates, calculated using equation 5.5.

shear rates, and hence may be considered as a lower

limit. Errors associated with these viscosities will

in turn lead to errors in the aspect ratios calculated

using equations 5.2 and 5.3. Use of the power law version

of the Batchelor equation, 5.5, and the more accurate

power law constants, will reduce the errors introduced

when estimating values of L/D. However, due to these

errors the aspect ratios quoted in the previous sections

should not be taken as exact values, but as approximate

values which illustrate trends and patterns in the aspect

ratio of the flowing units.

5.3.5 <u>Experimental Methods</u>

The experimental methods employed in this work were

chosen in order to characterise the rheological

properties of the polymer under conditions relevant to

injection moulding. Capillary rheometry has the advantage

over other rheological test methods in that the polymer

flows through similar regimes to those present in

injection moulding machines. However there are two main

differences between a laboratory rheometer and an

injection moulding machine. These are the size and the

deformation history undergone by the polymer.

In order to produce shear rates which are comparable to

those seen in injection moulding it is necessary to have

capillaries with small diameters, typically 1mm. This may produce problems, for example, shear heating may become important, or if a filled polymer is being studied, log jamming of fibres may severely affect the flow. With gate dimensions in the order of 4mm, these effects are greatly reduced in the injection moulding machine.

The deformation history can also affect the results, particularly of reinforced material. During the charging process of the injection moulding cycle, the fibre length can be significantly reduced, depending on the work done by the screw. In the laboratory rheometer the material is fed directly into the barrel, and hence the initial fibre length is retained. Work by Corscadden[111] on glass reinforced polypropylene, with fibre lengths of 5mm and 10mm, showed that the longer fibre material had higher shear and extensional viscosity. However, plaques which were injection moulded from the 10mm fibre material, and subsequently feed through the rheometer produced results not dissimilar from the 5mm fibre material.

To overcome these problems the use of an instrumented injection moulding machine was felt to be of considerable interest in obtaining rheological data. This method has the advantage that the polymer undergoes the same deformation history and flows through the same geometries. However, a major disadvantage of this method is the requirement for large quantities of material.

Hence, the use a laboratory capillary rheometer, in conjunction with an instrumented injection moulding machine can produce rheological data relevant to the actual process of injection moulding.

The results obtained from the laboratory rheometer and the instrumented injection moulding machine, for the glass reinforced polymer, are shown in figures 4.6 and 4.9. Over the shear rate examined, the results from the two different test methods were in close agreement, despite the difference in the thermal and shear history undergone by the polymer.

As mentioned above, the injection moulding process can result in a reduction in the fibre length. This can cause the measured value of the shear and extensional viscosity to be higher in the capillary rheometer, compared to the injection moulding machine. Measurement of the fibre lengths in the original granules and injection moulded plaques indicated that the average fibre length had been reduced from approximately 0.35 mm to an about 0.24 mm. This may indicate that single fibres are not the major flowing unit, but that the flowing unit is an aggregate of a number of fibres and/or polymer domains.

Cogswell has found that pre-shearing LCPs can produce a significant drop in viscosity[58]. However, even though the polymer will be heavily sheared in the injection
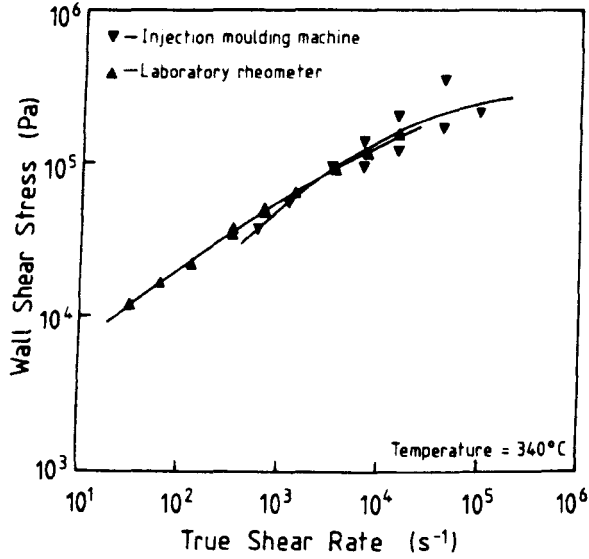
Figure 4.6. Log τ_w vs. Log Γ, comparing the results for
the glass reinforced polymer using the laboratory
rheometer and the injection moulding machine, at 340°C.

Figure 4.9. Log σ vs. Log ε, comparing the results for
the glass reinforced polymer using the laboratory
rheometer and the injection moulding machine, at 340°C.

205
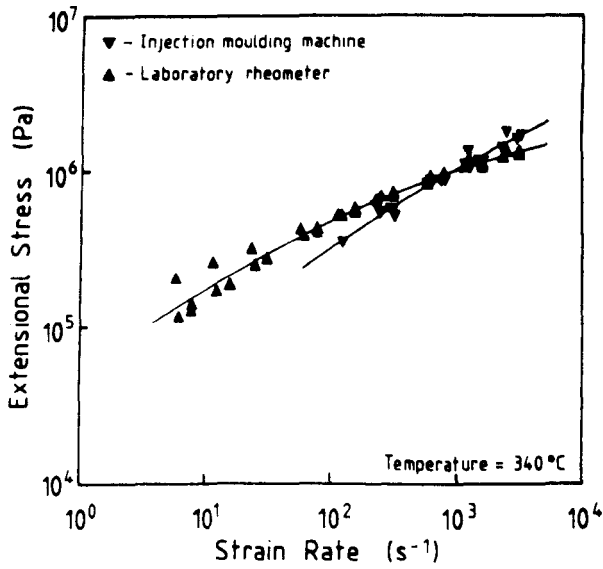
moulding machine, prior to injection, there appears
little difference in the value of the wall shear stress,
or the extensional stress, obtained from the different
apparatus.

5.3.6 Rheological Model

The ability of Gibson's rheological model to describe the
flow behaviour of the polymer is demonstrated by figures
4.11, 4.12 and 4.13. Over a wide range of shear rates and
die angles, the model is seen to predict the entry
pressure fairly closely.

Although values of the entry pressure were obtained at a
die semi angle of 15˚ with the injection moulding
machine, conventional laboratory rheometers are unable to
accommodate dies with low entry angles. This is due to
the constraints imposed on the size and shape of the die
by the die holder and the position of the pressure
transducer. For this reason, the effect of very low die
on the rheological properties could not be investigated.
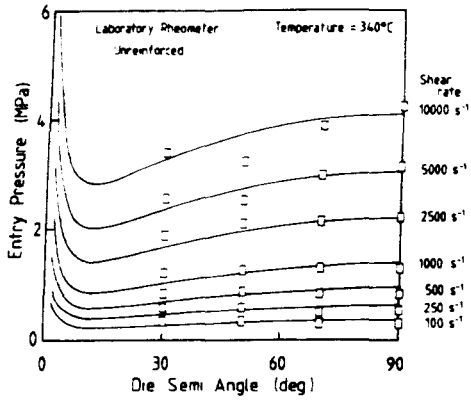
Figure 4.11. Entry pressure vs. die semi angle, for the unreinforced polymer, using the laboratory rheometer, comparing the predicted entry pressure with experimentally obtained values.

Figure 4.12. Entry pressure vs. die semi angle, for the glass reinforced polymer, using the laboratory rheometer, comparing the predicted entry pressure with experimentally obtained values.

Figure 4.13. Entry pressure vs. die semi angle, for the glass reinforced polymer, using the injection moulding machine comparing the predicted entry pressure with experimentally obtained values.

207
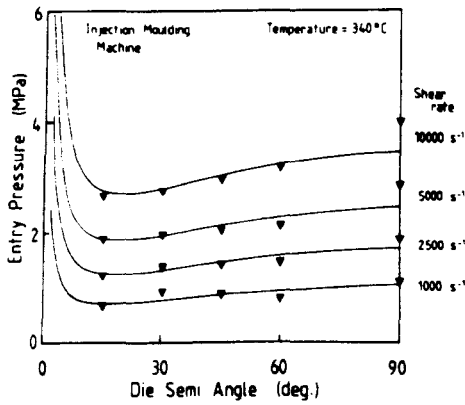
5.4   Mechanical Properties and Morphology

5.4.1   Layer Structure

The layer structure, consisting of four distinct layers,
symmetric about the core, is clearly visible in figures
4.21 and 4.22. At higher magnification each layer can be
seen to consist of a network of fine dark lines, when
viewed between crossed polarizers, referred to as a
schlieren texture[1]. These dark threads correspond to
extinction positions, where the director lies parallel or
normal to the polarizer planes. Where two or more lines
meet, a point singularity exists, referred to as a
disclination. Individual lines were difficult to examine
due to a lack of resolving power in the optical
microscope. The highest magnification available was 1000,
but using this combination of lenses it was impossible to
focus on the structure. Hence the maximum magnification
achievable with the optical microscope was 500.

Figures 4.27 and 4.28, showing micrographs for the glass
filled polymer, reveal the schlieren texture in more
detail. Near the surface of the moulding the dark threads
are seen to run perpendicular to the flow direction. In
this region, the high extensional stress experienced by
the molecules during fountain flow, orients them in the
flow direction. The appearance of the almost parallel

threads may indicate a periodic variation in the direction of the director with position along the polymer chain. At the centre of the moulding the lines appear to form almost circular patterns, reflecting the minimal degree of molecular orientation.

The layer structure observed optically also matches very closely with that revealed by etching the polymer, figures 4.39 and 4.40. Perpendicular to the flow direction two different structures are observed. The first structure corresponds to layers I and III, with the less oriented layers, II and IV, accounting for the second structure. This is in contrast to the structure observed parallel to the flow, where layers of similar orientation do not show similar topography.

The different deformation histories experienced by the polymer and the lack of correlation between sections etched parallel and perpendicular to the flow direction make the results of the etching difficult to interpret. Thapar and Bevis[68,89], observed a continuous change the structure of a HBA/HNA copolymer, which is not evident in this particular polymer. The discontinuous change from one layer to another seen in the sections perpendicular to the flow direction clearly indicates a distinct change in morphology.

At higher magnification, the structure appears to

indicate a system with two types of morphology. Figure
4.41 clearly shows the preferential etching of a
discontinuous phase, revealing a Swiss-cheese type
morphology, somewhat similar to that observed by Hedmark
et al.[87].

The etching process clearly reveals distinct
morphological features in the polymer. However,
conclusions about molecular structure are difficult to
reach. The observed morphology is seen to depend on the
macroscopic orientation of the section and on position
through the section thickness. It has also been shown
that different solutions will etch the polymer to varying
degrees[87], and reveal different structures. Hence it
can be seen that the interpretations of any etched
surface must be regarded with caution.

5.4.2 Section Thickness

The effect of section thickness on the tensile strength
of injection moulded specimens is shown by figure 4.14.
Although the reduction in the tensile strength, along the
flow direction, is not as large as that reported by
Boldizar[67] and by Thapar and Bevis[68], it still
constitutes a significant drop in the mechanical
properties. The fall in the tensile strength in the flow
direction is in contrast to an increase in strength with

section thickness for specimens tested perpendicular to the flow direction. These results suggest that, as the thickness of a moulding increases, there is an increasing proportion of the moulding which is not oriented in the major flow direction.

This is supported by the results of the morphology studies. Figures 4.23 and 4.24 show how the various layers alter as the section thickness increases. Blundell and coworker[82] have indicated that layers I and III are more oriented in the flow direction than layers II and IV. Figure 4.23 indicates that the thickness of the skin, layer I, increases only slightly with section thickness, while the third layer remains almost constant above a section thickness of 1.5mm. This is in contrast to a steady increase in the thickness of the second layer, up to a section thickness of about 2.5mm, and a significant growth in the thickness of the core, layer IV. Expressed as a percentage of the moulding, figure 4.24 clearly shows a reduction in the proportion of material which is highly oriented in the flow direction, at the expense of layers which are less oriented, and in the case of the core of the moulding, transversely oriented.

The level of molecular orientation present in the core of the moulding is shown by the results of the X-ray diffraction. An approximate, estimated value of -0.17 for the Hermans orientation function suggests a certain
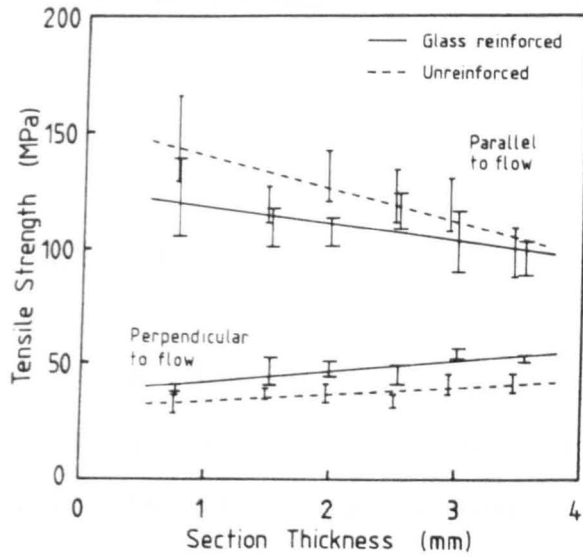
Figure 4.14. Tensile strength vs. section thickness for
the reinforced and unreinforced grades of polymer, tested
parallel and perpendicular to the major flow direction.
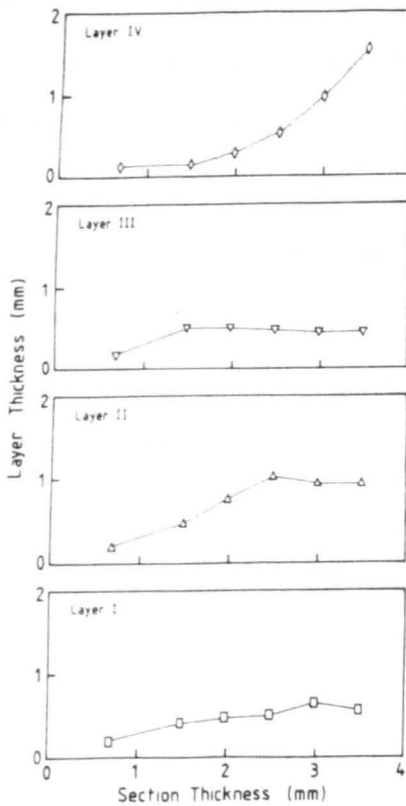
Figure 4.23. The thickness of the individual layers
plotted against the section thickness.
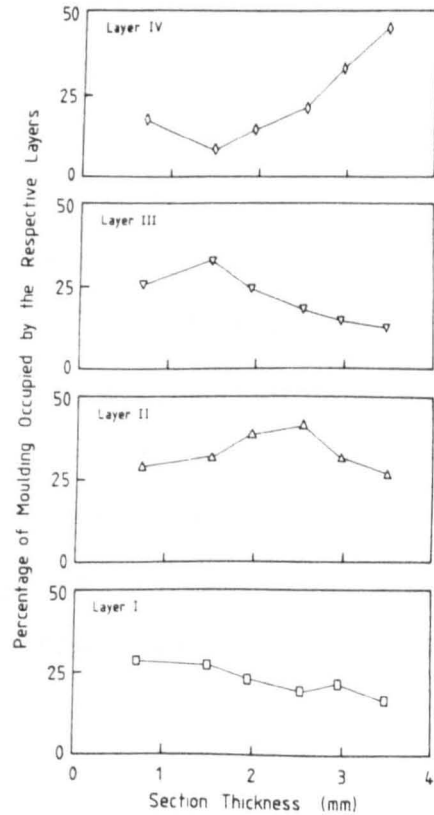
Figure 4.24. The thickness of the individual layers,
expressed as a percentage of the section thickness,
plotted against the section thickness.

212

degree of transverse orientation in the centre of the
moulding.

5.4.3 Weld Line Strength

It was mentioned in section 2.3.2.2 that gate and mould
degigns which result in multiple flow fronts are not
recommended for LCPs due to the formation of weld lines.
The deleterious effect of a weld line on the tensile
strength of a moulding is clearly illustrated by figure
4.15.

Immediately after the obstruction producing the weld
line, the tensile strength, perpendicular to the flow
direction, is reduced to less than 20% of the strength
upstream of the obstruction. The strength increases
rapidly, up to a distance of approximately 20mm
downstream of the obstruction, reaching about 40% of its
original value. This indicates a certain degree of mixing
and inter diffussion along the weld line as the two flow
fronts meet. After this sharp increase, the weld line
strength increases only gradually for the unreinforced
polymer, and remains constant for the glass reinforced
polymer.

In practical applications where weld lines are
unavoidable, the length of the weld line is usually kept

to a minimum, and is unlikely to exceed 20mm. Hence, it is clear that such a region of a moulding will be a week spot, with a strength between 20 - 40% of the normal value. It is therefore important that, where weld lines are present, the stresses perpendicular to the flow direction are kept to a minimum.

5.4.4   Dynamic Mechanical and Thermal Analysis

Plots of tan δ, the mechanical loss factor, against temperature indicate the occurrence of three distinct loss processes, figure 4.16. The high temperature, α, process was found to occur at approximately 140°C, which matches the transition seen on the DSC trace shown in figure 5.2. The α process is believed to be akin to a glass transition type process, and is associated with a significant drop in the storage modulus.

The lower temperature relaxation processes, referred to as ß and Γ, correspond to local mode processes occurring in the molecular chain. Troughton et al.[74] found that a transition taking place at approximately 50°C was associated with the motion of HNA residues, and it is possible that the weak ß process, seen at 62°C, is related to the motion of the small percentage of HNA which is present in SRP1. The larger Γ process is most probably associated with the motion of phenyl groups in
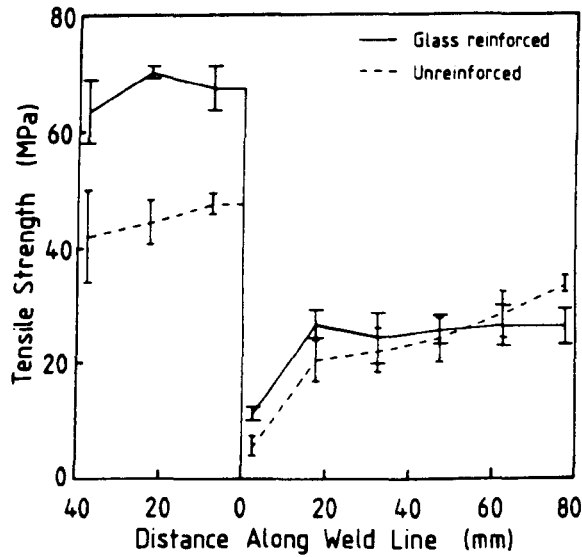
Figure 4.15. Tensile strength vs. distance along the weld line, indicating the weld line strength of the reinforced and unreinforced polymer.

Figure 4.16. Plot of log storage modulus and tan δ against temperature, obtained by DMTA. Results for a 0.7mm thick section, parallel to the flow direction for the reinforced and unreinforced polymer.

215
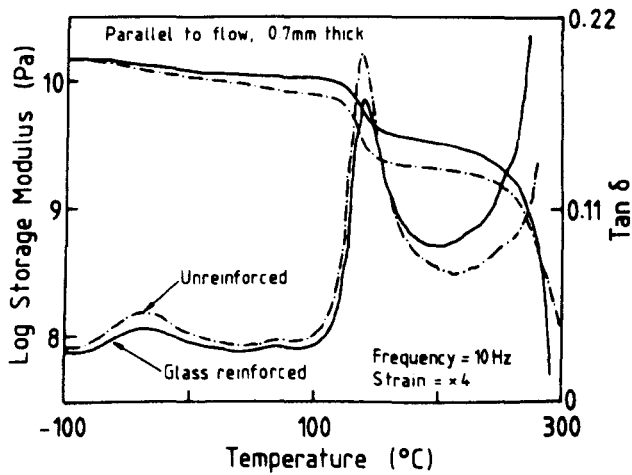
the main chain. Although Troughton et al. indicate a temperature in the region of -60°C for this type of relaxation process, the higher test frequency of 10Hz, and the inclusion of meta linkages in the polymer chain may account for the higher temperature, -30°C, observed in this study. Frosini and Levita[119] have indicated a loss process in the region of 0°C, for a number of aromatic polyesters, which is associated with the movement of phenyl groups in the chain. This temperature may be higher than is seen in SRP1 due to the faster frequencies employed in the experimental studies. Wissbrun and Yoon[72] have shown that an increase in test frequency from approximately 2.5 to 200Hz can result in an increase in the temperature, of a Γ transition, by about 30°C.

The very small drop in the modulus around the Γ relaxation supports the view that it associated with movement of the phenyl groups. For the para linked phenyl groups, rotation about the 1-4 axis of the unit requires no co-operative chain motion, and essentially leaves the polymer chain unaltered. The overall chain orientation remains unchanged with very little effect on storage modulus. Although the rotation of the meta linked phenyl groups requires a certain degree of co-operative movement, these groups are predominantly contained within the less oriented regions of the polymer chain, and so any co-operative motion will not greatly affect the

overall chain modulus.

5.4.5 Glass Reinforcement

One of the most noticeable effects of the addition of glass fibres to the polymer is the overall reduction in the mechanical anisotropy. Figure 4.14 indicates that the inclusion of glass fibres reduces the tensile strength in the flow direction while increasing the strength perpendicular to the flow direction.

Due to the anisotropic nature of LCPs, when discussing the mechanical properties it is customary to refer to the properties in the flow direction, rather than those in the transverse direction. For this reason the expression glass 'reinforcement' is technically not applicable since the glass fibres do not actually produce a reinforcing effect parallel to the flow direction.

The results from the examination of the fracture surfaces of the glass filled polymer reveal a possible explanation for the reduction in the tensile strength. Figures 4.35 to 4.38 show a large degree of fibre pull out, with very clean fibres. This is indicative of a poor bond between the fibre and the matrix, resulting in a less than effective use of the fibres as a reinforcing element. The micrographs of the fracture surfaces indicate that the

glass fibres also disrupt the formation of the hierarchical structure, which may reduce the degree of molecular orientation. In addition to this it has been shown that the inclusion of glass fibres reduces the extensional viscosity of the polymer at high strain rates. It is believed that the reduction in the extensional viscosity is caused by the glass fibres replacing highly extended, and hence highly oriented, polymer units. The reduction in the amount of these highly oriented polymer units will lead to a drop in the mechanical properties in the flow direction.

5.4.6 X-Ray Diffraction

The results of the X-ray diffraction show two main features. These are a broad equatorial spot, and faint aperiodic arcs on the meridional axis. The equatorial spot is associated with inter chain distance and also the angular spread in molecular alignment, shown in figure 4.44. The meridional lines are related to the length of the comonomers[120].

Using the Bragg equation, the equatorial reflection implies an inter chain distance of approximately 4.3Å, while the meridional arcs indicate a comonomer length of about 5.7Å, which is similar to the length of the HBA repeat unit.
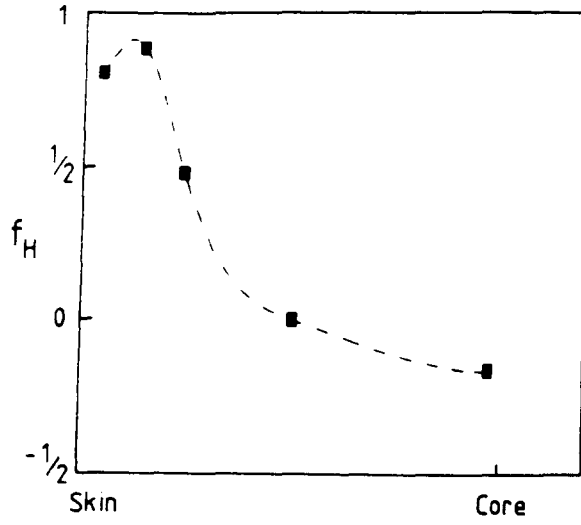
Figure 4.44. Hermans orientation function plotted against
position through the thickness of the moulding.

From the rheological studies, the aspect ratio of the
flowing unit in the polymer was estimated to be in the
region of 12 at high strain rates. If we assume that the
polymer chain is a solid rod of diameter 4.3Å, the inter
molecular distance, then an aspect ratio of 12 would
imply a chain which consisted of only 9 monomer units.
Such a small number is an unrealistic value and in turn
implies a flowing unit which is not a single chain, but
an aggregate of a number of chains. The flowing unit may
then be envisaged as a domain, in which the molecular
chains lie virtually parallel to each other, and flow as
a single entity.

CHAPTER 6

Conclusions

6.1   Rheology

1. SRP1 exhibits a shear and extensional viscosity which is almost independent of temperature between 330°C and 350°C.

2. The shear and extensional flow may be approximately described by power law relationships over the range of shear rates covered.

3. Empirical data may also be fitted by a Carreau-Ysasuda type equation from which the power law constants and a zero-rate Newtonian viscosity may be obtained.

4. SRP1 has an extensional viscosity which is more sensitive to strain rate than many other conventional thermoplastics.

5. The addition of glass fibres increases the shear viscosity over the full range of shear rates examined.

6. The presence of glass fibres reduces the extensional viscosity at high strain rates.

7. The Batchelor equation predicts a flowing unit in the glass filled polymer which corresponds to a single glass fibre surrounded by a cylindrical film of polymer, or an aggregation of fibres flowing as a unit, which are representative of the volume fraction.

8. Applying the Batchelor equation to the unfilled polymer predicts aspect ratios which increase with strain rate, and implies a flowing unit, or domain, comprised of a number of aligned molecules.

9. The results from the laboratory rheometer and the injection moulding machine are in reasonable agreement, despite the differences in thermal and shear history.

10. Within experimental error, the rheological model was found to predict experimental entry pressures, over the range of die angles and shear rates studied.

6.2   Mechanical Properties and Morphology

1. The tensile strength, in the flow direction, decreases with increasing section thickness. This corresponds to a reduction in the percentage of the moulding which is occupied by the more oriented layers.

2. The presence of a weld line has a detrimental effect on the mechanical properties, reducing the tensile strength to less than 50% of its upstream value.

3. Dynamic mechanical and thermal analysis indicated three loss processes. These corresponded to a type of glass transition and local mode possesses occurring in the molecular chain.

4. The addition of glass fibres causes a reduction in the tensile strength, when specimens are tested in the flow direction. This is caused by a poor fibre-matrix bond, and a disruption to the highly aligned polymer domains.

5. The layer structure when viewed by optical microscopy, is characterised by a schlieren texture.

6. X-ray diffraction revealed changes in orientation through the thickness of a moulding, indicating highly oriented skin layers and some transverse orientation in the core.

CHAPTER 7

Suggestions for Further Work

7.1   Rheology

As mentioned in section 5.3.5, conventional laboratory rheometers are unable to accommodate dies with low entry angles. It would therefore be both interesting and advantageous to design a laboratory rheometer which would allow the use of long, low angle dies. This would require a die holder which could be independently heated, to maintain the correct temperature in the die. This would then allow a complete analysis of the rheological model, covering the full range of die angles.

In designing a new laboratory rheometer, it would also be relevant to practical polymer processing if the polymer could be pre sheared prior to charging the rheometer. This would eliminate some of the problems associated with looking at the rheological properties of glass reinforced polymers, where fibre degradation is often an important factor. This particular problem may be overcome by the use a much smaller instrumented injection moulding machine. A bench top machine is currently under investigation by ICI for this purpose.

7.2   Mechanical Properties and Morphology

The results from the morphological examinations have been
seen to be difficult to interpret, and hence more work in
this area is necessary. An examination of the rheometer
extrudate may have proved interesting, allowing visible
structures to be related to a known shear rate. The use
of alternative methods of producing thin sections and the
use of more than one etchant may provide more
information. A hot stage microscope may also be useful in
gaining an insight into structures which form during
solidification.

A more detailed examination of the orientation would have
been interesting. It would also be informative to compare
the orientation parameters obtained by using both X-ray
diffraction and the aggregate model, as described by
Troughton et al.[73,74].

References

1. D. Demus and L. Richter; Textures of Liquid Crystals. Verlag Chemie Weinheim, New York, 1978.

2. G.W. Calundan and M. Jaffe, Anisotropic polymers, Their Synthesis and Properties, in Proceedings of the Robert A. Welch Foundation Conferences on Chemical Research, Research Conference XXVI, Synthetic Polymers, 1982.

3. A.E. Zachariades and R.S. Porter(Eds); High Modulus Polymers, Approaches to design and development, Marcel Dekker, 1988, Capter 1.

4. P.J. Flory; Proc. R. Soc., Ser. A 234, 1956, 73-89.

5. R.W. Lenz and J. Jin; Polym. News, 11, 1986, 200-204.

6. F.N. Cogswell; Plast. and Rubber Int., 12, 1987, 36-39.

7. F.C. Frank; Proc. Roy. Soc., Ser. A 319, 1970, 127-136.

8. K. Wissbrun; J. Rheol., 25, 1981, 619-662.

9. A.E. Zachariades and R.S. Porter(Eds); High Modulus Polymers, Approaches to design and development, Marcel Dekker, 1988, Capter 3.

10. W. Jackson; Br. Polym. J., 12, 1980, 154-162.

11. Z. Tadmor; J. of Appl. Polym. Sci., 18, 1974, 1753-1772

12. T. Weng, A. Hiltner and E. Baer; J. Mater. Sci., 21, 1986, 744-750.

13. E. Suokas; Polymer, 30, 1989, 1105-1112.

14. A.I. Isayev and J. Modic; Celanese, Antec Conference, 1986.

15. M. Nobile, E. Amendola and L. Nicolais; Polym. Eng. and Sci., 29, 1989, 244-257.

16. D.G. Baird and G.L. Wilkes; Polym. Eng. and Sci., 23, 1983, 632-636.

17. A Breakthrough in High-Performance Thermoplastics, Matchless Features, Countless Applications You never Thought Possible; Celanese Publications.

18. R.N. Butler; Celanese, Projection's Conference, Sept. 1986.

19. Tai-Shung Chung; Polym. Eng. and Sci., 26, 1986, 901-919.

20. J. Wendorff and J. Zimmerman; Die Angewandte Makromolekulare Chemie, 145/146, 1986, 231-257.

21. S. Chandrasekhar; Liquid Crystals, Cambridge University Press, 1980.

22. P. Meurisse, C. Noel, L. Monnerie and B. Fayolle; Br. Polym. J., 13, 1981, 55-63.

23. R.W. Lenz; Pure and Appl. Chem., 57, 1985, 977-984.

24. H, Toriumu, H. Furuya and A. Abe; Polymer Journal, 17, 1985, 895-898.

25. J. Clements and J. Humphrys; J. Polym. Sci. Part B, 24, 1986, 2293-2305.

26. A. Ciferri, W.R. Krigbaum and R.B. Meyer(Eds); Polymer Liquid Crystals, Academic Press, 1982, Chapter 10.

27. A. Ciferri, W.R. Krigbaum and R.B. Meyer(Eds); Polymer Liquid Crystals, Academic Press, 1982, Chapter 7.

28. L. Chapoy(Ed); Recent Advances in Liquid Crystalline Polymers, Elsevier Applied Science Publishers, 1985, Chapter 1.

29. B. Griffin and M. Cox; Br. Polym. J., 12, 1980, 147-153.

30. J. McIntyre and A. Milburn; Br. Polym. J., 13, 1981, 5-10.

31. M. Kyotani, K. Yoshida, K. Ogawara and H. Kanetsuna; J. Appl. Polym. Sci., Part B, 25, 1987, 501-511.

32. J. Jin, S. Antoun, C. Ober and R. Lenz; Br. Polym. J., 12, 1980, 132-146.

33. A. Ciferri, W.R. Krigbaum and R.B. Meyer(Eds); Polymer Liquid Crystals, Academic Press, 1982, Chapter 4.

34. H. Ringsdorf and A. Schneller; Br. Polym. J., 13, 1981, 43-46.

35. G.S. Attard and G. Williams; Chem. Br., Oct. 1986, 919-924.

36. M. Engel, B. Hisgen, R. Keller, W. Kreuder, B. Reck, H. Ringsdorf, H. Schmidt and P. Tschirner; Pure and Appl. Chem., 57, 1985, 1009-1014.

37. S. Berg, V. Krone, H. Ringsdorf; Makromol. Chem., Rapid Commun., 7, 1986, 381-388.

38. A. Abe; Macromolecules, 17, 1984, 2280-2287.

39. G. Chen and R.W. Lenz; J. Polym. Sci., Polym. Chem, 22, 1984, 3189-3201.

40. R.W. Lenz; Faraday Discuss. Chem. Soc., 79, 1985, 21-32.

41. A. Furukawa and R.W. Lenz; Macromol. Chem., Macromol. Symp. 2, 1986, 3-20.

42. H. Furuya, K. Asahi and A. Abe, Polymer Journal, 18, 1986, 779-782.

43. S. Hu and M. Xu; J. Polym. Sci. Part B, 27, 1989, 1749-1765.

44. G. Kiss; J. Rheol., 30, 1986, 585-599.

45. A. Ciferri, W.R. Krigbaum and R.B. Meyer(Eds); Polymer Liquid Crystals, Academic Press, 1982, Chapter 2.

46. W. Krigbaum, C. Liu and D. Yang; J. Polym. Sci. Part B, 26, 1988, 1711-1725.

47. K. Itoyama; J. Polym. Sci. Part B, 26, 1988, 1845-1836.

48. D. Yang and W. Krigbaum; J. Polym. Sci. Part B, 27, 1989, 1837-1851.

49. L. Chapoy(Ed); Recent Advances in Liquid Crystalline Polymers, Elsevier Applied Science Publishers, 1985, Chapter 10.

50. G. Astarita, G. Marrucci and L. Nicolais(Eds); Rheology, Volume 1, lecture 4.1, Plenum Press, 1980.

51. D.G. Baird; Polymeric Liquid Crystals, Proceedings of the 2nd Symposium at the American Chemical Society, Aug. 1983.

52. A. Gotsis and D.G. Baird; J. Rheol., 29, 1985, 539-556.

53. D. Yang and W. Krigbaum; J. Polym. Sci. Part B, 27, 1989, 819-835.

228

54. G. Viola and D.G. Baird; J. Rheol., 30, 1986, 601-628.

55. K.F. Wissbrun; Br. Polym. J., 12, 1980, 163-169.

56. C. Gochanour and M. Weinberg; J. Rheol., 30, 1986, 101-124

57. C. Gochanour and M. Weinberg; Unknown source.

58. F.N. Cogswell; Br. Polym. J., 12, 1980, 170-173.

59. R.T. Fenner; Principles In Polymer Processing, The MacMillan Press Ltd, 1979.

60. J.A. Brydson; Flow Properties of Polymer Melts, George Godwin, in assoc. with Plastics and Rubber Institute, 1981.

61. R. Jerman and D.G. Baird; J. Rheol., 25, 1981, 275-292.

62. Engineering Thermoplastic Materials Selector, Celanese Publications.

63. Victrex SRP, Self Reinforcing Polymers, Properties and Processing, ICI Advanced Materials.

64. Vectra Liquid Crystal Polymers; Guidelines and Specifications, Moulding High-performance Resins, Celanese Publications.

65. Vectra Liquid Crystal Polymers; Celanese Publications.

66. Z. Ophir and Y. Ide; Polym. Eng. and Sci., 23, 1983, 792-796.

67. A. Boldizar; Plast. and Rubber Process. and Appl., 10, 1988, 73-78.

68. H. Thapar and M. Bevis; Plast. and Rubber Process. and Appl., 12, 1989, 39-52.

69. G.E. Williams and S.K. Garg; U.S. Polymer Symposium, Oct. 1985.

70. M.J. Folkes; Short Fibre Reinforced Thermoplastics, Research Studies Press, 1982.

71. T. Murayama; Dynamic Mechanical Analysis of Polymeric Material, Elsevier, 1978.

72. K. Wissbrun and H. Yoon; Polymer, 30, 1989, 2193-2197.

73. A.E. Zachariades and R.S. Porter(Eds); High Modulus Polymers, Approaches to design and development, Marcel Dekker, 1988, Capter 2.

74. M. Troughton, G. Davies and I. Ward; Polymer, 30, 1989, 58-62.

75. H. Voss and K. Friedrich; J. Mater. Sci., 21, 1986, 2889-2900.

76. J.S. Wu, K. Friedrich and M. Grosso; Composites, 20, 1989, 223-233.

77. Y. Ide and T. Chung; J. Macromol. Sci. - Phys., B23(4-6), 1984-5, 497-509.

78. G. Viola, D. Baird and G. Wilkes; Polym. Eng. and Sci., 25, 1985, 888-895.

79. J. Jenkins and G. Jenkins; J. Mater. Sci., 22, 1987, 3784-3792.

80. J. White; Polym. Eng. and Sci.; 15, 1975, 44-50.

81. M. Kamal and S. Kenig; Polym. Eng. and Sci.; 12, 1972, 302-308.

82. D. Blundell, R. Chivers, A. Curson, J. Love and W. MacDonald; Polymer, 29, 1988, 1459-1467.

83. L. Sawyer and M. Jaffe; J. Mater. Sci., 21, 1986, 1897-1913.

84. D. Hull; An Introduction to Composite Materials, Cambridge University Press, 1981.

85. D.W. Clegg and A.A. Collyer(Eds); Mechanical Properties of Reinforced Thermoplastics, Elsevier Applied Science Publishers, 1986, Chapter 7.

86. E. Joseph, G. Wilkes and D. Baird; Polym. Eng. and Sci.; 25, 1985, 377-388.

87. P. Hedmark, J. Jansson, A. Hult, H. Lindberg and U. Gedde; J. Appl. Polym. Sci., 34, 1987, 743-762.

88. S. Chen, Y. Jin, S. Hu and M. Xu; Polymer Communications, 28, 1987, 208-211.

89. H. Thapar and M. Bevis; J. Mater. Sci. Letters 2, 1983, 733-736.

90. M. Dobb. D. Johnson and B. Saville; J. Polym. Sci., Part B, 15, 1977, 2201-2211.

91. A. Donald, C. Viney and A. Windle; Polymer, 24, 1983, 155-159.

92. C. Viney, A. Donald and A. Windle; J. Mater. Sci., 18, 1983, 1136-1142.

93. A. Donald and A. Windle; J. Mater. Sci., 18, 1983, 1143-1150.

94. C. Viney, A. Donald and A. Windle; Polymer, 26, 1985, 870-878.

95. M. Kwiatkowski and G. Hinrichsen; J. Mater. Sci., 25, 1990, 1548-1550.

96. A. Donald and A. Windle; Polymer, 25, 1984, 1235-1246.

97. D. Blundell; Polymer, 23, 1982, 359-364.

98. G. Butzbach, J. Wendorff and H. Zimmermann; Polymer, 27, 1986, 1337-1344.

99. R. Spontak and A. Windle; J. Mater. Sci., 25, 1990, 2727-2736.

100. F.N. Cogswell; Polymer Melt Rheology, George Godwin Ltd, in assoc. with Plastics and Rubber Institute, London, 1981.

101. A.A. Collyer and D.W. Clegg(Eds); Rheological Measurements, Elsevier Applied Science, 1988, Chapter 1.

102. C.D. Han; Rheology in Polymer Processing, Acadamic Press, 1976.

103. A. McClelland and A.G. Gibson; Composites Manufacturing, 1, 1990, 15-25.

104. E.B. Bagley; J. Appl. Phys., 28, 1957, 624-627.

105. F.N. Cogswell; Polym. Eng. and Sci., 12, 1972, 64-73.

106. D.M. Binding; J. Non-Newt. Fluid Mech., 27, 1988, 173-189.

107. D.M. Binding and K. Walters; J. Non-Newt. Fluid Mech., 30, 1988, 233-250.

108. A.G. Gibson; Composites, 20, 1989, 57-64.

109. A.A. Collyer and D.W. Clegg(Eds); Rheological Measurements, Elsevier Applied Science, 1988, Chapter 3.

110. A. McClelland; PhD Thesis, University of Liverpool, 1989.

111. S.P. Corscadden; PhD Thesis, University of Liverpool, 1989.

112. G.K. Batchelor; J. Fluid. Mech., 46, 1971, 813-829.

113. J.A. Brydson; Plastic Materials, Iliffe Books Ltd. 1966.

114. D.B. Parker; Polymer Chemistry, Applied Science Publishers Ltd. 1974.

115. L.E. Alexander; X-Ray Diffraction Methods in Polymer Science, John Wiley and Sons, Inc. 1969.

116. D.J. Groves; Personal communication, ICI Wilton.

117. H.J. Pitz; Flow and Cure of Polymers - Measurement and Control, Rapra Technology Limited, March 1990.

118. A.G. Gibson; Personal communication.

119. V. Frosini, G. Levita, J Landis and A.E. Woodward; J. Polym. Sci., Polym. Phys. Ed., 15, 1977, 239-245.

120. D. Judas, Y. Germain, C. Biver, S. Girault and C. Taupin; Nature Supplement, 350, 1991, 28-29.

121. A. Kelly; Strong Solids, Clarendon Press, Oxford, 1973, Chapter 5.

APPENDIX 1

Derivation of Batchelor Equation

The approach used will be analogous to that adopted by Cox[121] in the well known description of the elastic modulus of short fibre reinforced solids. Each fibre element in a cell model will be considered to be surrounded by a cylinder of fluid, shown in figure 8.1a. The outer surface of that cylinder is assumed to be subject to a velocity and strain rate regime representative of the average motion of the surrounding material.

Consider a suspension of aligned fibres subject to an extensional flow regime where the extension rate is ϵ.

The mid point of the fibre will be considered to be the point z=0. If the elongational strain rate along the boundary $r=r_1$ is constant and the relative velocity, v_1, between the fluid and the fibre is zero at z=0, then since:

$$\epsilon = \frac{dv_1}{dz} = \frac{v_1}{z}$$

$$v_1 = \epsilon z \qquad\qquad 8.1$$

Consider a section, thickness dz, shown in figure 8.1b. The shear stress, τ, induced by the viscous resistance of

233

the fluid will vary with r such that:

$$\tau_1 r_1 = \tau_0 r_0 = \tau r$$

so

$$\tau = \frac{\tau_1 r_1}{r} = \frac{\tau_0 r_0}{r} \qquad\qquad 8.2$$

Consider first the case of a Newtonian fluid. The shear rate will be given by:

$$\Gamma = \frac{\tau}{\eta} = \left[\frac{\tau_0 r_0}{\eta}\right] \cdot \frac{1}{r} \qquad\qquad 8.3$$

therefore,

$$v = \left[\frac{\tau_0 r_0}{\eta}\right] \cdot \int_{r_0}^{r} 1/r \ \ dr$$

$$= \left[\frac{\tau_0 r_0}{\eta}\right] \cdot \ln\left[\frac{r}{r_0}\right] \qquad\qquad 8.4$$

therefore,

$$v_1 = \left[\frac{\tau_0 r_0}{\eta}\right] \cdot \ln\left[\frac{r_1}{r_0}\right] \qquad\qquad 8.5$$

$$\tau_0 = \frac{\eta \cdot \varepsilon \cdot z}{r_0 \cdot \ln(r_1/r_0)} \qquad\qquad 8.6$$

From a force balance on a short element of fibre, shown in figure 8.1c,

$$d\sigma_f \cdot \pi r_0^2 = -\tau_0 \cdot 2\pi r_0 \cdot dz \qquad\qquad 8.7$$

$$d\sigma_f = \frac{-2\tau_0}{r_0} \ dz$$

$$d\sigma_f = \frac{-2\Pi \cdot \epsilon \cdot z}{r_o^2 \cdot \ln(r_1/r_o)} \, dz \qquad 8.8$$

$$\sigma_f = \frac{-2\Pi \cdot \epsilon}{r_o^2 \cdot \ln(r_1/r_o)} \cdot \int_{L/2}^{z} z \; dz$$

$$= \frac{-2\Pi \cdot \epsilon}{r_o^2 \cdot \ln(r_1/r_o)} \cdot \tfrac{1}{2} \cdot \left[z^2 - (L/2)^2 \right] \qquad 8.9$$

The average value of σ_f in the fibre may be found from

$$\sigma_{fav} = \frac{2}{L} \cdot \int_{0}^{L/2} \sigma_f \; dz$$

$$\sigma_{fav} = \frac{-2\Pi \cdot \epsilon}{r_o^2 \cdot \ln(r_1/r_o)} \cdot \frac{1}{L} \cdot \left[\frac{1}{3} \cdot z^3 - (L/2)^2 z \right]_{o}^{L/2}$$

$$= \frac{2\Pi \cdot \epsilon}{r_o^2 \cdot \ln(r_1/r_o)} \cdot \left[\frac{L^2}{12} \right]$$

$$\sigma_{fav} = \frac{2\Pi \cdot \epsilon}{3 \cdot r_o^2 \cdot \ln(r_1/r_o)} \cdot \left[\frac{L}{2} \right]^2 \qquad 8.10$$

Assume a population of fibres. The length of one particular fibre is L_i. The contribution of L_i to the extending stress will be $\sigma_{favi}V_i$.

Therefore, the total extending stress:

$$\sigma_e = \Sigma \; \sigma_{favi}V_i + \sigma_{em}V_m \qquad 8.11$$

$$\Pi_e = 1/\epsilon \cdot \Sigma \; \sigma_{favi}V_i + \Pi_{em}V_m \qquad 8.12$$

$$= \frac{2\cap}{3 \cdot \ln(r_1/r_0)} \cdot \Sigma \frac{L_i^2}{D^2} \ V_i \ + \cap_{em}V_m \qquad 8.13$$

The quantity r_1/r_0 may be related to V_f by making certain
assumptions about the spatial arrangements of fibres and
the effective radius, r_1, of the tube of fluid
surrounding each fibre.

For instance, a square array of fibres may be assumed,
figure 8.1d, and r_1 equated to the inter fibre spacing.

In this case

$$V_f \ = \ \frac{\pi r_0^2}{r_1^2}$$

$$\frac{r_0^2}{r_1^2} \ = \ \left[\frac{\pi}{V_f} \right]^{\frac{1}{2}} \qquad 8.14$$

In general it may be said that $\dfrac{r_0^2}{r_1^2} = \left[\dfrac{C}{V_f} \right]^{\frac{1}{2}}$ where C can
take a range of possible values depending on the
assumptions made. Changing these assumptions does not
change the value of C very much and $C = \pi$ leads to a
model which is identical with Batchelors[112].

$$\cap_e \ = \ \frac{4\cap}{3 \cdot \ln(\pi/V_f)} \cdot \Sigma \frac{L_i^2}{D^2} \ V_i \ + \cap_{em}V_m \qquad 8.15$$

An effective fibre length, L^*, can be defined such that

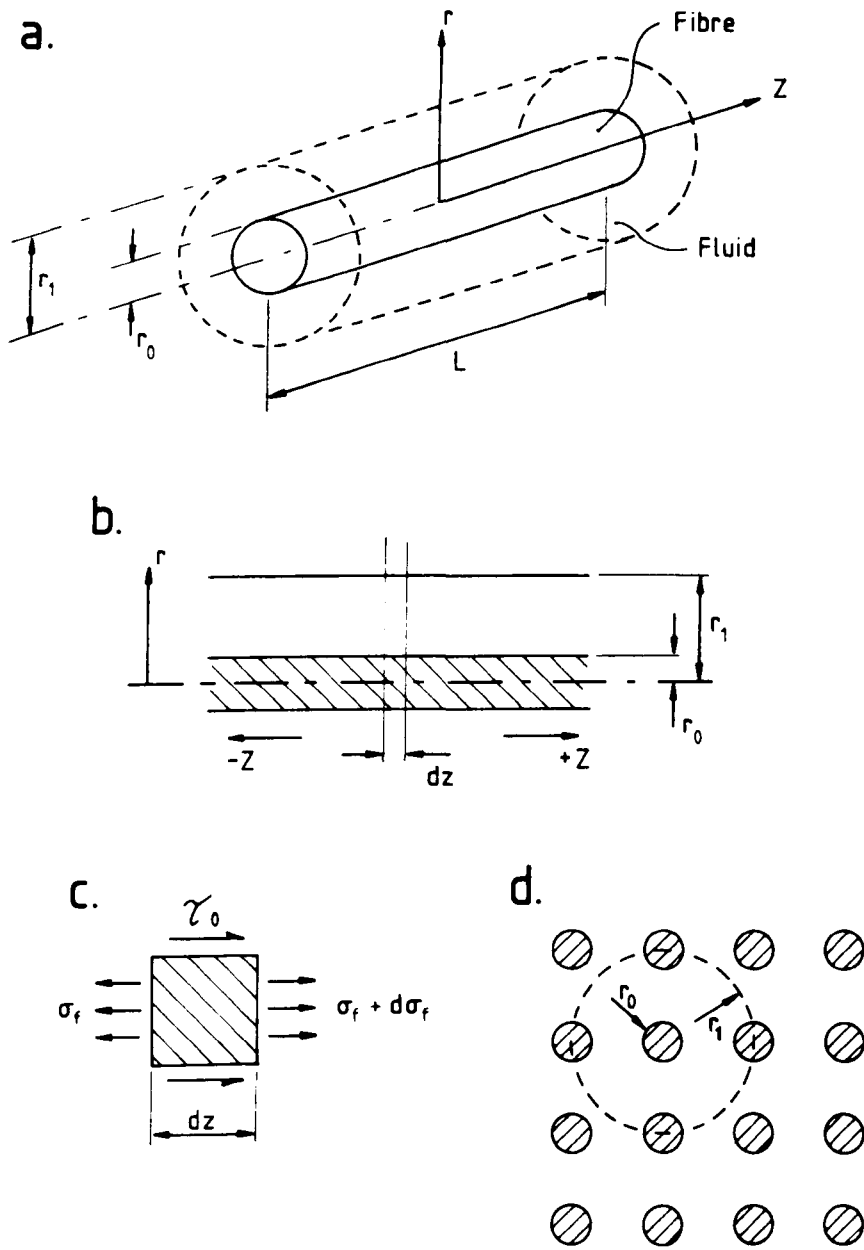$$L^{*2} \ = \ (1/V_f) \cdot \Sigma \ L_i^2 V_i$$

236

Figure 8.1.   Elements of Batchelor equation.
a. Fibre element surrounded by cylinder of fluid.
b. Cross section of fibre and fluid.
c. Force balance on section of fibre, length dz.
d. Square array of fibres.

237

$$V_i = V_f \cdot L_i / \Sigma \, L_i$$

$$L^{*2} = \frac{\Sigma \, L_i^3}{\Sigma \, L_i} \qquad\qquad 8.16$$

Then

$$\Omega_e = \frac{4 \Omega \cdot V_f}{3 \cdot \ln(\pi/V_f)} \cdot \left[\frac{L^*}{D}\right]^2 + \Omega_{em} V_m \qquad\qquad 8.17$$

For a dilute suspension of fibres in a Newtonian fluid, where $V_m \approx 1$, and $\Omega_{em} = 3 \cdot \Omega$, equation 8.17 corresponds to Batchelor's equation, equation 2.15, page 87.

APPENDIX 2

Power Law Version of Batchelor Equation

For a power law fluid an equivalent model for the extensional viscosity can be derived by an analogous procedure.

Assuming a power law relationship where:

$$\tau = G \cdot \Gamma^m \qquad\qquad 8.18$$

equation 8.3 can be written as:

$$\Gamma = \left[\frac{\tau}{G}\right]^{1/m}$$

$$\Gamma = \left[\frac{\tau_o r_o}{Gr}\right]^{1/m} \qquad\qquad 8.19$$

therefore,

$$
v = \left[\frac{\tau_o r_o}{G}\right]^{1/m} \cdot \int_{r_o}^{r} r^{(-1/m)} \, dr
$$

therefore,

$$
v_1 = \left[\frac{\tau_o r_o}{G}\right]^{1/m} \cdot \left[\frac{m}{1-m}\right] \cdot \left[1 - \left[\frac{r_o}{r_1}\right]^{(1-m)/m}\right] \qquad 8.20
$$

therefore,

$$
\varepsilon z = \left[\frac{\tau_o r_o}{G}\right]^{1/m} \cdot \left[\frac{m}{1-m}\right] \cdot \left[1 - \left[\frac{r_o}{r_1}\right]^{(1-m)/m}\right] \qquad 8.21
$$

Hence,

$$
\tau_o = \frac{G \cdot \varepsilon^m \cdot z^m}{r_o} \cdot \left[\frac{1-m}{m}\right]^m \cdot \left[1 - \left[\frac{r_o}{r_1}\right]^{(1-m)/m}\right]^{-m} \qquad 8.22
$$

From the force balance

$$
d\sigma_f = \frac{-2G \cdot \varepsilon^m}{r_o} \cdot \left[\frac{1-m}{m}\right]^m \cdot \left[1 - \left[\frac{r_o}{r_1}\right]^{(1-m)/m}\right]^{-m} \cdot z^m \, dz
$$

therefore,

$$
\sigma_f = \frac{\dfrac{-2G \cdot \varepsilon^m}{r_o} \cdot \left[\dfrac{1-m}{m}\right]^m \cdot \left[\dfrac{1}{m+1}\right]}{\left[1 - \left[\dfrac{r_o}{r_1}\right]^{(1-m)/m}\right]^m} \cdot \left[z^{(m+1)} - (L/2)^{(m+1)}\right] \qquad 8.23
$$

$$
\sigma_{fav} = \frac{2}{L} \cdot \int_{0}^{L/2} \sigma_f \, dz
$$

239

$$\sigma_{fav} = \frac{\dfrac{4G \cdot \varepsilon^m}{L \cdot r_o^2} \cdot \left[\dfrac{1-m}{m}\right]^m \cdot \left[\dfrac{1}{m+1}\right]}{\left[\,1 - \left[\dfrac{r_o}{r_1}\right]^{(1-m)/m}\,\right]^m} \cdot \left[\dfrac{m+1}{m+2}\right] \cdot \left[\dfrac{L}{2}\right]^{(m+2)}$$

$$\sigma_{fav} = \frac{\dfrac{2G \cdot \varepsilon^m}{r_o^2} \cdot \left[\dfrac{1-m}{m}\right]^m \cdot \left[\dfrac{1}{m+2}\right] \cdot \left[\dfrac{L}{2}\right]^{(m+1)}}{\left[\,1 - \left[\dfrac{r_o}{r_1}\right]^{(1-m)/m}\,\right]^m} \qquad 8.24$$

$$\eta_e = 1/\varepsilon \cdot \Sigma\ \sigma_{fav\,i} V_i \qquad 8.25$$

$$\eta_e = \frac{\dfrac{2G \cdot \varepsilon^{(m-1)}}{(m+2)} \cdot \left[\dfrac{1-m}{m}\right]^m \cdot \Sigma\ \dfrac{(L_i/2)^{(m+1)}}{r_o^2} \cdot V_i}{\left[\,1 - \left[\dfrac{r_o}{r_1}\right]^{(1-m)/m}\,\right]^m} \qquad 8.26$$

Substituting for r_o/r_1, and L^* gives

$$\eta_e = \frac{\dfrac{2G \cdot V_f \cdot \varepsilon^{(m-1)}}{(m+2)} \cdot \left[\dfrac{1-m}{m}\right]^m \cdot \left[\dfrac{L^*}{D}\right]^{(m+1)}}{\left[\,1 - \left[\dfrac{V_f}{\pi}\right]^{(1-m)/2m}\,\right]^m} \qquad 8.27$$

This corresponds to the power law version of Batchelors
equation, equation 5.4, section 5.3.4.4.